UNIVERSITY OF ALBERTA

AN APPROACH FOR PRECISE HARMONIC MEASUREMENTS

BY

DAVID JECTY NYARKO

A thesis submitted to the Faculty Of Graduate Studies and Research in partial fulfillment for the degree of DOCTOR OF PHILOSOPHY

DEPARTMENT OF ELECTRICAL ENGINEERING

EDMONTON, ALBERTA

FALL 1995

National Library
of Canada

Acquisitions and
Bibliographic Services Branch

395 Wellington Street
Ottawa, Ontario
K1A 0N4

Bibliothèque nationale
du Canada

Direction des acquisitions et
des services bibliographiques

395, rue Wellington
Ottawa (Ontario)
K1A 0N4

Your file Votre référence

Our file Notre référence

THE AUTHOR HAS GRANTED AN IRREVOCABLE NON-EXCLUSIVE LICENCE ALLOWING THE NATIONAL LIBRARY OF CANADA TO REPRODUCE, LOAN, DISTRIBUTE OR SELL COPIES OF HIS/HER THESIS BY ANY MEANS AND IN ANY FORM OR FORMAT, MAKING THIS THESIS AVAILABLE TO INTERESTED PERSONS.

L'AUTEUR A ACCORDE UNE LICENCE IRREVOCABLE ET NON EXCLUSIVE PERMETTANT A LA BIBLIOTHEQUE NATIONALE DU CANADA DE REPRODUIRE, PRETER, DISTRIBUER OU VENDRE DES COPIES DE SA THESE DE QUELQUE MANIERE ET SOUS QUELQUE FORME QUE CE SOIT POUR METTRE DES EXEMPLAIRES DE CETTE THESE A LA DISPOSITION DES PERSONNE INTERESSEES.

THE AUTHOR RETAINS OWNERSHIP OF THE COPYRIGHT IN HIS/HER THESIS. NEITHER THE THESIS NOR SUBSTANTIAL EXTRACTS FROM IT MAY BE PRINTED OR OTHERWISE REPRODUCED WITHOUT HIS/HER PERMISSION.

L'AUTEUR CONSERVE LA PROPRIETE DU DROIT D'AUTEUR QUI PROTEGE SA THESE. NI LA THESE NI DES EXTRAITS SUBSTANTIELS DE CELLE-CI NE DOIVENT ETRE IMPRIMES OU AUTREMENT REPRODUITS SANS SON AUTORISATION.

ISBN 0-612-06267-8

Canada

UNIVERSITY OF ALBERTA

LIBRARY RELEASE FORM

NAME OF AUTHOR:	DAVID JECTY NYARKO
TITLE OF THESIS:	AN APPROACH FOR PRECISE HARMONIC MEASUREMENTS
DEGREE:	DOCTOR OF PHILOSOPHY
YEAR THIS DEGREE GRANTED:	1995

Permission is hereby granted the University of Alberta Library to reproduce single copies of this thesis and to lend or sell such copies for private, scholarly or scientific research purposes only.

The author reserves all other publication and other rights in association with the copyright in the thesis, and except as hereinbefore provided neither the thesis nor any substantial portion thereof may be printed or otherwise reproduced in any material form whatever without the author's prior written permission.

.....
(Student's signature)

#202-9925-83Ave.,
EDMONTON,
ALBERTA
T6E 2B9

DATE: 5TH OCTOBER 1995

UNIVERSITY OF ALBERTA

FACULTY OF GRADUATE STUDIES AND RESEARCH

The undersigned certify that they have read, and recommend to the Faculty of Graduate Studies and Research for acceptance, a thesis entitled AN APPROACH FOR PRECISE HARMONIC MEASUREMENTS submitted by DAVID JECTY NYARKO in partial fulfillment of the requirements for the degree of DOCTOR OF PHILOSOPHY

Keith A. Stromsmoe

K.A. Stromsmoe

K.E. Bollinger

K.E. Bollinger

John C. Salmon

J. Salmon

R. E. Rink

R.E. Rink

K. Fyfe

K. Fyfe

Peter C. McLaren

P. McLaren

DATE: 5 Oct 1995

ABSTRACT

This thesis describes an approach to improve the accuracy of determining the amplitude and phase components of a periodic signal when discrete Fourier algorithms are used. In particular, this approach improves the accuracy in the determination of the harmonics of asynchronously sampled waveforms or a single period band-limited signal. Measurement accuracy is improved by reducing the primary spectral errors which are introduced by long, medium and short-range leakage effects. The algorithm used to determine the harmonic components, referred to as the trapezoidal compensating window (TCW) algorithm, uses a window referred to the TCW and a modified discrete Fourier transform algorithm. Long-term leakage effects are minimized since the TCW lobes vary in width with the fundamental signal period. The TCW having the advantage of the rectangular window by having it's first zero crossing close to the 1st harmonic, results in a reduction of medium-term leakage effects. Short-term leakage is reduced by the use of a discrete Fourier series type computation scheme which evaluates the harmonic components at the actual frequencies.

A hardware implementation of this approach is realized (with a software modification) on an existing 8Mhz 68000 microprocessor-based wattmeter design for voltage, current and electrical power signals in the DC to 1kHz range.

ACKNOWLEDGEMENT

I would like to thank my supervisor, Dr. Keith Stromsmoe, for his help and encouragement in preparing this thesis. Also the Alberta Microelectronic Centre for the design and construction of three prototype wattmeters based on the TCW algorithm. I would also like to thank Mr. Morris Locker for his help in obtaining the necessary tools for speeding up the design, construction and assembly of this thesis. Finally I express my thanks to my wife Margaret-Mary for her encouragement.

TABLE OF CONTENTS

ABSTRACT

ACKNOWLEDGEMENT

LIST OF TABLES

LIST OF FIGURES

LIST OF SYMBOLS AND ABBREVIATIONS

1. INTRODUCTION 1

    1.1 Comparison of analog and digital computational approaches 1

    1.2 Time-Domain sampling: The Sampling Theorem 2

    1.3 Effects of a finite data record length on measurement accuracy 5

    1.4 Summary of desirable window characteristics for leakage minimization 17

    1.5 Techniques for precise signal average value measurements 17

    1.6 Traditional harmonic measurements based on windows and the DFT 18

    1.7 Algorithm employed in thesis (TCW and modified DFT) 19

    1.8 Summary of windows properties for leakage error reduction 22

    1.9 Thesis organization 22

2. AVERAGE VALUE MEASUREMENT APPROACHES 24

    2.1 Fourier series representation of signals 24

    2.2 Spectrum Analysis for Discrete-Time signals 25

    2.3 DC value Computation and Windows 26

        2.3.1. Classical windows 28

            2.3.1.1 Rectangular Window 28

            2.3.1.2 Sum of Cosines Windows[14] 30

2.3.2. Compensating windows 34
2.3.2.1 Trapezoidal Compensating Window (TCW-Proposed Algorithm) 34
2.4 Summary of the Various Windowing Schemes 38
2.4.1 Window DTFT comparisons (N=60 and Δ=0.9 and k varying) 38
2.4.2 Window DTFT comparisons (N=60 and k=2, Δ varying) 41
2.5 Chapter Summary 45
3. HARMONIC MEASUREMENTS 46
3.1 Harmonic computation and windows 46
3.2 Basis Vectors in the Harmonic Computation Algorithm 49
3.3 Plots of the DFT of some Windows in Harmonic Computations 49
3.4 Experimental Results 52
3.4.1 A Waveform Exhibiting Long and Short-Term Leakage 52
3.4.2 Simulated Bandlimited PWM signal 55
3.5 Summary of results 63
4. THE FOURIER ANALYZER HARDWARE 65
4.1 CPUmain Module 66
4.2 Memory module 66
4.3 EPLD1 module 67
4.4 I/O Module 69
4.5 Timing-Controller Module 70
4.6 Analog-to-Digital Interface Module 72
4.7 Input Module 73
4.8 Power Supply Module 74

5. FOURIER ANALYZER SOFTWARE 75
5.1 Software Overview 75
5.2 The Main Program 77
5.2.1 The Main Menus 78
5.2.2 Module 0 79
5.2.3 Module 1 80
5.2.4 Module 2 81
5.2.5 Module 3 83
5.2.6 Module 4 86
5.2.7 Module 5 89
5.2.8 Module 6 89
5.2.9 Module 7 90
5.2.10 Module 8 91
5.2.11 Module 9 93
5.2.12 Module 10 93
5.2.13 Module 11 93
5.2.14 Module 12 94
5.2.15 Module 13 94
5.2.16 Module 14 94
5.2.17 Module 15 94
6. ERROR ANALYSIS 96
6.1 ADC quantization errors [19] 96
6.1..1 Amplitude Measurement 100
6.1.2 Phase Measurement 102
6.1.3 DC Component Measurement 102
6.2 Effect of Sample jitter [20] 103

6.3 Extension to signals derived from product of two sampled signals 105
6.4 Numerical Errors in the DFT Algorithm 106
6.5 Hardware errors 109
6.5.1 Voltage channel errors 109
6.5.2 Current channel errors 110
6.6 Error analysis for inaccuracies in Δ measurement 110
6.6.1 Amplitude Measurement errors 110
6.6.2 Phase Measurement error 112
6.7 Summary of results 113
7. FOURIER ANALYZER PERFORMANCE AND SPECIFICATIONS 114
7.1 Calibration 114
7.2 Performance Checks 114
7.3 Specifications 119
7.4 Algorithm performance on various platforms 120
8. CONCLUSIONS 122
8.1 The unique contributions of this thesis 123
8.2 Limitations of the TCW scheme as implemented in this thesis 123
8.3 Suggestions for further work 123
REFERENCES 124
APPENDIX SCHEMATIC DIAGRAMS 127

LIST OF TABLES

TABLE 1.1 Window characteristics required for Accurate harmonic measurements (Amplitude and Phase) 17

TABLE 1.2 Summary of how the TCW Algorithm reduces leakage errors. 22

TABLE 1.3 Summary of window properties for leakage error reduction 22

TABLE 2.1 Some commonly employed Sum of Cosines Windows 32

TABLE 2.2 The DC and first 7 harmonic DFT Magnitude values of some Windows for N=60 and =0.9 39

TABLE 2.3 The DC and first 7 harmonic DFT Phase values in degrees of some Windows for N=60 and =0.9 39

TABLE 2.4 The DTFT Magnitude values of some Windows for N=60 and k=2 42

TABLE 2.5 The DTFT Phase values in degrees of some Windows for N=60 and =2 ... 42

TABLE 3.1 The Amplitude values for Equation 3.5.1 53

TABLE 3.2 Percentage errors in Magnitude determination 54

TABLE 3.3 Percentage errors in Phase determination 54

TABLE 3.4 Switching Angles of Simulated PWM Signal 57

TABLE 3.5 The Harmonic Components of the PWM Waveform based on Switching Angles and Parameters indicated 58

TABLE 3.6 Percentage errors in Low Pass Filtered PWM Signal Magnitude determination (3 Periods) 60

TABLE 3.7 Percentage errors in Low Pass Filtered PWM Signal Phase determination (3 Periods) 61

TABLE 3.8 Percentage errors in Low Pass Filtered PWM Signal Magnitude determination (1 Period) 62

TABLE 3.9 Percentage errors in Low Pass Filtered PWM Signal Phase determination (1 Period) 63
TABLE 5.1 Software and Hardware interaction in sampling routine 77
TABLE 5.2 Parameters of 'C' function eval2() 86
TABLE 5.3 Value of y_i used in the various modes. 87
TABLE 7.1 RMS readings of Fourier analyzer and a 4-1/2 digit test digital meter 115
TABLE 7.2 Fourier analyzer readings for a 20V p-p 59.95Hz square wave 117
TABLE 7.3 Fourier analyzer readings for a 20V p-p 60.01Hz triangular wave 119
TABLE 7.4 Harmonic Computation Benchmarks for various platforms 121

LIST OF FIGURES

Figure 1.1 An example of the Fourier transform of an analog bandlimited signal. 3

Figure 1.2 The discrete time Fourier transform of the sampled analog bandlimited signal with the Fourier transform in Figure 1.1. 4

Figure 1.3. The application of a brickwall filter $H_c(\omega)$ for an analog signal reconstruction 4

Figure 1.4. Illustration of aliasing 5

Figure 1.5 Synchronous sampling scheme (1 period = 8 sample intervals) 6

Figure 1.6. Asynchronous sampling scheme (1 period = 8.5 sample intervals). The end-correction (Δ) is thus 0.5 7

Figure 1.7 Plot of some windows 8

Figure 1.8 The DTFT of a rectangular window for N=10 and Δ= 0 9

Figure 1.9 Magnitude and Phase spectra of a rectangular windowed synchronously sampled waveform 10

Figure 1.10 Combined Magnitude and Phase spectra of a rectangular windowed synchronously sampled waveform (N=10,Δ=0) 10

Figure 1.11 Magnitude and Phase spectra of a rectangular windowed asynchronously sampled waveform (N=10,Δ=0.9) 11

Figure 1.12 Combined Magnitude and Phase spectra of a rectangular windowed asynchronously sampled waveform (N=10,Δ=0.9) 11

Figure 1.13 Magnitude and Phase spectra of a Hanning windowed asynchronously sampled waveform (N=20,Δ=0.9) 12

Figure 1.14 Combined Magnitude and Phase spectra of a Hanning windowed asynchronously sampled waveform (N=20,Δ=0.9) 13

Figure 1.15 Illustration of long-range leakage (rectangular windowed and asynchronously sampled waveform) 14
Figure 1.16 Illustration of medium-range leakage (Hanning windowed and synchronously sampled waveform) 15
Figure 1.17 Illustration of short-range leakage (N=10,Δ =0.5) 16
Figure 1.18 Detail of short-range leakage illustration (N=10, Δ=0.5)-frequency range 0.7-1.5 times the fundamental 16
Figure 1.19 DTFT of trapezoidal compensating window (N=10, Δ=0.2) using modified DFT 20
Figure 1.20 DTFT of trapezoidal compensating window illustrating the minimization of short-range leakage (N=10, Δ=0.2) 21
Figure 2.1 The scaled DTFT Plot for the Rectangular Window (N=60, Δ=0.9) 29
Figure 2.2 Scaled DTFT plots for the Hanning and Hamming Windows (N=60, Δ=0.9) 33
Figure 2.3 Scaled DTFT plots for the Blackman and the Fast Decaying 3-term Flat-top windows (N=60, Δ=0.9) 33
Figure 2.4 DTFT plot of the Trapezoidal Compensating Window (N=60, Δ=0.9) .. 37
Figure 2.5 DTFT Magnitude Plots of the Trapezoidal Compensating Windows for A) adjusted, B) not adjusted(N=60, k=2) 37
Figure 2.6 DTFT plots for the Rectangular and Trapezoidal Compensating Windows (N=60, Δ=0.9) 40
Figure 2.7 DTFT plots for the Hanning and Hamming Windows (N=60, Δ=0.9) 40
Figure 2.8 DTFT plots for the Blackman and the Fast Decaying 3-term Windows (N=60, Δ=0.9) 41
Figure 2.9 DTFT plot for rectangular window for N=60 and Δ=[0,1) 43

Figure 2.10 DTFT plots for the Hanning and Hamming windows for N=60 and Δ =[0,1) 43
Figure 2.11 DTFT plots for the Blackman and Fast decaying 3-term windows for N=60 and Δ=[0,1) 44
Figure 2.12 DTFT plots for the TCW for N=60 and Δ=[0,1) 44
Figure 3.1 Expanded DFT Plots for the Rectangular Window in a 2nd harmonic computation (N=60, Δ=0.9) 50
Figure 3.2 Expanded DFT Plots for the Hanning and Hamming Windows in a 2nd harmonic computation (N=60, Δ=0.9) 51
Figure 3.3 Expanded DFT Plots for the Blackman and the Fast Decaying 3-term Windows in a 2nd harmonic computation (N=60,Δ =0.9) 51
Figure 3.4 Expanded Plots for the TCW employing a modified DFT in a 2nd harmonic computation (N=60,Δ =0.9) 52
Figure 3.5 Plot of Equation 3.4.1 53
Figure 3.6 2-level regular sampled PWM waveform 55
Figure 3.7 Plot of PWM based on switching angles in Table 3.4 59
Figure 3.8 Plot of Low-Pass Filtered waveform for parameters and values in Table 3.5 59
Figure 4.1 Block diagram of Fourier analyzer 65
Figure 4.2 Block diagram of Cpumain module 66
Figure 4.3 Block diagram of memory module 67
Figure 4.4 System Memory map 68
Figure 4.5 Timing relationships among timing-controller signals 71
Figure 4.6 Block diagram of Analog-to-Digital interface module 72
Figure 4.7 Block diagram of the Input module 73

Figure 5.1 Program files interactions 75
Figure 5.2 Flowchart of main program code in file AMC.C 78
Figure 5.3 Detailed menu displays 79
Figure 5.4 Flowchart of Module '0' 80
Figure 5.5 Flowchart of Module 1 81
Figure 5.6 Flowchart of module 2 83
Figure 5.7 Flowchart of module 3 84
Figure 5.8 Flowchart of module 4 88
Figure 5.9 Flowchart of Module 5 89
Figure 5.10 Flowchart of module 6 90
Figure 5.11 Flowchart of module 7 91
Figure 5.12 Flowchart of module 8 92
Figure 5.13 Flowchart of module 9 93
Figure 5.14 Flowchart of module 11 94
Figure 5.15 Flowchart of module 15 95
Figure 6.1 Probability density function of quantization error 97
Figure 7.1 RMS reading of a test voltmeter and the Fourier analyzer 116
Figure 7.2 Plot of the Fourier analyzer Amplitude results and fitted square wave ... 118
Figure 7.3 Plot of the Fourier analyzer Amplitude results and fitted triangular wave 118

LIST OF SYMBOLS AND ABBREVIATIONS

Symbol	Description
$\otimes$	Convolution Operator
α_i	ith switching angle for a PWM waveform
∂	Quantization step
$\delta_{unit}(n)$	Unit sample sequence
δ_e	Error in the measurement of the end-corection (Δ)
ε	Relative error in a measurement
ε_M	Maximum value of the relative error
$(\lambda a)_k$	Linear form of the addition errors
$(\lambda a)_m$	Linear form of the multiplication errors
μ_a	Mean of the relative error in the addition of two machine numbers
μ_m	Mean of the relative error in the multiplication of two machine numbers
σ_a^2	Variance of the relative error in the addition of two machine numbers
σ_e^2	Variance of variable 'e'
σ_m^2	Variance of the relative error in the multiplication of two machine numbers
ω	Digital frequency in radians
ω_k	The digital frequency of the kth harmonic component
ω_S	Sampling frequency in radians = 2π
ϕ	Sampling angle in radians
Θ_i	Summation operator based on the TCW
Δ	End correction
Δ_m	Measured value of the end correction
Δ_t	True value of the end correction
Ω_k	The angular frequency of the kth harmonic component of a continous waveform
a_n	The pth term of a sum of cosines window
e	Quantization error
$\hat{e}$	Mean value of quantization error
$f(x,y)$	The true value of a function of variables x and y
$\hat{f}(x,y)$	The computed value of a function of variables x and y
i.i.d	An independently and identically distributed random variable
$var(\lambda a)_k$	Variance of the linear form of the addition errors
$var(\lambda a)_m$	Variance of the linear form of the multiplication errors
w(i)	ith weighting value of window w
x(i)	ith sample of analog signal $x_c(t)$
$x_c(t)$	analog signal

$x_o(i)$	ADC output
$\|\|x(n)\|\|_E^2$	The square of the length of the vector x(n)
y(i)	The product of w(i) and x(i)
A_k	Cosinusoidal component of the kth harmonic of a periodic signal
B_k	Sinusoidal component of the kth harmonic of a periodic signal
C_0	The amplitude of the DC term
$C_k \angle \theta_k$	Harmonic k having amplitude C and phase angle θ
$C_{kc} \angle \theta_{kc}$	Harmonic k having a calculated amplitude C_{kc} and phase angle θ_{kc}
$E(X1_k)$	Expected value of the kth harmonic component of random variable X1
F_S	Sampling frequency in Hertz
I(i)	The ith sample value of a current signal I
M	The maximum harmonic number or for a pulse width modulated signal, the modulation index
N	Number of sampling intervals
$\int_T$	The integral over one period of the signal
S_{win}	The Scale factor required for the DC value of a window to have a unity value.
T	Period of a periodic waveform
T_S	Sampling period in units of time
V(i)	The ith sample value of a voltage signal V
$W(\omega)$	Discrete time Fourier transform
$W_c(\omega)$	Fourier Transform
$W_{rect}(\omega)$	Discrete time Fourier transform of the rectangular window
$W_{scos}(\omega)$	Discrete time Fourier transform of the sum of cosines windows
$W_{tcw}(\omega)$	Discrete time Fourier transform of the trapezoidal compensating window
$X1_k$	Random variable X1 calculated at harmonic k
X_c	The estimate of the kth harmonic component of an analog signal
Y(k)	The estimate of the kth harmonic component of a discrete signal.

1. INTRODUCTION

Accurate harmonic measurements (both amplitude and phase) of voltage and current waveforms, and the subsequent accurate power measurement, have many useful applications. The ability to accurately define the harmonic content of the waveforms allows proper compensation of reactive power, effective reduction of the harmonic content, the placement of loads to meet specified harmonic current limits and correct revenue metering. Another area where precise harmonic measurements is important is in estimating the parameters of pulse-width-modulated (PWM) inverters as used in switching power supplies and motor drive circuitry. Harmonic determination poses a number of problems in cases where accurate measurement of both amplitude and phase components of signals are required. Traditional discrete Fourier type methods which improve the amplitude measurement accuracy, do not improve the phase measurement accuracy even after using other post-processing methods [4].

This introduction describes the concept of sampling, prime sources of measurement inaccuracy and some of the techniques currently employed to minimize these errors. Finally a technique (the TCW algorithm) used to minimize these errors is described.

The impact area of this thesis is in applications where accurate harmonic components determination is difficult to achieve using a single approach. An example being the accurate determination of the harmonics of asynchronously sampled waveforms or a single period band-limited signal when employing discrete Fourier transform type algorithms. The Trapezoidal compensating window algorithm allows precise amplitude and phase information to be obtained without the use of post-processing techniques. DFT algorithms employing classical windows utilize post-processing interpolation or other techniques after the windowing to improve the amplitude measurement accuracy without much phase measurement accuracy improvement.

1.1 Comparison of analog and digital computational approaches

A classification of measuring instruments for harmonic and average evaluation of signals can be made based on the computational approach employed. This classification results in instruments being referred to as either analog or digital. Analog computation suffers from the limitations of impedance matching and component variations with ambient conditions in the implementation of filters and multipliers required to obtain the signal component values. Furthermore, calibration of analog measuring instruments is not easily carried out. The digital approach as implemented in sampling instruments, employs fully digital arithmetic procedures to compute the required parameters. This is easily implemented in digital stored-program systems such as microprocessor-based or DSP-based implementations. In the determination of the average and harmonic components of a signal having an appreciable harmonic content,

the advantages of digital systems outweigh those of the traditional analog instruments. Digital instrument advantages include accuracy and the ease of integration with other computing environments for data transfer, storage and post-signal processing among others. A digital computational approach utilizing regularly spaced signal samples will be used in this thesis.

1.2 Time-Domain sampling: The Sampling Theorem

To process a continuous-time signal by digital processing techniques, it is necessary to convert the signal into a sequence of numbers referred to as the sampled values of the signal or simply samples of the signal. The digital method of obtaining the Fourier series components of the underlying continuous signal determines the accuracy of the harmonic estimation procedure.

Sampling of a continuous signal at fixed (regular) intervals imposes a relationship between the independent variables of time (t) and sample number index (i). That is,

$$t = i\,T_s = \frac{n}{F_s} \tag{1.2.1}$$

where T_S is the sampling period and F_S the sampling frequency.

The relationship between the sampled values and the continuous signal values is the product of the time function and the unit sampling sequence at the sample index as indicated in the expression below,

$$x(i) = x_c(t)\sum_{i=-\infty}^{\infty}\delta_{unit}(t - i\,T_s) \tag{1.2.2}$$

where the unit sampling sequence $\delta_{unit}(i)$ is defined as

$$\delta_{unit}(n) = \begin{cases} 1, & n = 0 \\ 0 & n \neq 0 \end{cases} \tag{1.2.3}$$

Since the Fourier transform of a product of time functions is equal to the convolution of the Fourier transforms of the individual time functions, the Fourier transform of the discrete signal (the discrete Time Fourier transform) of Equation 1.2.2 can be expressed as:

$$\begin{aligned} W(\omega) &= W_c(\omega) \otimes W\left[\sum_{i=-\infty}^{\infty}\delta_{unit}(t - i\,T_s)\right] \\ &= W_c(\omega) \otimes \sum_{i=-\infty}^{\infty}\delta_{unit}(\omega - i\,\omega_s) \end{aligned} \tag{1.2.4}$$

where
$\otimes$ is the convolution operator
i is an integer
ω is the digital frequency,
ω_S the digital sampling frequency having a value of 2π radians.
$W(\omega)$ is referred to as the Discrete time Fourier transform (DTFT),
$W_C(\omega)$ is the Fourier transform of the continuous signal

Equation 1.2.4 reduces to:

$$W(\omega) = \sum_{i=-\infty}^{\infty} W_c(\omega - i\omega_s)$$

When the Discrete Time Fourier transform (DTFT) is computed at discrete frequency values, it is referred to as the Discrete Fourier transform (DFT). In general the DTFT will be employed in depicting the frequency spectrum of sampled signals with the DFT obtained by computing the values at the discrete frequency points.

A bandlimited continuous signal has a spectrum which is zero for $|\omega| \geq B$. An example of the Fourier transform of a bandlimited analog signal is shown in Figure 1.1.

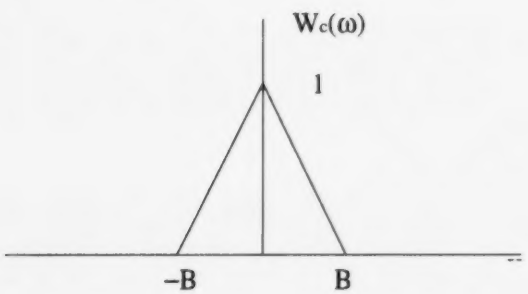

Figure 1.1 An example of the Fourier transform of an analog bandlimited signal.

The Discrete Time Fourier transform of the sampled bandlimited analog signal having a Fourier transform shown in Figure 1.1. is indicated in Figure 1.2.

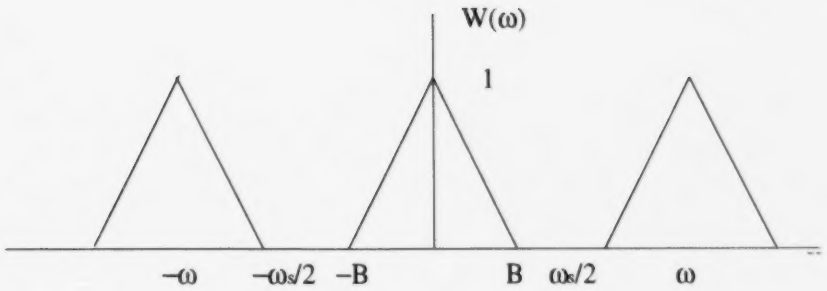

Figure 1.2 The Discrete Time Fourier transform of the sampled analog bandlimited signal with Fourier transform in Figure 1.1.

To reconstruct the original continuous signal entails restoring the original spectrum from the spectrum of the discrete sequence. This can be achieved by employing a filter having a Fourier transform $H_C(\omega)$ as shown in Figure 1.3.

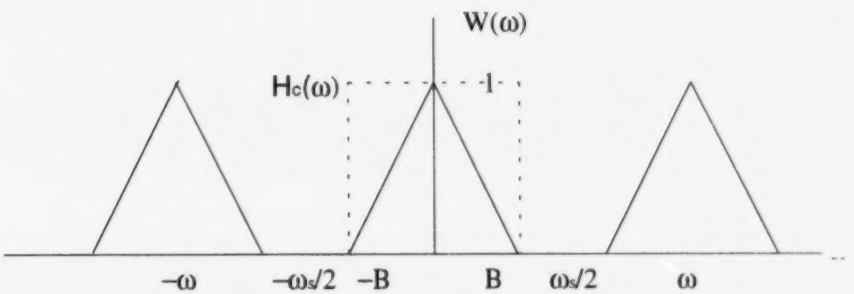

Figure 1.3 The application of a brickwall filter $H_C(\omega)$ for an analog signal reconstruction.

If $B > \frac{\omega_s}{2}$ the Discrete Time Fourier transform will have higher frequency components taking on the identity of lower frequency ones and thus making it impossible to extract the original continuous signal. This phenomena known as aliasing is shown in Figure 1.4.

Hence for signal reconstruction of a digitized band-limited analog signal the sampling frequency should be at least twice the highest signal component in the signal. This is referred to as the Nyquist sampling theorem. The Nyquist frequency is $\omega_S/2$.

To prevent the aliasing of frequency components in the sampling of analog signals, low-pass or band-pass filters referred to as antialiasing filters are introduced in the analog signal path before the signal is sampled. In practical situations the brickwall filter is not easily implemented. The practical filters have decaying frequency components extending beyond the Nyquist frequency. To minimize the interference between the reconstruction filter and the frequency replications occurring at multiples of the sampling frequency, it is convenient to have the maximum signal frequency B at least an order of magnitude less than the sampling frequency (ω_S). As a result, the DTFT expression given by Equation 1.2.4 can be simplified to

$$W(\omega) \approx W_c(\omega)$$

The harmonic determination problem can be viewed as the application of frequency specific filters to obtain the amplitude and phase values of the continuous signal from the underlying analog signal. As a result, the sampling limitations mentioned above should be adhered to.

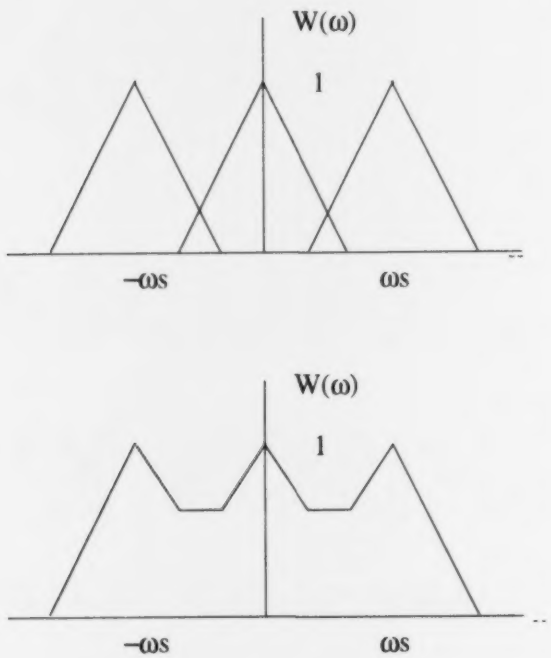

Figure 1.4 Illustration of aliasing.

1.3 Effects of a finite data record length on measurement accuracy

A Fourier series expansion of a signal is the expression of a signal in terms of harmonically related sinusoidal components. For a given finite length data set, the truncated Fourier series results in the best approximation (in a mean-square-error sense) [18]. The determination of the Fourier series components (average and harmonic values) of a signal involves the application of weighting functions (windows) to the sample values and the subsequent use of the Discrete Fourier transform (DFT) or the computationally faster versions (Fast Fourier transform).

In this thesis the digital computational approach used is based on a new windowing method and a modified DFT. This modified form does not lend itself to the use of the fast Fourier transform (FFT). However it is shown that current hardware and operating system platforms produce adequate computational speed for most purposes (see Chapter 7).

To compute either a continuous-time or discrete-time signal, the values of the signal for all time are required. However, in practice, we observe signals for only a finite duration. The sample size can thus be thought of as being viewed through a window. The term windowing is also applied to the further application of various mathematical weighting factors on the finite sample size. The implications of using a finite data record length on the accuracy of the harmonic computation will be examined in this section.

The regularly spaced samples employed in the average and harmonic evaluation can be obtained using two sampling schemes. In a synchronous sampling scheme, the sampling period is an integer multiple of the fundamental period of the measured signal. Asynchronous sampling occurs when the sampling period is not an integer multiple of the fundamental period of the measured signal. In practice, precise synchronous sampling is not easy to achieve and asynchronous sampling thus results. An example of synchronous and asynchronous sampling are depicted in Figure 1.5 and Figure 1.6 respectively.

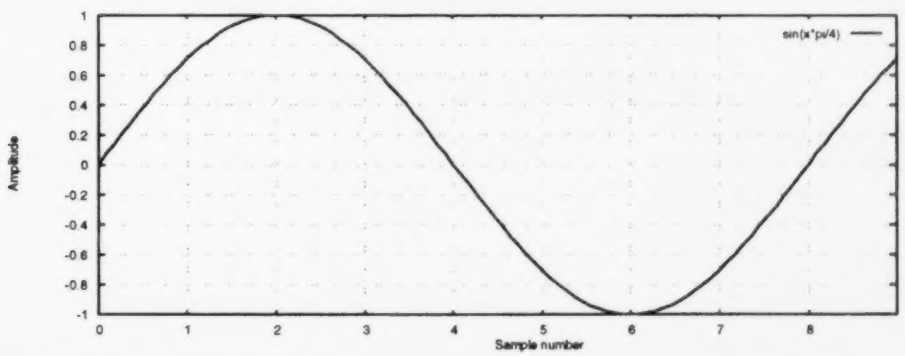

Figure 1.5 Synchronous sampling scheme (1 period = 8 sample intervals).

For a signal having a period T and sampled at a fixed sampling interval T_S, a notation Δ (also referred to as the end-correction) can be introduced. Δ is defined as a fraction of a sampling interval in the range [0,1] such that for N sampling intervals ;

$$(N+\Delta)T_s = T$$

In the example shown in Figure 1.6, Δ=0.5.

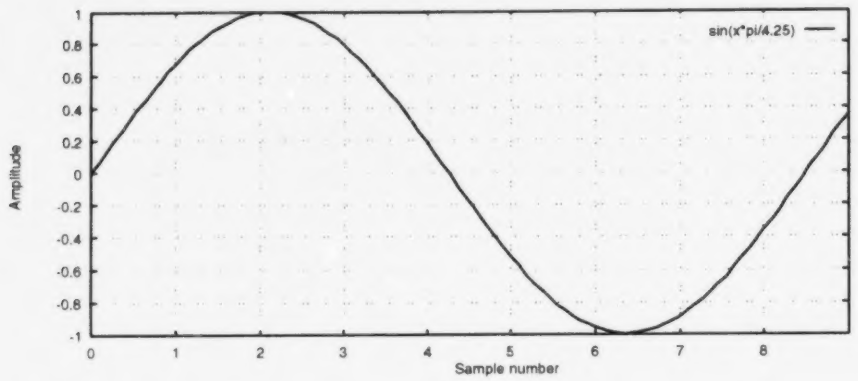

Figure 1.6 Asynchronous sampling scheme (1 period = 8.5 sample intervals). The end-correction (Δ) is thus 0.5

Digital signal processing theory indicates that the nonperfect synchronization between the sampling period and the signal period (asynchronous sampling effect) is the main reason for the measurement errors when the amplitude and phase of the harmonic components of periodic signals are determined by means of digital techniques[12].

Two concepts have thus been introduced namely; sampling and windowing. To simplify the presentation and make comparison with other approaches utilized in the literature, the effects of these concepts will be examined from the viewpoint of a sampled window. For simplicity, the sampled window will be referred to as a window or windowing function.

Letting {x(i)} denote a sequence to be analyzed. Limiting the duration of the signal to N samples in the interval [0,N-1] is equivalent to multiplying {x(i)} by a rectangular window of length N. That is, {y(i)}

$$y(i) = w(i)x(i) \tag{1.3.1}$$

where the rectangular window w(i) is,

$$w(i) = \begin{cases} 1, & 0 \le i \le N-1 \\ 0, & otherwise \end{cases} \tag{1.3.2}$$

Various windows or weighting functions are used. Some common windows are plotted in figure 1.7

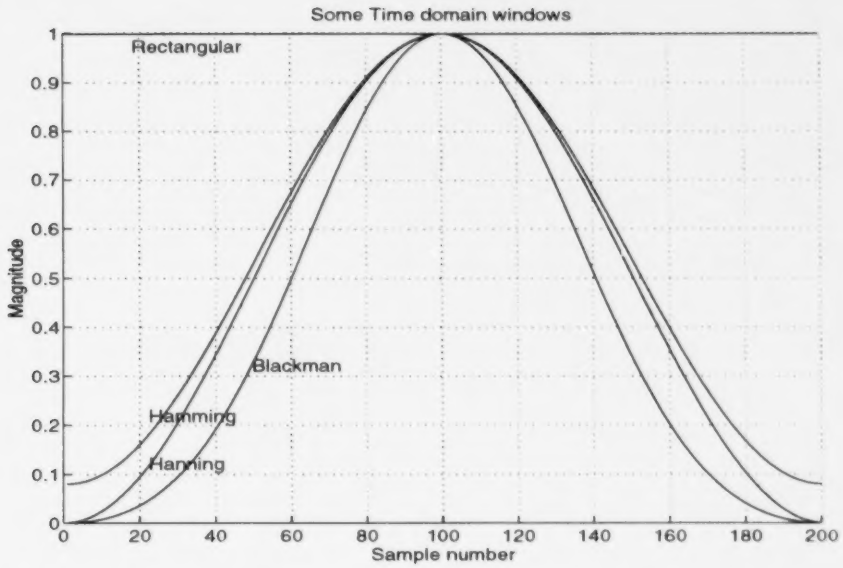

Figure 1.7 Plots of some windows

Now suppose that the sequence consists of a single sinusoid, that is,
$x(i) = \cos(i\omega_0)$
Then the DTFT of the finite-duration sequence x(i) may be expressed as:

$$Y(\omega) = \frac{1}{2}\left[W(\omega - \omega_0) + W(\omega + \omega_0)\right] \tag{1.3.3}$$

where W(ω) is the DTFT of the window sequence, which for the rectangular window is given by,

$$W(\omega) = \frac{\sin\frac{N\omega}{2}}{\sin\frac{\omega}{2}} e^{-\frac{j(N-1)\omega}{2}} \tag{1.3.4}$$

Figure 1.8 indicates the DTFT of this window plotted for positive and negative frequency values. The windowed spectrum is not located at a single frequency, but instead the original power in the signal has been spread by the window into the entire frequency range. This phenomenon, which is characteristic of windowing the signal, is called 'spectral leakage' or simply 'leakage'. As noted previously the DFT is computed at the harmonic frequencies. Hence, signal harmonic frequency components at the amplitude null points of the DTFT will not contribute components to the determination of other harmonic components. However, if the harmonic components

of the signal do not occur at the null points of the magnitude spectrum of the DTFT, these components will contribute to the measured harmonic and give rise to inaccuracies in the measurement.

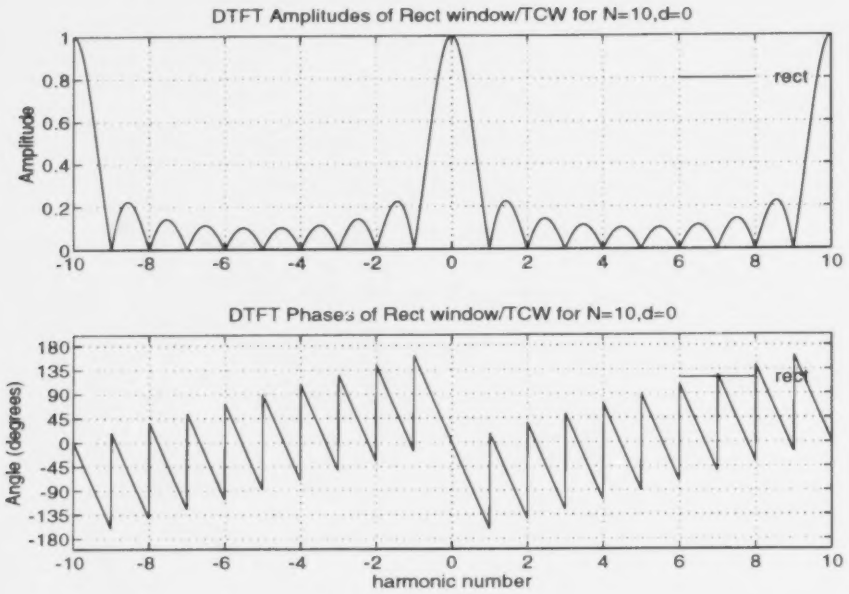

Figure 1.8 The DTFT of a rectangular window for N=10 and Δ=0

The symmetrical nature of the rectangular window is also a property of all other windows. As a result all subsequent plots of the DTFT of any window will be made for only positive frequency values.

Figure 1.9 indicates the individual Magnitude and Phase spectra of a synchronously sampled signal (Δ=0) having equal amplitudes for the fundamental and second harmonic. It can be seen that the amplitude nulls occur at the harmonic frequencies. Hence spectral leakage should not exist.

The effect on the DFT value of say the fundamental due to a second harmonic signal will be the sum of the two window values (one centered at the fundamental and the other centered at the 2nd harmonic) evaluated at the first harmonic. In order words the harmonic value at a particular frequency is due to the sum of the DFTs of all the other signals computed at the frequency of interest. This concept is explained in detail in the second chapter.

The absence of spectral leakage is confirmed by the plot of the combined DTFT in Figure 1.10, indicating that the amplitude and phases of the DTFT at the fundamental and second harmonic frequencies are the true values ($1\angle 0$).

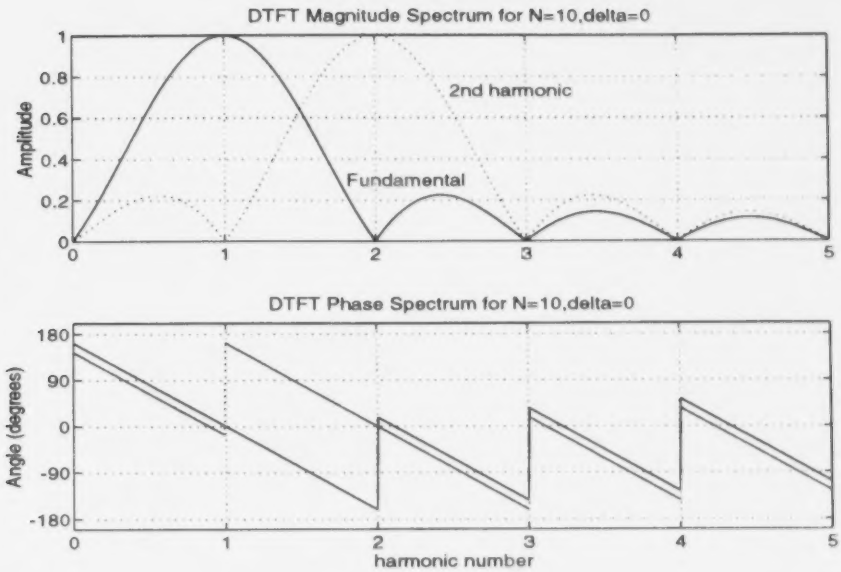

Figure 1.9 Magnitude and Phase spectra of a rectangular windowed synchronously sampled waveform

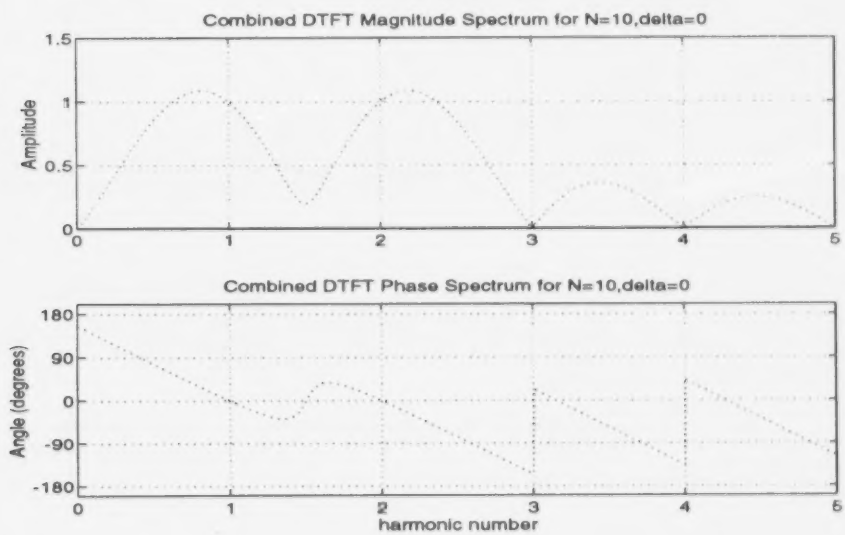

Figure 1.10 Combined Magnitude and Phase spectra of a rectangular windowed synchronously sampled waveform (N=10,Δ=0)

Figure 1.11 indicates the individual magnitude and phase spectra of an asynchronously sampled signal (Δ=0.9) having equal amplitudes for the fundamental and second harmonic. The rectangular window has been applied in this instance. It can be seen that the amplitude nulls do not occur at the harmonic frequencies. Hence

spectral leakage should exist as seen by the combined DTFT in Figure 1.12. This results in the DTFT values at the fundamental and second harmonic frequencies not being equal to unity with a zero degree phase angle.

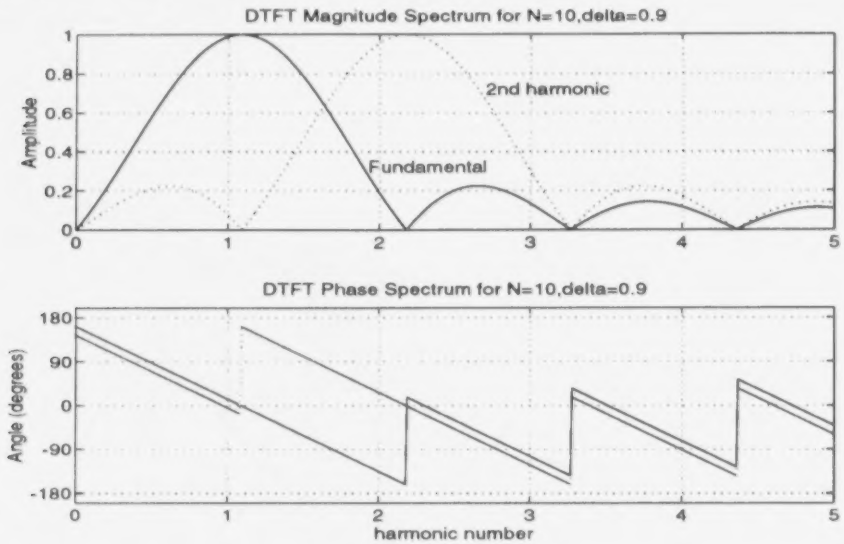

Figure 1.11 Magnitude and Phase spectra of a rectangular windowed asynchronously sampled waveform (N=10, Δ=0.9).

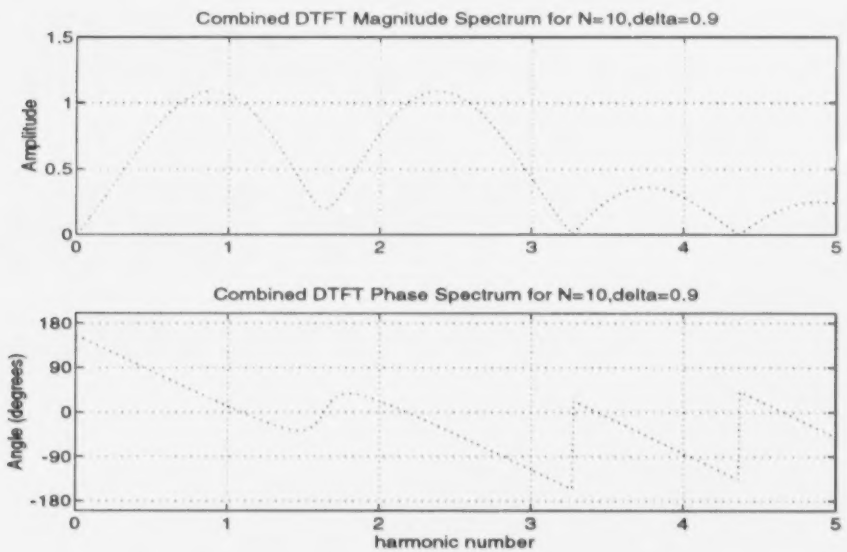

Figure 1.12 Combined Magnitude and Phase spectra of a rectangular windowed asynchronously sampled waveform (N=10,Δ=0.9)

In the DFT computation the record length of the sampled and windowed signal is a period of an infinite signal. Hence since an asynchronously sampled signal does not fall off smoothly to fixed values at both ends of the data record length, the sharp transitions implies a number of high frequency components. This is another viewpoint of the leakage effect. Hence the application of non-rectangular window functions employed primarily to reduce leakage effects in the computation of the harmonic components by a Discrete Fourier transform approach, when the record length is not an integral multiple of the fundamental period of the input waveform.

An example of a non-rectangular window is the Hanning window expressed as

$$w(i) = \begin{Bmatrix} 0.5(1-\cos\frac{2\pi}{N}i), & 0 \le i \le N-1 \\ 0, & otherwise \end{Bmatrix} \qquad (1.3.5)$$

Figure 1.13 indicates the DTFT of the Hanning window when used in determining the Fourier coefficients of a signal having a 2nd and 4th harmonic component but a very small fundamental component. This comparison is used due to the wide main lobe of the Hanning window. The signal is asynchronously sampled with N=20 and Δ=0.5. The low side lobes of the Hanning window would be expected to result in minimal leakage as evidenced in figure 1.14.

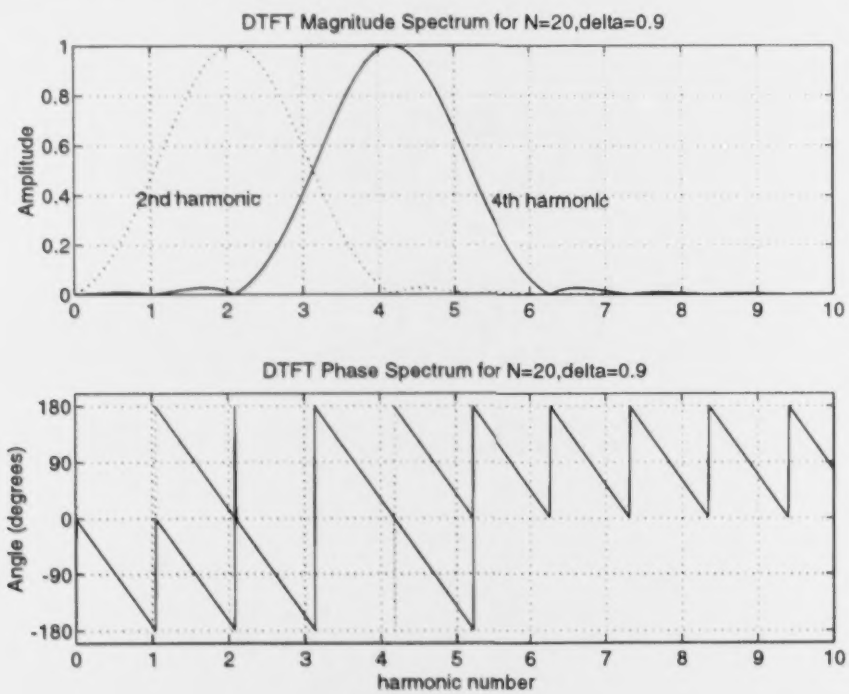

Figure 1.13 Magnitude and Phase spectra of a Hanning windowed asynchronously sampled waveform (N=20, Δ=0.9).

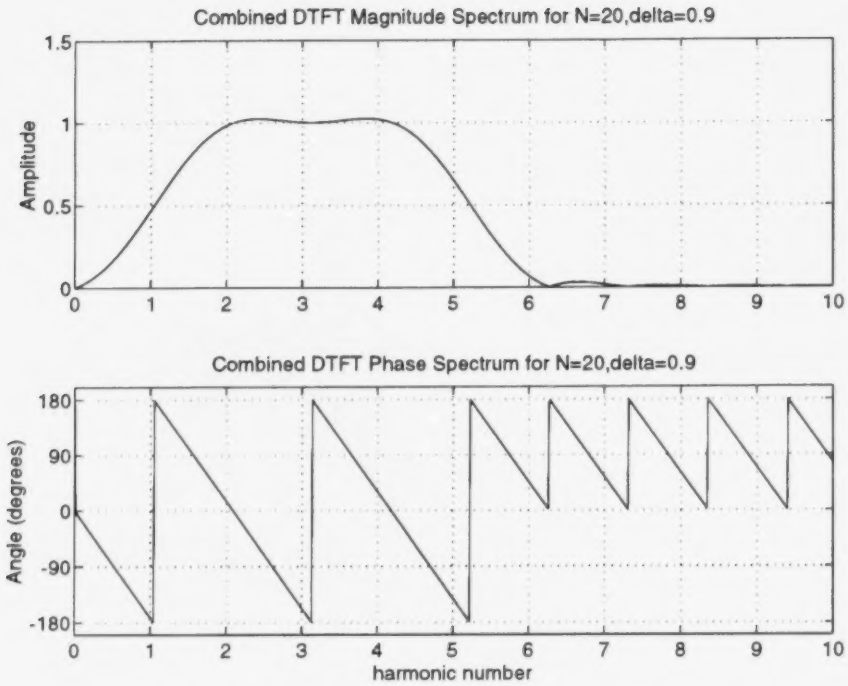

Figure 1.14 Combined Magnitude and Phase spectra of a Hanning windowed synchronously sampled waveform (N=20,Δ=0.9)

The leakage effects which arise due to the finite window length (or a finite sample size) and the computation algorithm used can be classified into three groups: long-range, medium-range and short-range [4].

Long-range leakage occurs in asynchronous sampling and results in all frequency components contributing to the computed value of the l^{th} harmonic component instead of only the l^{th} harmonic component itself. Thus this error depends on all the harmonic components of the signal as well as all the side-lobes of the Fourier transform of the window employed. To reduce this error, the amplitude of the Fourier transform of the window employed should be as small as possible at the actual signal harmonic frequencies.

Figure 1.15 illustrates the existence of long-range leakage on the DC measurement. This can be inferred from the previous descriptions of spectral leakage due to the non-zero amplitude values of the window DTFT at the harmonic points. Hence for a signal having a magnitude of 0.75 for the fundamental, and 0.5 for the 2nd harmonic as shown on the plot, both the fundamental and second harmonic can contribute an error to the measurement of the DC value.

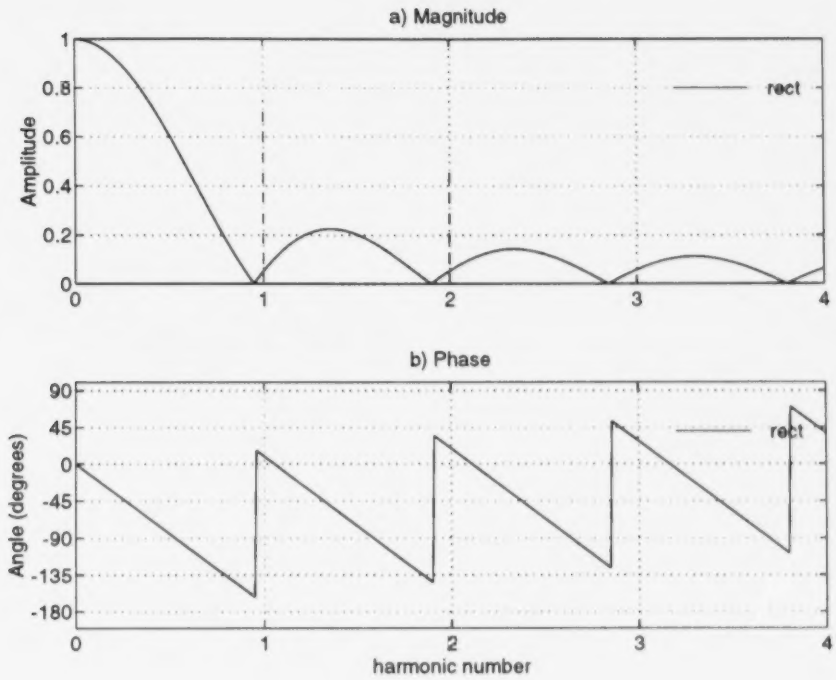

Figure 1.15 Illustration of long-range leakage (rectangular windowed and asynchronously sampled waveform)

Medium-term leakage depends on the adjacent harmonic components of the signal as well as the main lobe of the window employed. This type of leakage which determines the resolution of the window used, can occur even when the signal is synchronously sampled. For windows with wide main lobes and low side-lobes, this error can be minimized by using a sample set which results in the 1st harmonics not intersecting the main lobe. This can be achieved by increasing the number of cycles of the input signal spanned by the sample set. In particular, for a synchronously sampled signal employing a Hanning window, at least 2 input signal periods are required.

The effect of medium-range leakage on the DC measurement is illustrated in Figure 1.16. The Discrete time Fourier transform (DTFT) of a Hamming window is used. Synchronized sampling occurs in this example since Δ=0. The DTFT of this window has a non-zero value at the fundamental (for a single cycle time record). Hence a signal fundamental having a non-zero amplitude will contribute an error to the measurement of the DC value as shown in Figure 1.16.

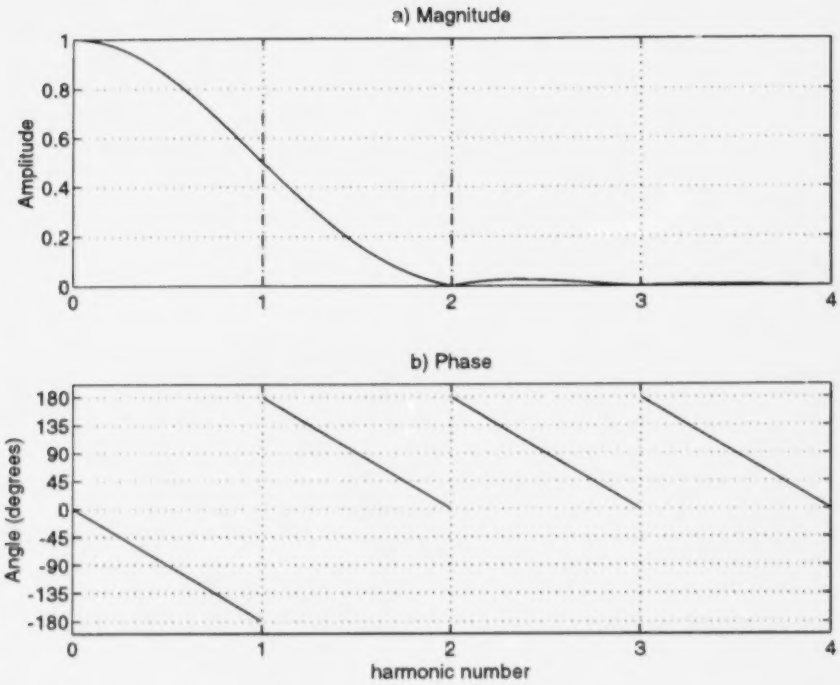

Figure 1.16 Illustration of medium-range leakage (Hanning windowed and synchronously sampled waveform)

Short-term leakage is concerned only with the l^{th} harmonic component itself and the main-lobe of the Fourier transform of the window employed. This results when the main lobe of the DFT of the window reaches its peak value at frequency values which are not the harmonic frequencies of the input signal. It should be noted that this error cannot be reduced by solely employing a typical DFT algorithm which computes values at integral multiples of 1/N, while the actual harmonic components are at integral multiples of $1/(N+\Delta)$. To minimize this type of error additional correction schemes are generally employed.

Figure 1.17 illustrates the effect of short-range leakage on the determination of the harmonic components of a sinusoid having unity amplitude and zero phase, using the DFT and a rectangular window. It can be observed the window peak occurs at a frequency equal to 10.5/10 times the fundamental signal frequency (i.e. $(N+\Delta)/N$). This latter mentioned frequency is where the zero phase angle occurs in the phase plot. An expanded view of the DTFT plot of the window for a frequency range of 0.7-1.5 times the fundamental is illustration in Figure 1.18.

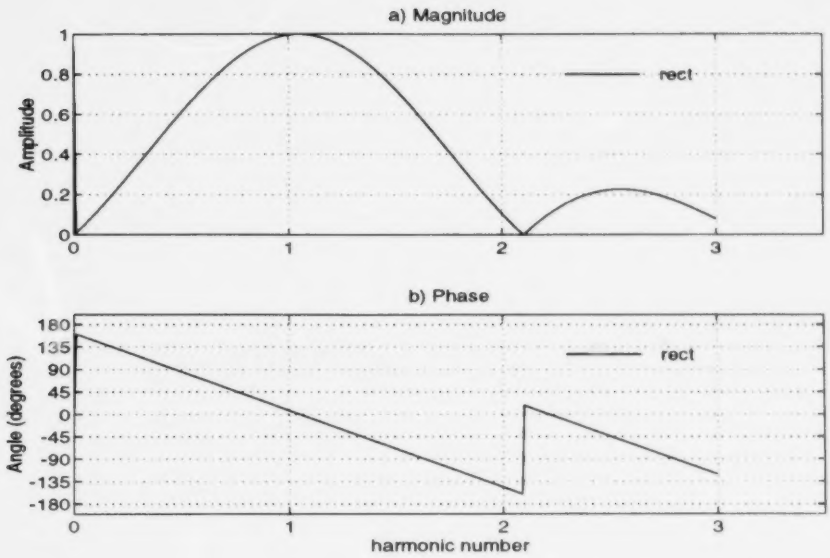

Figure 1.17 Illustration of short-range leakage (N=10, Δ=0.5)

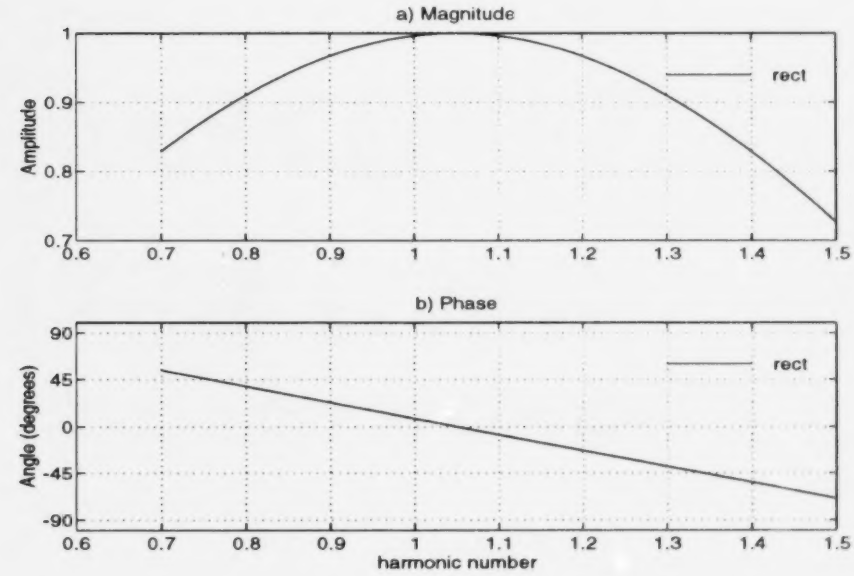

Figure 1.18. Detail of short-range leakage illustration (N=10, Δ=0.5)-frequency range 0.7-1.5 times the fundamental

1.4 Summary of desirable window characteristics for leakage minimization

For the purpose of this thesis, windows will be classified into two groups. In the classical windows group the weighting functions employed do not use the knowledge of the end-correction. The alternate compensating windows group use the end-correction. Examples of classical windows are the rectangular and Hanning. The weighting function employed in the Stenbakken[16] approach is an example of a compensating window (Refer to section 1.5). From section 1.3. it can be seen that average measurements are affected by both long and medium-term leakage. The general signal harmonic measurement on the other hand can be affected by all three forms of leakage. A summary of desirable window characteristics for precise measurements are summarized in Table 1.1 based on the explanations in section 1.3.

TABLE 1.1 Window characteristics required for Accurate harmonic measurements (Amplitude and Phase)

Leakage effect to be minimized	Desired Windows Characteristics
Long-term	Low transform values at harmonic frequencies
Medium-term	Very narrow window main lobe
Short-term	Very narrow main lobe. DFT basis vectors at actual frequencies

1.5 Techniques for precise signal average value measurements

Computation of the average value of a signal involves the determination of the mean of the time integral of the quantity under consideration. For a periodic signal, this quantity is computed over a period of the signal. In the digital computation scheme, a numerical integration is used. Numerical integration techniques indicate that the application of the composite trapezoidal rule to an integral of a periodic signal results in the best estimate (least error) for the integral of the signal [8]. In the absence of aliasing and a synchronously sampled waveform, the numerical integration result is exact. For a synchronously sampled signal (Figure 1.1), using the composite trapezoidal rule is equivalent to taking the mean of the sum of the samples. Turgel [17] utilized this idea in the implementation of a digital wattmeter. To insure synchronized sampling, a phase locked loop system was used to generate the timing pulses for the analog-to-digital converters. This instrument produced accurate results for signals having a stable frequency within the data record length. The issue of maintaining synchronization in situations where a sudden signal frequency change could occur resulted in the search for improved measurement methods. An example of such a situation is in the measurement of the frequency of the signal injected on the terminals of a DC motor by the commutation process.

In general, the complexity of the sampling interval generator in a data acquisition system is reduced when a fixed sampling scheme is used. This economic benefit generally results in the reduction of the measurement accuracy. The need for an improved algorithm for precise DC measurements in fixed-sampling interval instruments led to the National Bureau of Standards (NBS) wattmeter by Stenbakken [16] employing 12-bit analog-to-digital converters. This instrument was later upgraded to a 16-bit version [15]. Both wattmeters used a fixed sampling scheme, and a sample set covering more than one cycle of the fundamental. Furthermore both instruments incorporated a unique feature namely; the incorporation of an estimate for the end-correction (Δ) in an averaging routine (an extension of Turgels' [17]) in order to compute the signal average value. The end-correction was estimated by using the cycle counter value and the sample counter data.

Another researcher, Zu-Liang [22] examined some theoretical aspects resulting from incorporating the end-correction (Δ) in a trapezoidal scheme. This scheme resulted in a far lower error compared to the compensating average scheme used by Stenbakken. In addition, Zu-Liang proposed an interpolation scheme for determining the end-correction using the signal samples. A digital sampling wattmeter employing a hardware approach to the determination of the end-correction has been implemented[11]. In the wattmeter implementation, the end-correction Δ was also incremented by one whenever Δ was in the range (0.5-1). This method of constraining the value of Δ to the range [-0.5,0.5] resulted in an improvement in the measurement accuracy. Nyarko and Stromsmoe [9,10] extended Zu-Liangs' work with the error expressions for the various processing methods (algorithms) being further analyzed and presented in a manner relevant to actual hardware implementations. The inclusion of simulation results to determine the number of samples required to achieve a particular worst case error was an aid to a system hardware choice to meet a required accuracy figure. Refer to Chapter 2 for further details of the algorithm.

1.6 Traditional harmonic measurements based on windows and the DFT

The Discrete Fourier transform (DFT) is one of the usual means of determining the harmonic coefficients of a signal since it has the advantage of producing the best linear unbiased estimation of the Fourier coefficients of periodic signals (in the least mean square sense) in the presence of covariant and noncovariant errors in the observations (e.g. noise) [18].

The use of time domain classical windows having smoother edges to reduce the discontinuities at the data set boundaries has been the normal procedure to minimize the undesired harmonic interference due to leakage effects [6]. The price paid in such implementations is the increase in the width of the main lobe of the windows employed. A wide main lobe can cause medium-range leakage especially where only a single cycle of the input waveform is available. However, an advantage to using classical windows is that it easily leads to the subsequent use of computationally faster Discrete Fourier transform (DFT) algorithms such as the fast

Fourier transform (FFT). The approaches to the elimination of the amplitude errors due to short-term leakage are the use of simple interpolation methods [1],[5] and [7] as well as using flat-top windows. This increased accuracy in the harmonic amplitude determination, is generally achieved at the expense of an increased computational burden.

Zero padding of the input sample set is another technique employed to improve measurement accuracy. This involves adding extra samples of value zero to increase the data record length. In some instances it is used to meet the sample set size requirement of a particular FFT algorithm. A DFT performed on a zero-padded sample set simply results in a frequency interpolation of the non-zero-padded signal DFT. That is, the DFT plot contains extra values of the DTFT of the window employed. This effect of adding L zeros to a data record of length N can be intuitively explained as follows. Adding an infinite number of zeros to a given data record will result in an aperiodic signal whose Fourier transform will be equal to the DTFT. As the number of zeros are decreased the DTFT will be sampled at increasing frequency interval which are integral multiples of $2\pi/(N+L)$ until with no zero padding, the DTFT will be sampled at frequency intervals which are integral multiples of $2\pi/N$. This form of frequency domain interpolation of the spectrum should be used judiciously and the results interpreted with care. This is because the extra harmonics already present due to asynchronous sampling will be accentuated giving a false impression of the existence of components not present in a period of the original signal.

Generally the techniques discussed above give some improvements on the determination of harmonic amplitude values. The down side is that the phase measurement accuracy is not improved [4] since, in general, errors due to short-term leakage effects are not adequately dealt with.

1.7 Algorithm employed in thesis (TCW and modified DFT)

The compensating window in the digital sampling wattmeter [11] is used in this thesis. This is a modification of Zu-Liangs' trapezoidal correction as explained in Section 1.5.
This window is defined as.

$$w(i)=\begin{Bmatrix} 0.5+\dfrac{\Delta}{2}, & i=0 \\ 1, & 1\le i\le N-1 \\ 0.5+\dfrac{\Delta}{2}, & i=N \end{Bmatrix} \qquad (1.7.1)$$

The DTFT of this window is

$$W(\omega) = \left[\frac{\sin\frac{N\omega}{2}}{\sin\frac{\omega}{2}} \cos\frac{\omega}{2} + \Delta \cos\frac{N\omega}{2} \right] \cdot e^{\frac{-jN\omega}{2}} \tag{1.7.2}$$

This window improves the measurement accuracy of the average value of a signal since it minimizes long and medium-range leakage effects. An illustration of this effect is given in figure 1.19 for a signal sampled asynchronously and resulting in Δ having a value of 0.2.

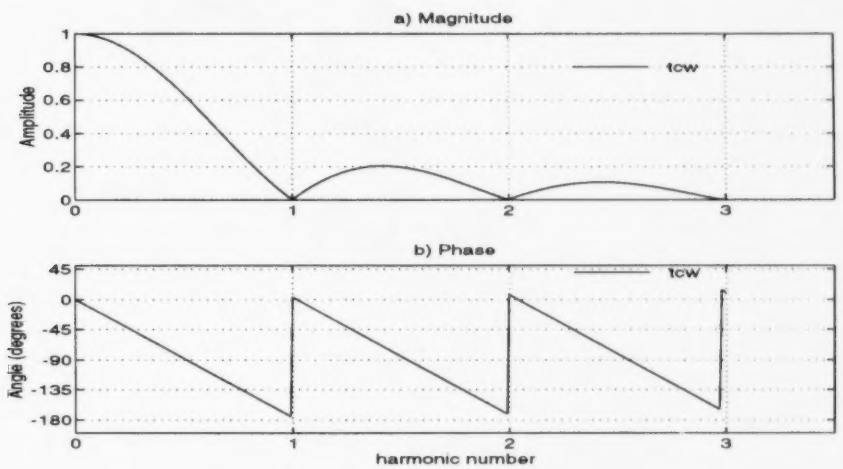

Figure 1.19 DTFT of trapezoidal compensating window (N=10, Δ=0.2) using modified DFT

The DFT approach to harmonic determination is also based on the averaging of the integral of exponentially scaled sample values. This leads to a natural extension of the trapezoidal compensating window for use in the general harmonic determination problem. In this thesis, a modified DFT is used, where the arguments of the exponential terms are adjusted from those normally used in DFT computations, to make them coincide exactly to the harmonic of interest. This can be done since Δ can be determined and incorporated in the computation, unlike schemes that use the classical windows. Examination of the Fourier transform of the trapezoidal compensating window (TCW) indicates a main lobe which has a width which varies with Δ. The main lobe varies in order to maintain minimal leakage at the actual harmonic points. Hence certain figures of merit of the regular classic windows cannot be applied to this scheme and thus other common grounds for comparison should be used. This scheme, like the rectangular window (an averaging approach), requires only

a single cycle of the input signal which is advantageous in a number of cases. The reduction in short-range leakage is illustrated in the example of figure 1.20 where the fundamental is being computed using the modified DFT.

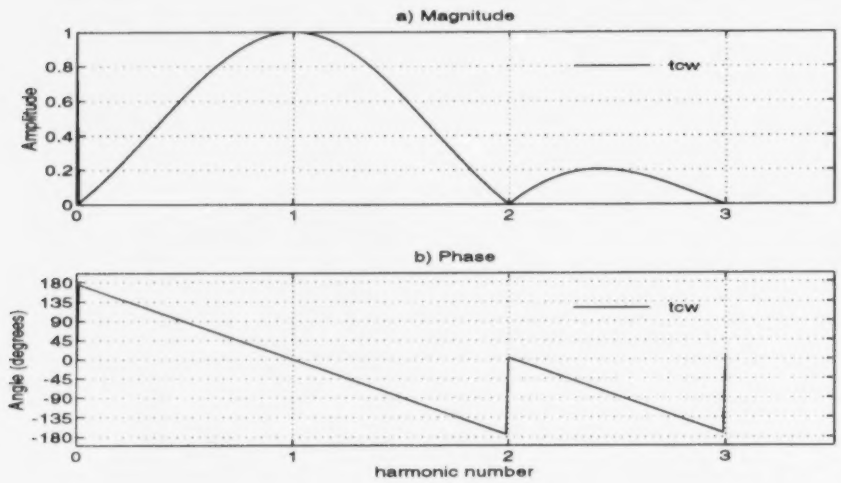

Figure 1.20 DTFT of trapezoidal compensating window illustrating the minimization of short-range leakage (N=10, Δ=0.2)

The TCW approach utilized in this Fourier analyzer is thus seen to minimize both amplitude and phase errors. The analyzer as implemented utilizes a fixed sampling interval scheme derived from the system clock, since it is easily implemented, as well as being cost-effective. Provision has however been made to generate the sampling interval from a multiple of a trigger source frequency derived from an input signal. This allows an FFT to be used when Δ is zero. Economic considerations prevented the inclusion of the necessary hardware in this prototype. The end-correction can be determined by a hardware scheme to an arbitrary degree of accuracy. Since the sampling interval is fixed, any number of frequency multiplication schemes can be utilized to obtain an integral number of smaller pulses per sampling period. A counter clocked at the frequency of the pulses can then have its count value held at the end of a period. This Fourier analyzer which is based on a prototype of the previously designed sampling wattmeter [11], utilizes such an approach with a 4-bit counter. In this instrument, the end correction Δ can thus be resolved to 1 in 16 parts. The sampling instrument employs 12-bit analog-to-digital devices. The analyzer is based on an 8MHz 68000 microprocessor implementing floating point computations in software. This processor with its' lack of multiply-accumulate type instructions results in slow computations. As previously stated, in addition to the spectrum analysis function utilizing a TCW and modified DFT, frequency measurement for signals from dc-1kHz are performed. The input voltage range is -500V to +500V. The input current range is -10A to +10A. The objectives of a user-friendly menu-driven software

interface and easy to maintain hardware were also given due considerations in the system design and construction cycle.

Table 1.2 indicates the summary of the algorithm employed and its effect on leakage errors

TABLE 1.2 Summary of how the TCW Algorithm reduces leakage errors

Procedure	Leakage type minimized
The use of a window based on a trapezoidal integration scheme, incorporating a correction for an asynchronous sampling scheme.	long and medium-range leakage
A modified DFT algorithm employing exponents which ensure the computation of the harmonic components at the signal harmonic frequencies.	Short-range leakage

1.8 Summary of windows properties for leakage error reduction

In Table 1.3, a summary of the properties of the classical and compensating type windows with respect to leakage error reduction, is listed.

TABLE 1.3 Summary of window properties for leakage error reduction

Leakage type	Classical Windows	Compensating Windows
Long-term	Low side-lobe	Low transform values at harmonic frequencies
Medium-term	Very narrow main-lobe	Very narrow-main lobe
Short-term	Flat-top main lobe and very narrow main-lobe	Very narrow main lobe. DFT basis vectors at actual frequencies

1.9 Thesis organization

To unify the theoretical ideas and ease the comparison in the presentation of the average and harmonic computation procedure, the various processing methods are treated as windowing functions, with their frequency responses indicated by their Fourier transforms (refer to Chapters 2 and 3). The effect of long and medium range leakage and its reduction is examined under the measurement of the average of a signal in Chapter 2. Short-range leakage and its reduction is examined under harmonic measurements in Chapter 3. In addition the approach used is compared with some

classical windows for a couple of cases. The hardware platform used is introduced in the fourth chapter and this is followed by the software scheme in the fifth chapter. The effect of quantization and computational errors is examined in the sixth chapter. In the seventh chapter the system performance is obtained. In addition the results of the simulations of the algorithm on some hardware and operating system platforms are included for comparison. The conclusion incorporates suggestions for further work which can be done to improve upon this thesis.

2. AVERAGE VALUE MEASUREMENT APPROACHES

The accurate measurement of the average value of a signal using DFT type algorithms entails reducing the primary sources of error (long-range and medium-range leakage effects). The process of obtaining the arithmetic mean of a set of signal samples is a special case of a DFT type algorithm. A typical example of the average evaluation is the determination of the active power of a distorted electrical power signal. An appropriate form for a signal representation for error analysis purposes is introduced (see Section 2.1). The analysis procedure is then developed to show that the error effects can be easily analyzed and comparisions between various procedures may be made when each computational approach is viewed as the application of windowing functions to the sampled signal values. The DTFT of some traditional windows are derived as well as that of the TCW. Examples are introduced to compare the effectiveness of the various windowing approaches in improving the average measurement accuracy by reducing the long-range and medium-range errors.

2.1 Fourier series representation of signals

A trigonometric set of functions can be used to represent a periodic time function $x_c(t)$ satisfying the Dirichlet conditions. This approach is known as a Fourier series representation of a signal and involves expressing the signal as a sum of an infinite number of harmonically related sine and cosine terms. The Dirichlet conditions are:

1) $\int_{t_1}^{t_1+T} |x_c(t)|dt$ is finite for any t_1, where T is the period of $x_c(t)$.

2) There are a finite number of maxima and minima in any finite time period.

3) There are a finite number of discontinuities in any finite time period.

Any time function $x_c(t)$ corresponding to an actual physical signal will always satisfy the Dirichlet conditions.

A Fourier series expansion for a band-limited periodic signal x(t) can be expressed as:

$$x_c(t) = C_0 + \sum_{k=1}^{M} C_k \cos(\Omega_k t - \theta_k) \qquad (2.1.1)$$

where
M = The maximum harmonic(k),
C_0 = The amplitude of the DC term (average value),
C_k = The kth harmonic component amplitude
and

$$\Omega_k = \frac{2\pi k}{T}$$

with T being the fundamental period.

The Fourier series expansion terms, C_0, and C_k result in the 'best-fit' (in a mean-square-error sense) for the signal $x_C(t)$.

Substituting the expression for Ω_k in equation 2.1.1, results in:

$$x_c(t) = C_0 + \sum_{k=1}^{M} C_k \cos(\frac{2\pi k}{T} t - \theta_k) \tag{2.1.2}$$

which can be expanded to:

$$x_c(t) = C_0 + \sum_{k=1}^{M} C_k \cos\theta_k . \cos(\frac{2\pi k}{T} t) + C_k \sin\theta_k . \sin(\frac{2\pi k}{T} t) \tag{2.1.3}$$

It can easily be shown that the DC term, C_0, can be determined by:

$$C_0 = \frac{1}{T} \int_T x(t) dt \tag{2.1.4}$$

where $\int_T$ means integrating over one period of the signal

2.2 Spectrum Analysis for Discrete-Time signals

Discrete-time signals (hereafter referred to as discrete signals) are signals defined at discrete times. A practical system involving the use of an analog-to-digital converter (ADC) applied to a continuous signal actually produces a digital signal (discrete time and amplitude). If the quantization error is assumed negligible or non-existent, then the ADC could be thought of as producing discrete signals. This will be the assumption employed in this chapter. This assumption is a valid one, since it can be shown that the quantization errors can be examined independently (Refer to Chapter 7).

An analogy to the continuous signal approach will be employed in the determination of the Fourier series components of discrete signals. This is generally known as the Discrete Fourier transform (DFT) approach.

Ignoring the quantization error, the sampled values $x(i)$ obtained when Equation 2.1.2 is uniformly sampled with a sampling interval T_S is:

$$x(i) = C_0 + \sum_{k=1}^{M} C_k \cos(\frac{2\pi k T_s}{T} i - \theta_k) \tag{2.2.1}$$

or

$$x(i) = C_0 + \sum_{k=1}^{M} C_k \cos(i\omega_k - \theta_k) \tag{2.2.2}$$

where

$$\begin{aligned} \omega_k &= \frac{2\pi k T_s}{T} \\ &= \frac{2\pi k T_s}{(N+\Delta) T_s} \\ &= \frac{2\pi k}{N+\Delta} \\ &= k\phi \end{aligned} \tag{2.2.3}$$

where T_s is the sampling interval.
ϕ is defined as the sampling angle with $(N+\Delta)\phi = 2\pi$.
$\Delta \in [0,1)$ as previously explained in the introductory chapter.

2.3 DC value Computation and Windows

Making reference to the general equation for a sampled multi-frequency periodic signal; (Equation 2.2.2)

$$x(i) = C_0 + \sum_{k=1}^{M} C_k \cos(i\omega_k - \theta_k)$$

it is noted that any method employed in the determination of the DC value (C_0) of the signal, should effectively have the measurement contributions of the harmonic components being zero or very close to zero. The pertinent leakage effects which need to be reduced are those due to the long term and medium term effects. The short term leakage does not affect the accurate measurement of the DC value.

The computation of the DC term can be expressed as:

$$\begin{aligned} Y(0) &= S_{win} \cdot \sum_i w(i)x(i) \\ &= S_{win} \cdot \sum_i y(i) \end{aligned} \tag{2.3.1}$$

where
Y(0) is the estimate of the DC term C_0.
$w(i)$ is the i_{th} window function value.
and S_{win} is the scale factor required for the window employed.

Thus:

$$
\begin{aligned}
Y(0) &= S_{win}\sum_i\left[w(i)C_0+\sum_{k=1}^{M}\frac{C_k}{2}\left\{e^{-j\theta_k}w(i)e^{ji\omega_k}+e^{j\theta_k}w(i)e^{-ji\omega_k}\right\}\right] \\
&= S_{win}\cdot\sum_i w(i)C_0+S_{win}\cdot\sum_i\left[\sum_{k=1}^{M}\frac{C_k}{2}\left\{e^{-j\theta_k}w(i)e^{ji\omega_k}+e^{j\theta_k}w(i)e^{-ji\omega_k}\right\}\right] \\
&= C_0\cdot S_{win}\sum_i w(i)+S_{win}\sum_i\left[\sum_{k=1}^{M}\frac{C_k}{2}\left\{e^{-j\theta_k}w(i)e^{ji\omega_k}+e^{j\theta_k}w(i)e^{-ji\omega_k}\right\}\right] \\
&= C_0\cdot S_{win}\sum_i w(i)+S_{win}\cdot\sum_{k=1}^{M}\frac{C_k}{2}\left\{e^{-j\theta_k}\sum_i\left[w(i)e^{ji\omega_k}\right]+e^{j\theta_k}\sum_i\left[w(i)e^{-ji\omega_k}\right]\right\} \\
&= C_0\cdot S_{win}\sum_i w(i)+\sum_{k=1}^{M}\frac{C_k}{2}\left\{e^{-j\theta_k}S_{win}.W(-\omega_k)+e^{j\theta_k}S_{win}.W(\omega_k)\right\}
\end{aligned}
$$

(2.3.2)

$W(\omega_k)=\sum_i\left[w(i)\cdot e^{-ji\omega_k}\right]$ is the value of the Fourier transform of the window values w(i) evaluated at the frequency ω_k. This is termed the discrete time Fourier transform (DTFT). Ideally the DC measurement on a signal with an appreciable harmonic content should produce:

$$Y(0)=C_0$$

As a first step, from Equation 2.3.2, for a given window with values w(i), S_{win} should be chosen to satisfy the following equation:

$$S_{win}\cdot\sum_i w(i)=1$$

It can be noted from Equation 2.3.2 that the window DFT values at the harmonic frequencies ω_k will give an error contribution to the measurement of the DC value. Ideally, the sum of all error contributions should be zero. This could also be achieved by having each error contribution being zero. Each error contribution can be expressed as a phasor quantity having a magnitude and phase. Obviously, a zero magnitude and phase are desirable. Where the latter conditions cannot be met, then a

small magnitude value and a small angular deviation from zero or 180 degrees is desirable.

The scaled Fourier transform $S_{win}W(\omega_k)$ of various windows will be analyzed and compared with that of the trapezoidal compensating window. The effectiveness in the accurate determination of DC quantities will be analyzed, and extension later made to the computation of other harmonic values. Continuous plots will be created in order to appreciate the effect of the various windows. However it should be noted that the DFT of the windows are actually defined only at the discrete harmonic values.

This method of analyzing the values of $S_{win}W(\omega_k)$ in order to determine the errors in DC computation due to the contributions of the various harmonics, agrees with the results obtained in [9] and [10].

2.3.1. Classical windows

The classical windows which will be treated are the rectangular, the Hamming, Hanning, Blackman and Fast decaying 3-term windows.

2.3.1.1 Rectangular Window

This window is effectively what is used when the average of a set of samples are obtained by summing them and dividing by the number of samples.

The rectangular window is defined as:

$$w(i) = \begin{cases} 1, & 0 \le i \le N-1 \\ 0, & otherwise \end{cases} \qquad (2.3.3)$$

with $S_{win} = \frac{1}{N}$,

The DTFT of the window scaled by S_{win} is:

$$S_{win}W_{rect}(\omega) = \frac{1}{N}\sum_{i=0}^{N-1} e^{-ji\omega}$$

$$= \frac{e^{\frac{j\omega(N-1)}{2}}}{N} \sum_{i=-(N-1)/2}^{(N-1)/2} e^{-j\omega i}$$

$$S_{win}W_{rect}(\omega) = \frac{1}{N}\frac{\sin\frac{N\omega}{2}}{\sin\frac{\omega}{2}} e^{-\frac{j(N-1)\omega}{2}} \qquad (2.3.4)$$

$$S_{win}|W_{rect}(\omega)| = \left| \frac{1}{N} \frac{\sin \frac{N\omega}{2}}{\sin \frac{\omega}{2}} \right| \tag{2.3.5}$$

At the harmonic k:

$\omega=\omega_k$

Hence substituting for this value from Equation 2.2.3:

$$S_{win}|W_{rect}(k\phi)| = \left| \frac{1}{N} \frac{\sin \frac{Nk\phi}{2}}{\sin \frac{k\phi}{2}} \right| \tag{2.3.6}$$

The example plot in figure 2.1 indicates the scaled DTFT of the rectangular window for N=60 and Δ=0.9.

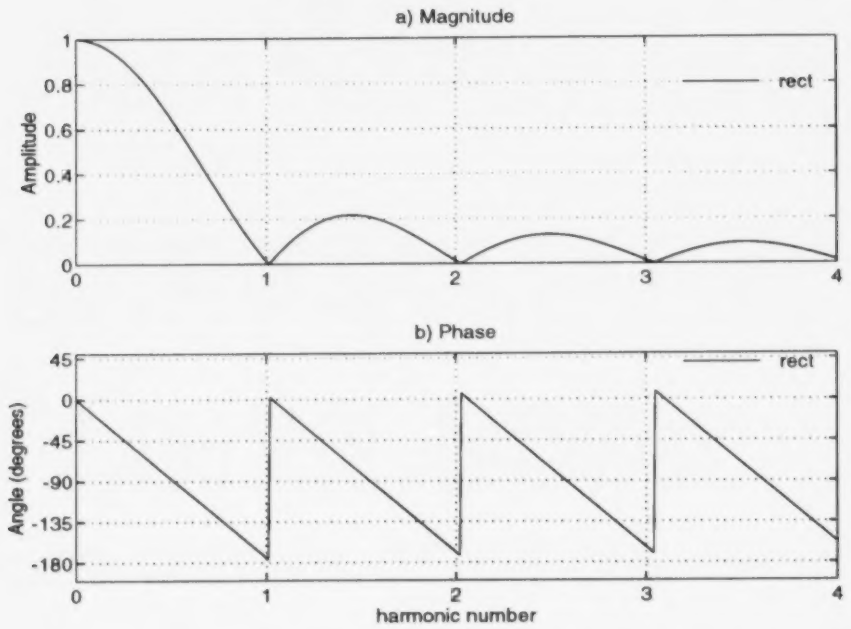

Figure 2.1 The scaled DTFT Plot for the Rectangular Window (N=60, Δ=0.9)

Since

$$(N+\Delta)\phi = 2\pi$$

$$\Rightarrow \frac{Nk\phi}{2} = \pi k - \frac{\Delta k\phi}{2}$$

Equation 2.3.6 can be further expressed as:

$$S_{win}|W_{rect}(k\phi)| = \left|\frac{1}{N}\frac{\sin\frac{Nk\phi}{2}}{\sin\frac{k\phi}{2}}\right|$$
$$= \left|\frac{-\cos(\pi k).\sin\frac{\Delta k\phi}{2}}{N\sin\frac{k\phi}{2}}\right|$$
$$= \left|\frac{\sin\frac{\Delta k\phi}{2}}{N\sin\frac{k\phi}{2}}\right| \qquad (2.3.7)$$

2.3.1.2 Sum of Cosines Windows[14]

This class of windows includes the commonly used Hanning, Hamming and Blackman windows. The *ith* sample value of these windows can be expressed as follows:

$$w(i) = \sum_{p=0}^{P}(-1)^p a_p \cos\frac{2p\pi i}{N}$$
$$= \sum_{p=0}^{P}(-1)^p \frac{a_p}{2}\left(e^{j\frac{2p\pi i}{N}} + e^{-j\frac{2p\pi i}{N}}\right) \qquad (2.3.8)$$

subject to the constraint:

$$\sum_{p=0}^{P} a_p = 1$$

The maximum value of p (P) for the window will be termed the order of the window. Thus a Hanning window is a 1st order sum of cosines window.

The resulting DTFT for this class of windows scaled by S_{win} is:

$$
\begin{aligned}
S_{win}W_{scos}(\omega) &= S_{win}\sum_{i=0}^{N-1}\left[\sum_{p=0}^{P}(-1)^p\frac{a_p}{2}\left(e^{j\frac{2p\pi i}{N}}+e^{-j\frac{2p\pi i}{N}}\right)\right]e^{-ji\omega} \\
&= S_{win}\sum_{p=0}^{P}\left[\sum_{i=0}^{N-1}(-1)^p\frac{a_p}{2}\left(e^{j\frac{2p\pi i}{N}}+e^{-j\frac{2p\pi i}{N}}\right)\right]e^{-ji\omega} \\
&= S_{win}\sum_{p=0}^{P}(-1)^p\frac{Na_p}{2}[W_{rect}(\omega-\frac{2p\pi}{N})+W_{rect}(\omega+\frac{2p\pi}{N})] \\
&= S_{win}\sum_{p=0}^{P}(-1)^p\frac{a_p}{2}\frac{\sin(\frac{N\omega}{2}-p\pi)}{\sin(\frac{\omega}{2}-\frac{p\pi}{N})}\cdot e^{-j(N-1)(\frac{\omega}{2}-\frac{p\pi}{N})}+ \\
&\quad S_{win}\sum_{p=0}^{P}(-1)^p\frac{a_p}{2}\frac{\sin(\frac{N\omega}{2}+p\pi)}{\sin(\frac{\omega}{2}+\frac{p\pi}{N})}\cdot e^{-j(N-1)(\frac{\omega}{2}+\frac{p\pi}{N})}
\end{aligned}
\tag{2.3.9}
$$

At the harmonic k:

$$\omega=\omega_k$$

Hence substituting for this value from equation 2.2.3:

$$
\begin{aligned}
S_{wn}W_{scos}(k\phi) &= S_{win}\sum_{p=0}^{P}(-1)^p\frac{a_p}{2}[\frac{\sin(\frac{Nk\phi}{2}-p\pi)}{\sin(\frac{k\phi}{2}-\frac{p\pi}{N})}e^{-j(N-1)(\frac{k\phi}{2}-\frac{p\pi}{N})}]+ \\
&\quad S_{win}\sum_{p=0}^{P}(-1)^p\frac{a_p}{2}[\frac{\sin(\frac{Nk\phi}{2}+p\pi)}{\sin(\frac{k\phi}{2}+\frac{p\pi}{N})}e^{-j(N-1)(\frac{k\phi}{2}+\frac{p\pi}{N})}]
\end{aligned}
\tag{2.3.10}
$$

$$
\begin{aligned}
S_{wn}W_{scos}(k\phi) &= S_{win}\sum_{p=0}^{P}(-1)^p\frac{a_p}{2}[\frac{\sin(\frac{Nk\pi}{N+\Delta}-p\pi)}{\sin(\frac{k\pi}{N+\Delta}-\frac{p\pi}{N})}e^{-j(N-1)(\frac{k\pi}{N+\Delta}-\frac{p\pi}{N})}]+ \\
&\quad S_{win}\sum_{p=0}^{P}(-1)^p\frac{a_p}{2}[\frac{\sin(\frac{Nk\pi}{N+\Delta}+p\pi)}{\sin(\frac{k\pi}{N+\Delta}+\frac{p\pi}{N})}e^{-j(N-1)(\frac{k\pi}{N+\Delta}+\frac{p\pi}{N})}]
\end{aligned}
\tag{2.3.11}
$$

$$S_{win}W_{s\cos}(k\phi) = S_{win}\sum_{p=0}^{P}(-1)^p\frac{a_p}{2}[\frac{\sin(\frac{Nk}{N+\Delta}-p)\pi}{\sin(\frac{k}{N+\Delta}-\frac{p}{N})\pi}e^{-j(N-1)\pi(\frac{k}{N+\Delta}-\frac{p}{N})}]+$$

$$S_{win}\sum_{p=0}^{P}(-1)^p\frac{a_p}{2}[\frac{\sin(\frac{Nk}{N+\Delta}+p)\pi}{\sin(\frac{k}{N+\Delta}+\frac{p}{N})\pi}e^{-j(N-1)\pi(\frac{k}{N+\Delta}+\frac{p}{N})}] \qquad (2.3.12)$$

where S_{win}, the scaling factor, is dependent on the window type and is chosen such that when $\omega = 0$, $W = 1$.

TABLE 2.1 Some commonly employed Sum of Cosines Windows

WINDOW	a_0	a_1	a_2	a_3	a_4	$N.S_{win}$
Hanning	0.5	-0.5				1/0.5
Hamming	0.54	-0.46				1/0.54
Blackman	0.42	-0.5	0.08			1/0.42
FD3	0.26526	-0.5	0.23474			1/0.26526
FD4	0.21706	-0.42103	0.28294	-0.07897		1/0.21706
FD5	0.1881	-0.36923	0.28702	-0.13077	0.02488	1/0.1881
MS3	0.28235	-0.52105	0.19659			1/0.28235
MS4	0.241906	-0.460841	0.255381	-0.041872		1/0.241906
MS5	0.209671	-0.407331	0.281225	-0.092669	0.0091036	1/0.209671

FD3 - fast-decaying 3-term flat-top window
FD4 - fast-decaying 4-term flat-top window
FD5 - fast-decaying 5-term flat-top window
MS3 - Minimum sidelobe 3-term flat-top window
MS4 - Minimum sidelobe 4-term flat-top window
MS5 - Minimum sidelobe 5-term flat-top window

The example plot in Figure 2.2 indicates the scaled DTFT of the Hanning and Hamming windows for N=60 and Δ=0.9. The example plot in Figure 2.3 indicates the scaled DTFT of the Blackman and Fast decaying 3-term flat-top windows for N=60 and Δ=0.9.

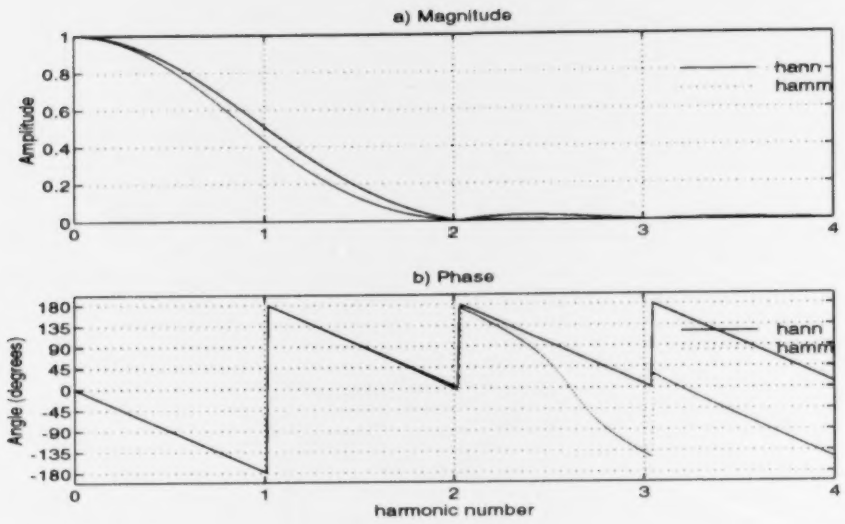

Figure 2.2 Scaled DTFT plots for the Hanning and Hamming Windows (N=60, Δ =0.9)

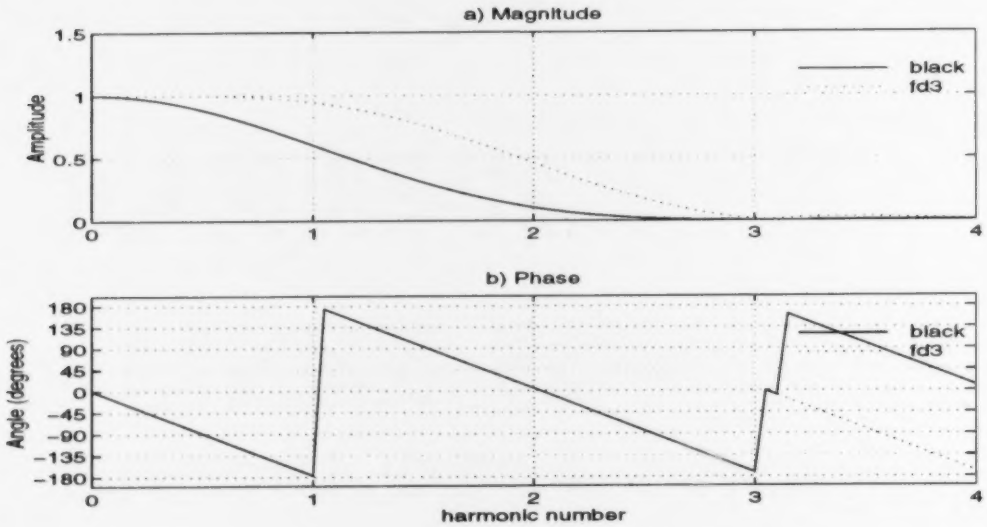

Figure 2.3 Scaled DTFT plots for the Blackman and the Fast Decaying 3-term Flat-top windows (N=60, Δ=0.9)

2.3.2. Compensating windows

Compensating windows utilize the value of Δ in the windowing function. The window employed in this thesis (the TCW) will be discussed in this section.

2.3.2.1 Trapezoidal Compensating Window (TCW-Proposed Algorithm)

Of the composite Newton-Cotes[9] formulae for the evaluation of the integral of periodic functions, the composite mid-point or composite trapezoidal rule result in the greatest rate of error reduction as N increases [9]. For a given set of data points as obtained in the sampling process in the digital instrument, the mid-point rule is not appropriate for integral evaluation, since it involves the determination of the unknown function values at the mid-points of the sampled values before the summation process can be used. The composite trapezoidal rule is thus the prime candidate for the computation. When the period of the signal is an integral multiple of the sampling interval, the composite trapezoidal rule reduces to the sum of the samples, with indices from 0 to N-1 (where the 0th index refers to the start of the signal, and the Nth index will correspond to the end of the period or the 0th index for the next cycle). This idea was used by Turgel [17] in his synchronously sampled implementation of a digital wattmeter. Mainly because of it's ease of computation, that same idea was extended to wattmeters where the sampling was not synchronized to the input waveform.

The use of the trapezoidal formula is employed by incorporating the actual signal period measured as the number of sampling intervals N, and the fraction of a sampling interval Δ. The latter-mentioned formula gives rise to the trapezoidal compensating window. The fraction Δ can be easily measured in a system hardware setup or estimated from the sample values.

For a signal with period $(N+\Delta)T_S$, the trapezoidal compensating window indices are defined as:

$$w(i)=\begin{Bmatrix} 0.5, & i=0 \\ 1, & 1\le i\le N-1 \\ 0.5+\dfrac{\Delta}{2}, & i=N \\ \dfrac{\Delta}{2}, & i=N+\Delta \end{Bmatrix} \qquad (2.3.13)$$

Since $(N+\Delta)\phi = 2\pi$,
it follows that
$w(N+\Delta) = w(0)$
and
$x(N+\Delta) = x(0)$

Let the multiplier in the determination of the DTFT of a windowed signal be expressed as $E(i) = e^{-jki\phi}$

Hence determination of the DTFT of a signal x(i) using the TCW results in:

$$DTFT[y(i)] = (0.5w(0)E(0) + \sum_{i=0}^{N-1} w(i)x(i)E(i) + (0.5+\frac{\Delta}{2})w(N)x(N)E(N) + \frac{\Delta}{2}w(0)x(0)E(0)$$

$$= (0.5+\frac{\Delta}{2})w(0)x(0)E(0) + \sum_{i=0}^{N-1} w(i)x(i)E(i) + (0.5+\frac{\Delta}{2})w(N)x(N)E(N)$$

Thus, an alternate expression for this window is:

$$w(i) = \begin{Bmatrix} 0.5+\frac{\Delta}{2}, & i=0 \\ 1, & 1 \le i \le N-1 \\ 0.5+\frac{\Delta}{2}, & i=N \end{Bmatrix} \qquad (2.3.14)$$

Now $S_{win} = \frac{1}{N+\Delta}$,

hence the resulting DTFT scaled by S_{win} is:

$$S_{win}W_{tcw}(k\phi) = \frac{1}{N+\Delta}[0.5e^{-j0k\phi} + \sum_{i=1}^{N-1} e^{-jik\phi} + 0.5e^{-jkN\phi} + \frac{\Delta}{2}(e^{-j0k\phi} + e^{-jkN\phi})] \qquad (2.3.15)$$

$$S_{win}W_{tcw}(k\phi) = \frac{1}{N+\Delta}[\sum_{i=0}^{N-1} e^{-jik\phi} + \frac{1}{2}(e^{-jNk\phi} - e^{-j0k\phi}) + \frac{\Delta}{2}(e^{-jNk\phi} + e^{-j0k\phi})]$$

$$S_{win}W_{tcw}(k\phi) = \frac{1}{N+\Delta}\left[\frac{\sin\frac{Nk\phi}{2}}{\sin\frac{k\phi}{2}} e^{\frac{-jk\phi(N-1)}{2}} - je^{\frac{-jNk\phi}{2}}\sin\frac{Nk\phi}{2} + \Delta e^{\frac{-jNk\phi}{2}}\cos\frac{Nk\phi}{2}\right] \qquad (2.3.16)$$

$$S_{win}W_{tcw}(k\phi) = \frac{1}{N+\Delta}\left[\frac{\sin\frac{Nk\phi}{2}}{\sin\frac{k\phi}{2}}\cos\frac{k\phi}{2} + \Delta\cos\frac{Nk\phi}{2}\right] \cdot e^{\frac{-jkN\phi}{2}}$$

The magnitude of the resulting DTFT scaled by S_{win} is:

$$S_{win}\left|W_{tcw}(k\phi)\right| = \frac{1}{N+\Delta}\left|\left[\frac{\sin\frac{Nk\phi}{2}}{\sin\frac{k\phi}{2}}\cos\frac{k\phi}{2}+\Delta\cos\frac{Nk\phi}{2}\right]\right|$$

$$= \frac{1}{N+\Delta}\left|\left[\frac{-\sin\frac{k\pi\Delta}{N+\Delta}.\cos k\pi}{\sin\frac{k\pi}{N+\Delta}}\cos\frac{k\pi}{N+\Delta}+\Delta\cos k\pi.\cos\frac{k\pi\Delta}{N+\Delta}\right]\right|$$

$$= \left|\frac{\cos k\pi}{N+\Delta}\right|\left|\left[\frac{-\sin\frac{k\pi\Delta}{N+\Delta}}{\sin\frac{k\pi}{N+\Delta}}\cos\frac{k\pi}{N+\Delta}+\Delta\cos\frac{k\pi\Delta}{N+\Delta}\right]\right|$$

(2.3.17)

The example plot in Figure 2.4 indicates the DTFT of the Trapezoidal compensating window for N=60 and Δ=0.9 indicating the very small amplitudes at the harmonic values unlike the rectangular window applied to an asynchronously sampled signal. This results in minimal leakage being produced by the TCW. The spikes in the phase plot in figure 2.4 occur when the amplitude portion of the DTFT,

$$\frac{\sin\frac{Nk\phi}{2}}{\sin\frac{k\phi}{2}}\cos\frac{k\phi}{2}+\Delta\cos\frac{Nk\phi}{2}$$

changes sign while the phase $\frac{-kN\phi}{2}$ still has the same sign for the angle.

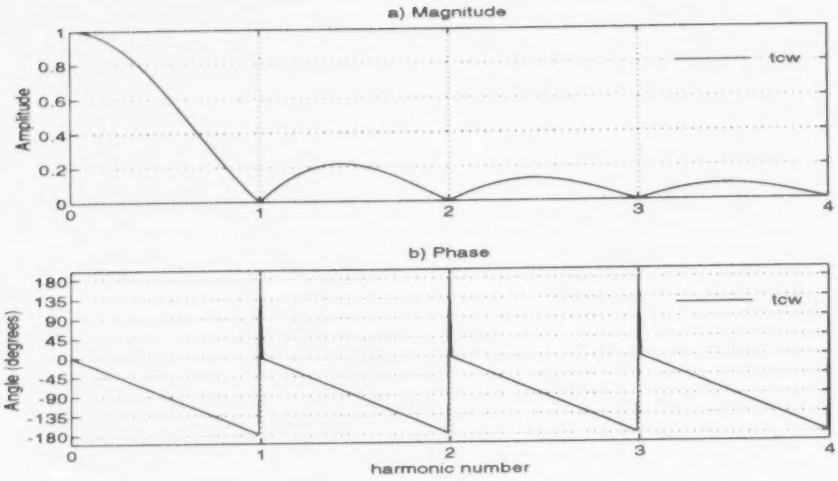

Figure 2.4 DTFT plot of the Trapezoidal Compensating Window (N=60, Δ=0.9)

When Δ is constrained to the range (-0.5,0.5] and N incremented by one when Δ > 0.5, a reduction in the window amplitude for values of Δ > 0.5 can be achieved. Thus an adjusted value of Δ will be used, whenever the TCW is employed. An example used to explain this concept is shown in Figure 2.5

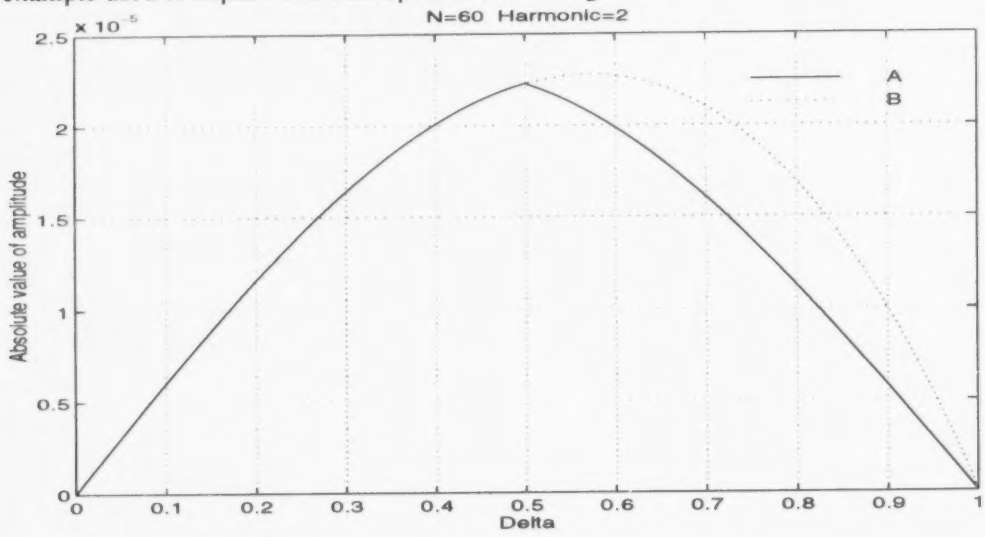

Figure 2.5 DTFT Magnitude Plots of the Trapezoidal Compensating Windows for A) Δ adjusted, B) Δ not adjusted(N=60, k=2)

In plot (A) in Figure 2.5, values of $\Delta > 0.5$ actually correspond to the negative values Δ-1, and the adjusted N value, 61. This was done in order to indicate the effect of adjusting Δ.

Since the first zero crossing of the Fourier transform of the TCW is close to the first harmonic,(Figure 2.4) and in a synchronized case this window is identical to the rectangular window, long-range and not medium-range effects will be the prime error contributions. In addition, it implies that this window can be used in situations where only a single period of the input signal is available, or desirable for computation purposes. This thus forms a good basis for a window for the determination of the harmonic components of a signal as will be demonstrated by examples in the next section.

2.4 Summary of the Various Windowing Schemes

As noted in Section 2.3, the choice of a window which minimizes the long and medium-term leakage errors will improve the measurement accuracy in the determination of the average value of the signal.

The ideal or perfect window should have a Fourier transform with no side-lobes, a very narrow main lobe and a constant zero-frequency value of 1. As known, such a window is non-causal and has infinite width.

In the determination of the average (DC value) of an asynchronously sampled signal, the contribution of the harmonic components of the signal to the average value, can be easily determined by evaluating the window DTFT components at the harmonic frequency.

Two main comparison schemes will be employed for the various windows discussed. The first set of plots in section 2.4.1 will be based on a fixed value of N and Δ and the DTFT values at the various harmonic values will be evaluated. The second set of plots in Section 2.5.2 will be based on a fixed value of N and harmonic number (k) but varying Δ.

2.4.1 Window DTFT comparisons (N=60 and Δ=0.9 and k varying)

The magnitude and phase plots of the transforms of some of the windows evaluated previously will be provided. The plots are provided for a signal with period $60.9*T_S$ (i.e. N = 60 and Δ = 0.9). T_S is the fundamental period of the signal under consideration. The TCW as stated is plotted using N = 61 and Δ = -0.1. The magnitude values for the DC value and the first 7 harmonics are tabulated in Table 2.2. In Table 2.3, the phase values for the DC value and the first 7 harmonics are tabulated.

TABLE 2.2 The DC and first 7 harmonic DFT Magnitude values of some Windows for N=60 and Δ=0.9

Harm.	Rect	TCW	Hanning	Hamming	Blackman	FD3
0	1	1	1	1	1	1
1	0.015001	1.4422e-06	0.51109	0.4376	0.60467	0.94586
2	0.015005	5.772e-06	0.005196	2.2269e-03	0.10343	0.4616
3	0.015011	1.2998e-05	0.0019327	6.4892e-04	1.0451e-04	0.007532
4	0.01502	2.3137e-05	1.0263e-03	1.3812e-03	2.3637e-04	2.6436e-03
5	0.015032	3.6208e-05	6.3874e-04	1.7065e-03	2.0169e-04	1.3918e-03
6	0.015046	5.2241e-05	4.3595e-04	1.8787e-03	1.5461e-04	8.7112e-04
7	0.015063	7.127e-05	3.1614e-04	1.9818e-03	1.1888e-04	6.0031e-04

The above results show the effect of the wide main lobes of the Hanning, Hamming, Blackman and fast decaying 3-term flat-top windows in the comparatively large window DTFT magnitude values at the first harmonic position.

TABLE 2.3 The DC and first 7 harmonic DFT Phase values in degrees of some Windows for N=60 and Δ=0.9

Harm	Rect	TCW	Hanning	Hamming	Blackman	FD3
0	0	0	0	0	0	0
1	-174.38	179.7	-177.34	-177.32	-177.34	-177.34
2	-168.77	179.41	5.3202	-0.58064	5.3202	5.3202
3	-163.15	179.11	7.9803	-140.13	-172.02	-172.02
4	-157.54	178.82	10.64	-150.09	10.64	-169.36
5	-151.92	178.52	13.3	-147.26	13.3	-166.7
6	-146.31	178.23	15.961	-142.85	15.961	-164.04
7	-140.69	177.93	18.621	-137.94	18.621	-161.38

It must be noted that values close to ±180 degrees translate to a phase reversal in the phasors. Hence the TCW values are actually small phase angle deviations. In general one seeks small angle deviations from 0 or ±180 degrees with an amplitude value of 1 at the desired harmonic, and minimal amplitude and phase contribution at the other harmonics. The above results show clearly the minimal phase error contributions of the TCW.

The plots indicate the effect at harmonic components 4, 5, 6 and 7, for a window centered about the DC value (harmonic number 0). Figure 2.6 indicates the reduction in amplitude value at the harmonic frequencies provided by the TCW as well as minimal phase contributions, compared to the rectangular window. This has the effect of minimizing the various leakage effects previously described. Figure 2.7 indicates a plot of the DTFT of the Hanning and Hamming windows for N=60 and Δ

=0.9. Figure 2.8 indicates a plot of the DTFT of the Blackman and the fast decaying 3-term flat-top windows for N=60 and Δ=0.9.

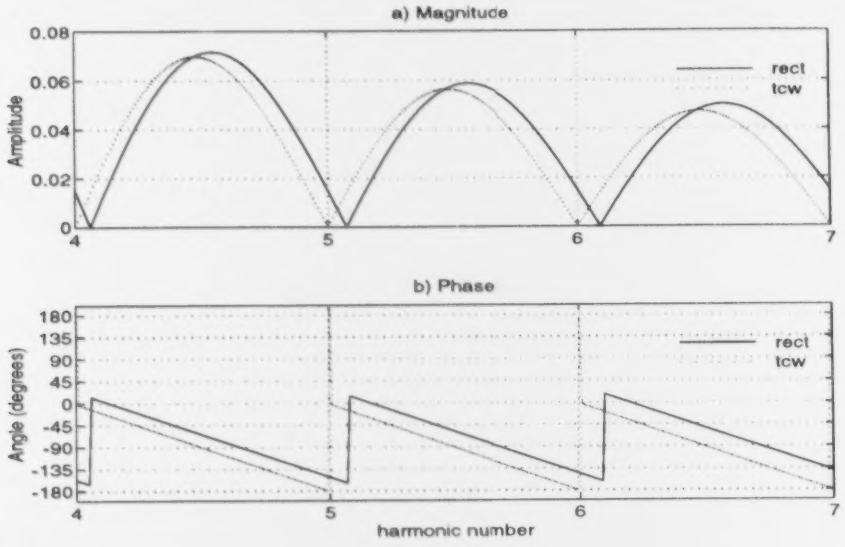

Figure 2.6 DTFT plots for the Rectangular and Trapezoidal Compensating Windows (N=60, Δ=0.9)

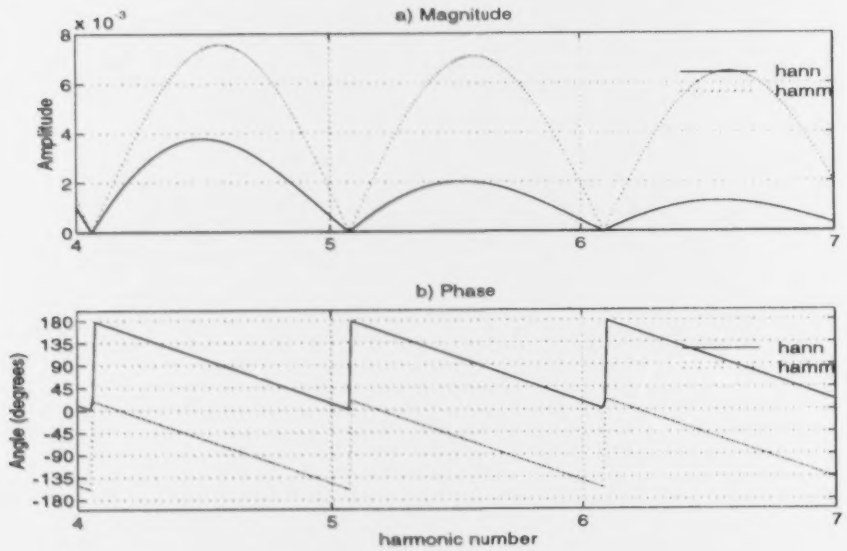

Figure 2.7 DTFT plots for the Hanning and Hamming Windows (N=60, Δ=0.9)

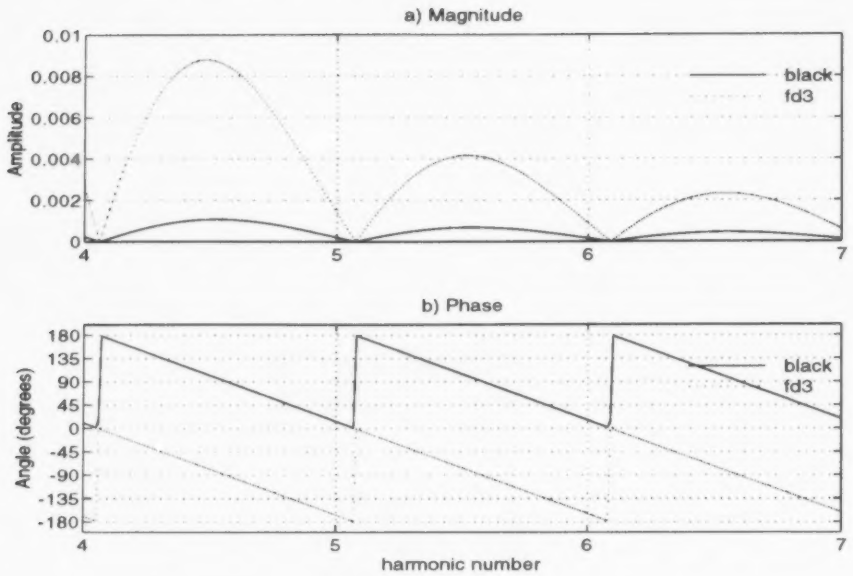

Figure 2.8 DTFT plots for the Blackman and the Fast Decaying 3-term Windows (N=60, Δ=0.9)

2.4.2 Window DTFT comparisons (N=60 and k=2, Δ varying)

The error in the measurement of the DC component due to the second harmonic component of a signal is analyzed in this section. The error can be analyzed by considering the amplitude and phase of the DTFT of the applied window at the second harmonic. The amplitude and phase values of the DTFT of the windows discussed are evaluated at the 2nd harmonic for a signal having 60 samples (N=60) and Δ in the range [0,1). Δ is incremented in steps of 0.01 and in each case the amplitude and phase of the DTFT of the window at the second harmonic is evaluated. This results in the various waveforms of Figures 2.9-2.12.

The magnitude and phase values for various values of Δ are tabulated in Table 2.3 and 2.4 respectively. Table values having a magnitude less than 1.0e-16 translate to zero. This conforms with theoretical values for the rectangular, Hanning and Hamming windows as well as the TCW when Δ=0. The reduction in the magnitude values for the TCW as well as the minimal phase deviation can be noted.

TABLE 2.4 The DTFT Magnitude values of some Windows for N=60 and k=2

Δ	Rect	TCW	Hanning	Hamming	Blackman	FD3
0	3.9052e-17	3.8838e-17	3.5786e-20	5.8158e-18	NaN	NaN
0.1	0.0016697	6.0057e-006	0.00055802	0.00023079	0.096139	0.44462
0.2	0.0033392	0.000011589	0.0011209	0.00046574	0.097042	0.44677
0.3	0.0050082	0.000016395	0.0016887	0.00070485	0.097948	0.4489
0.4	0.0066768	0.000020077	0.0022614	0.00094813	0.098856	0.45103
0.5	0.0083446	0.000022295	0.0028388	0.0011956	0.099766	0.45316
0.6	0.010011	0.000019879	0.003421	0.0014472	0.10068	0.45528
0.7	0.011677	0.000016073	0.004008	0.0017029	0.10159	0.45739
0.8	0.013342	0.000011249	0.0045997	0.0019628	0.10251	0.4595
0.9	0.015005	5.772e-006	0.005196	0.0022269	0.10343	0.4616
1	0.016667	3.8842e-017	0.0057971	0.0024951	0.10435	0.46369

TABLE 2.5 The DTFT Phase values in degrees of some Windows for N=60 and k=2

Δ	Rect	TCW	Hanning	Hamming	Blackman	FD3
0	-174	-180	-180	-174.03	0	0
0.1	-173.41	0.599	0.599	-5.8229	0.599	0.599
0.2	-172.82	1.196	1.196	-5.1573	1.196	1.196
0.3	-172.24	1.791	1.791	-4.4947	1.791	1.791
0.4	-171.66	2.3841	2.3841	-3.835	2.3841	2.3841
0.5	-171.07	2.9752	2.9752	-3.1784	2.9752	2.9752
0.6	-170.5	177.62	3.5644	-2.5246	3.5644	3.5644
0.7	-169.92	178.22	4.1516	-1.8738	4.1516	4.1516
0.8	-169.34	178.82	4.7368	-1.2258	4.7368	4.7368
0.9	-168.77	179.41	5.3202	-0.58064	5.3202	5.3202
1	-168.2	-180	5.9016	0.061698	5.9016	5.9016

Figure 2.9 indicates a plot of the DTFT of the rectangular window at the second harmonic (k=2) for N=60. Figure 2.10 indicates plots of the DTFT of the Hanning and Hamming windows at the second harmonic (k=2) for N=60. In Figure 2.11 plots of the DTFT of the Blackman and fast decaying 3-term flat-top windows at the second harmonic (k=2) for N=60 are shown. Figure 2.12 shows the plot of the DTFT of the TCW. For $\Delta > 0.5$, N is incremented by one (N = 61) and Δ is decremented by 1.

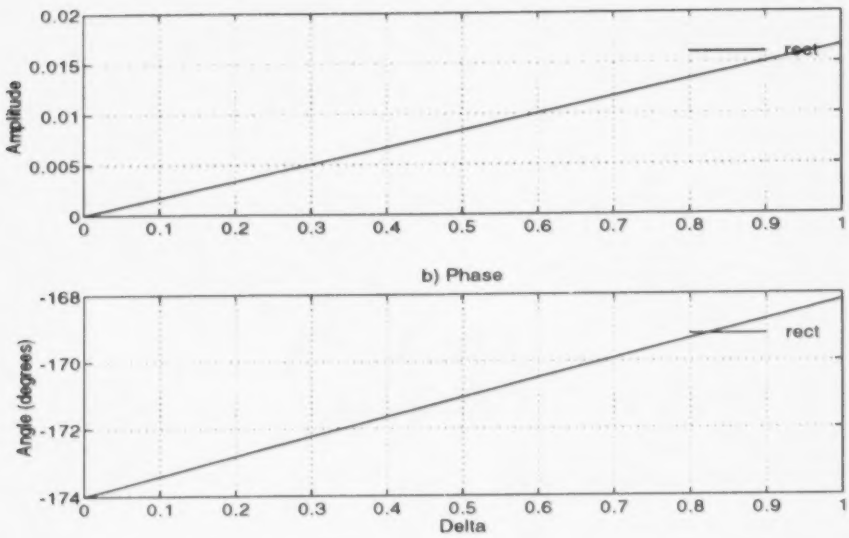

Figure 2.9 DTFT plot for rectangular window for N=60 and Δ=[0,1)

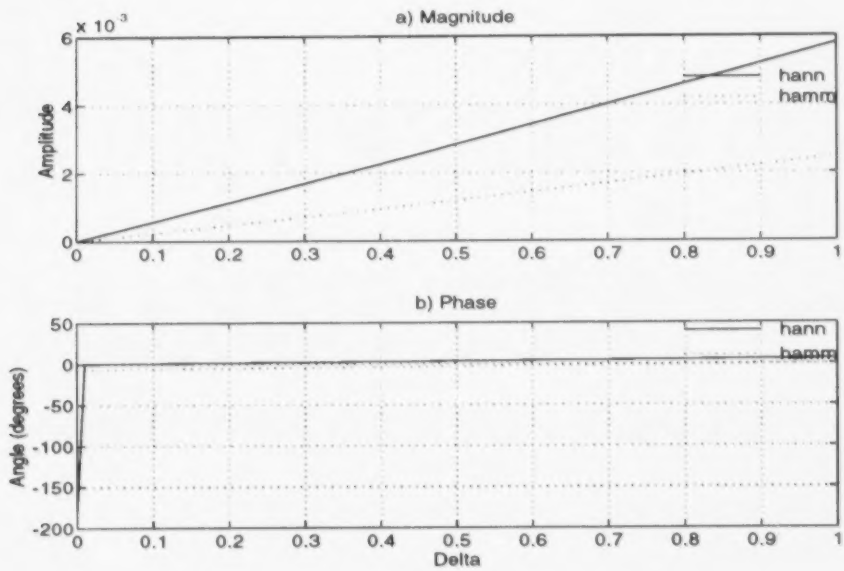

Figure 2.10 DTFT plots for the Hanning and Hamming windows for N=60 and Δ =[0,1)

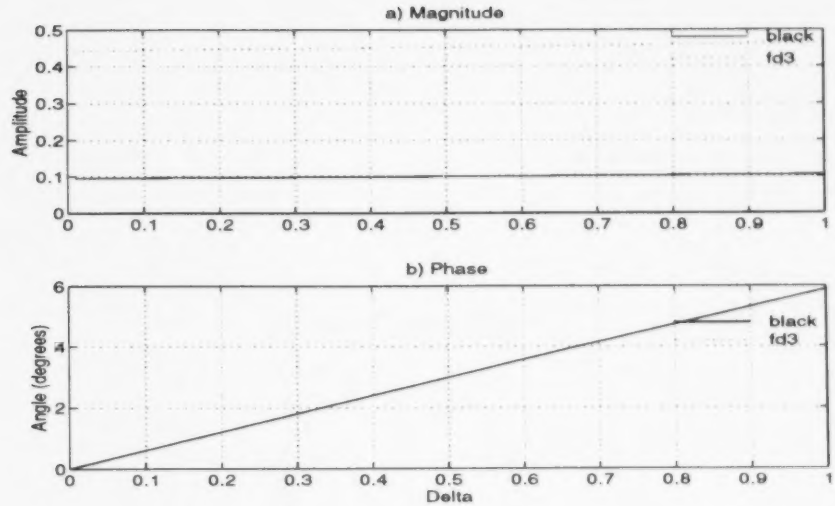

Figure 2.11 DTFT plots for the Blackman and Fast decaying 3-term windows for N=60 and Δ=[0,1)

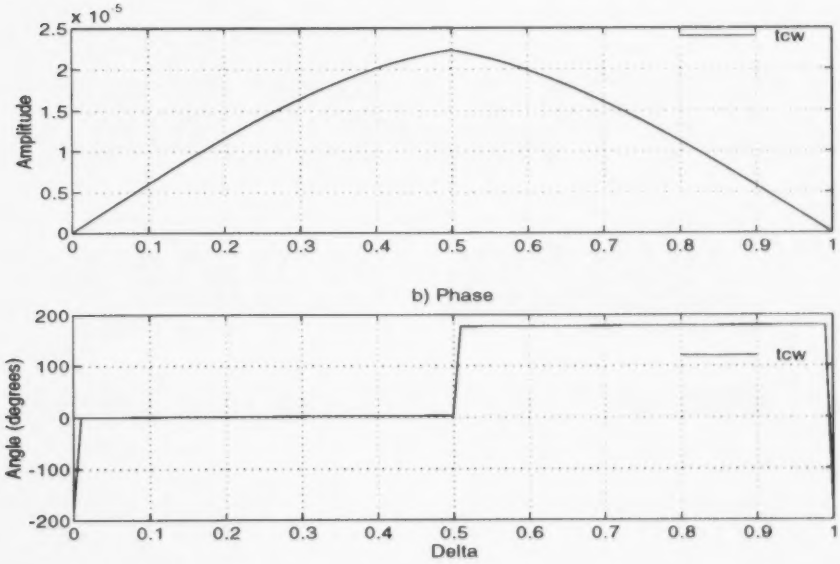

Figure 2.12 DTFT plot for the TCW for N=60 and Δ=[0,1)

2.5 Chapter Summary

The DTFT has been introduced and used to compare the TCW and some classical windows. The measurement accuracy problem has been analyzed by evaluating various windowing implementations for reducing the long and medium range errors. The reduction in long and medium term leakage using the TCW has been illustrated with some examples and thus the use of this window as a prime choice for the measurement of signal average quantities such as electrical power in wattmeters is a good one.

3. HARMONIC MEASUREMENTS

The accurate measurement of the amplitude and phase of signal harmonics using DFT type algorithms entails reducing short-range leakage errors. The signal representation for error analysis purposes introduced previously (see section 2.1) is extended to the general harmonic situation. Two examples of signal waveforms are compared, taking into account the finite instrument bandwidth, using various windowing and DFT algorithms and compared to the TCW algorithm. Error effects introduced by signal quantization and other numerical and hardware effects are analyzed in Chapter 6.

3.1 Harmonic computation and windows

For a continuous signal as expressed by Equation 2.1.3 (restated below) the harmonic coefficients C_k (for $k \neq 0$) can be determined as follows:

$$x_c(t) = C_0 + \sum_{k=1}^{M} C_k \cos\theta_k . \cos(\frac{2\pi k}{T} t) + C_k \sin\theta_k . \sin(\frac{2\pi k}{T} t)$$

$$C_k \cos\theta_k + j C_k \sin\theta_k = 2 \cdot \int_T x_c(t) \cos(\frac{2\pi kt}{T}) + j \cdot x_c(t) \sin(\frac{2\pi kt}{T}) dt$$

$$C_k \angle \theta_k = \frac{2}{T} \cdot \int_T x_c(t) e^{\frac{j2\pi kt}{T}} dt \qquad (3.1.1)$$

Alternatively, using a negative exponential for the complex term representation in equation 3.1.1 results in the expression:

$$C_k \angle -\theta_k = \frac{2}{T} \cdot \int_T x_c(t) e^{\frac{-j2\pi kt}{T}} dt \qquad (3.1.2)$$

If we define a variable X_c such that:

$$X_c(k) = \frac{1}{T} \int_T x_c(t) e^{\frac{-j2\pi kt}{T}} dt$$

$$= \frac{1}{T} \int_T x_c(t) e^{-j\Omega_k} dt \qquad (3.1.3)$$

then using this substitution, Equation 3.1.2 can be expressed as:

$$C_k \angle -\theta_k = 2 \cdot X_c(k) \qquad (3.1.4)$$

X_c is the Fourier transform of $x_c(t)$ scaled by 1/T

For the discrete windowed signal given by the expression

$$y(i) = w(i).x(i)$$
$$= w(i)C_0 + w(i)\sum_{k=1}^{M} C_k \cos(i\omega_k - \theta_k) \qquad (3.1.5)$$

the harmonic components of a discrete signal can be obtained by a procedure analogous to that for continuous signals as shown above. The discrete analogy to the Fourier transform evaluated at the harmonic (or approximate harmonic) frequencies is referred to as the discrete Fourier transform (DFT) of the signal. This is the sampled values of the DTFT at the harmonics (or approximate harmonic) points.

The steps involved in the determination of the Fourier series coefficients using Equation 3.1.4 and the Fourier transform expression in Equation 3.1.3 are:

1) $x_c(t)e^{-j\Omega_l}$ is replaced by a function which is the product of the windowed discrete value at a particular instant and an exponential. The exponent is dependent on either an approximation to the desired harmonic frequency or the desired harmonic frequency. The dependency of the exponent is determined by the DFT algorithm employed and also the sampling scheme used (synchronous or nonsynchronous).
2) The integration (summation) of the function in (1).
3) The averaging of the integral in (2) (division by the approximate fundamental signal period or the actual fundamental period).
4) The application of the appropriate scale factor (S_{win}) to obtain the harmonic components

This leads to the following expression for determining the Fourier series components for a particular harmonic l as.

$$C_l \angle \theta_l = S_{win} \cdot \sum_i y(i) \cdot e^{-j i \omega_{la}}$$
$$= S_{win} \cdot Y(\omega)\Big|_{\omega=\omega_{la}} \qquad (3.1.6)$$

where ω_{la} is the digital frequency which corresponds to the harmonic l in the DFT algorithm used (the approximate or actual frequency depending on the algorithm and sampling scheme).

The summation operator (Σ) sums the product of the derived sample values y(i) and the corresponding exponential term over the range of values of y(i), thus

performing the numerical integration required. S_{win} is the scale factor required for the window employed.

The l_{th} harmonic component of a signal expressed by Equation 3.1.5 can be written as:

$$\begin{aligned} y(i) &= C_l w(i).\cos(i\omega_l - \theta_l) \\ &= \frac{C_l}{2}\left\{e^{-j\theta_l} w(i).e^{ji\omega_l} + e^{j\theta_l} w(i).e^{-ji\omega_l}\right\} \end{aligned} \tag{3.1.7}$$

To determine the relationship between the harmonic component C_l and the corresponding window, the above expression is substituted in the Fourier transform expression.

$$Y(\omega) = \sum_i y(i)\cdot e^{-ji\omega} \tag{3.1.8}$$

which results in:

$$\begin{aligned} Y(\omega) &= \sum_i \frac{C_l}{2}\left\{e^{-j\theta_l} w(i).e^{ji\omega_l}.e^{-ji\omega} + e^{j\theta_l} w(i).e^{-ji\omega_l}.e^{-ji\omega}\right\} \\ &= \frac{C_l}{2}\sum_i\left\{e^{-j\theta_l} w(i).e^{-ji(\omega-\omega_l)} + e^{j\theta_l} w(i).e^{-ji(\omega+\omega_l)}\right\} \\ &= \frac{C_l}{2}.e^{-j\theta_l}\sum_i\left\{w(i).e^{-ji(\omega-\omega_l)}\right\} + \frac{C_l}{2}.e^{j\theta_l}\sum_i\left\{w(i).e^{-ji(\omega+\omega_l)}\right\} \\ &= \frac{C_l}{2}.e^{-j\theta_l}.W(\omega-\omega_l) + \frac{C_l}{2}.e^{j\theta_l}.W(\omega+\omega_l) \end{aligned} \tag{3.1.9}$$

Equation 3.1.9 indicates that the Fourier transform of the windowed signal consists of the Fourier transform of the window replicated at frequencies $\pm\omega_l$. In addition, if the window $W(\omega)$ has non-zero contributions at the frequency desired as well as other harmonic frequencies an error (leakage effects) in the harmonic whose parameters are required will result. Thus the window and the frequency ω_{la} which approximates the actual harmonic frequency ω_l, will have an influence on the accuracy of the harmonic measurements in particular due to short-range leakage effects as seen in the introductory chapter.

Since the DFT of windows have previously been discussed in Chapter 2., there is no need for further analysis. The effect of the choice of the frequency value ω_{la} will be discussed in the next section.

3.2 Basis Vectors in the Harmonic Computation Algorithm

The choice of the frequency value which represents the actual harmonic frequency is seen from Equation 3.1.9 to have an effect on the accuracy of the measurement.

Equation 2.2.3 indicates that, for a particular harmonic component l, the digital frequency ω_{la} coincides with the actual harmonic when :

$$\omega_{la} = \frac{2\pi l}{N+\Delta} = \omega_l \qquad (3.2.1)$$

Thus the basis vectors which are integral multiples of Equation 3.2.1, coincide with the harmonic frequencies of the signal under consideration. Each of the DFT of the windows analyzed have a phase component which is non-zero at off-harmonic frequencies. In particular the phase angle at DC (main lobe of window DFT) is zero. Thus if ω_{la} is chosen as in Equation 3.2.1, the main lobe of the window will coincide exactly with the desired harmonic, thus the phase error due to the main lobe of the window will be non-existent. This implies the elimination of short-range leakage. If, in addition, all the other side-lobes of the window DFT occur at integral multiples of the actual signal frequency, the phase and magnitude errors will be eliminated and a very accurate measurement will result.

Equation 3.2.1 is used for basis vector generation in the DFT based on the TCW. This is termed a modified DFT since the harmonic determination scheme employing the DFT based on classical windows employs a digital frequency for the harmonic l of interest expressed as:

$$\omega_{la} = \frac{2\pi l}{N} \qquad (3.2.2)$$

In addition, Δ is constrained to the range [-0.5,0.5] and N adjusted appropriately as in the DC measurement case. The TCW and the modified DFT algorithm employed results in a greatly reduced contribution of leakage effects to the measurement error. Thus a high accuracy magnitude and phase measurements will be expected even when only a single period of the signal is available for analysis.

3.3 Plots of the DFT of some Windows in Harmonic Computations

Some magnitude and phase plots are provided to illustrate the effects of the use of the DFT and modified DFT on the error contribution to the computed harmonic. It should be expected that the major error would be contributed around the main lobe of the window, especially if there is an appreciable magnitude reduction and

appreciable non-zero phase contribution. The plots utilize the values of N and Δ used in the previous plots, (N=60, Δ=0.9) for consistency. The classical windows have their peak at a 'harmonic' value of 2.03. The window based on the TCW and modified DFT peaks at the desired 2nd harmonic

Figure 3.1 shows the expanded DFT plots of the rectangular window. The phase error at the second harmonic frequency is observed to be about 5 degrees.

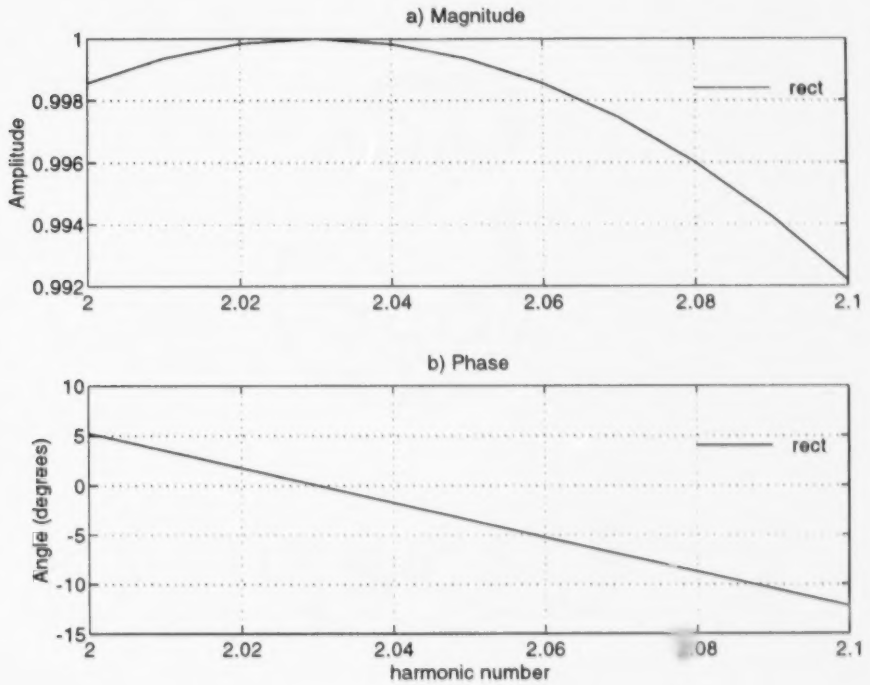

Figure 3.1 Expanded DFT Plots for the Rectangular Window in a 2nd harmonic computation (N=60, Δ=0.9)

Figure 3.2 shows the expanded DFT plots of the Hanning and Hamming windows. The phase error at the second harmonic frequency is about 5 degrees. In Figure 3.3 the expanded DFT plots of the Blackman and the fast decaying 3-term flat-top windows is shown. The phase error at the second harmonic frequency is also appromately 5 degrees. Figure 3.4 shows the expanded DFT plots of the TCW using the modified DFT. A zero degree phase error is observed at the second harmonic frequency. This is an improvement over the previous windowing techniques and DFT algorithm.

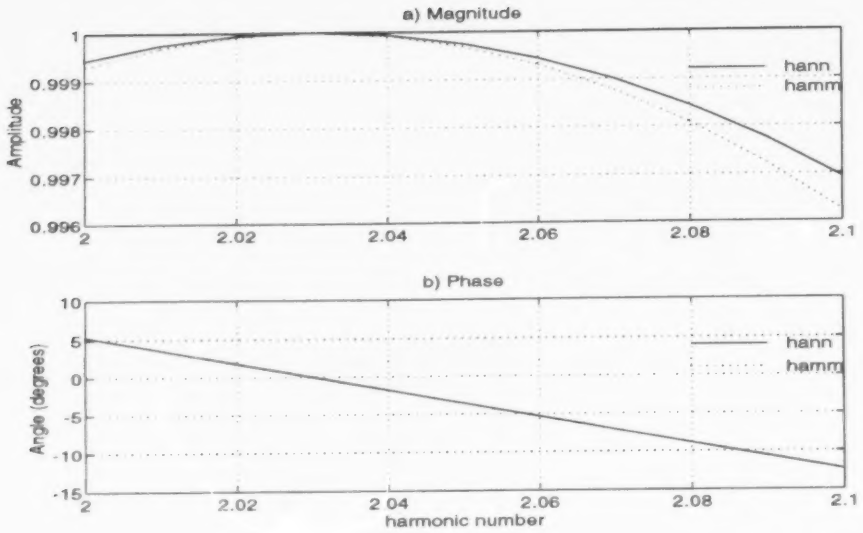

Figure 3.2 Expanded DFT Plots for the Hanning and Hamming Windows in a 2nd harmonic computation (N=60, Δ=0.9)

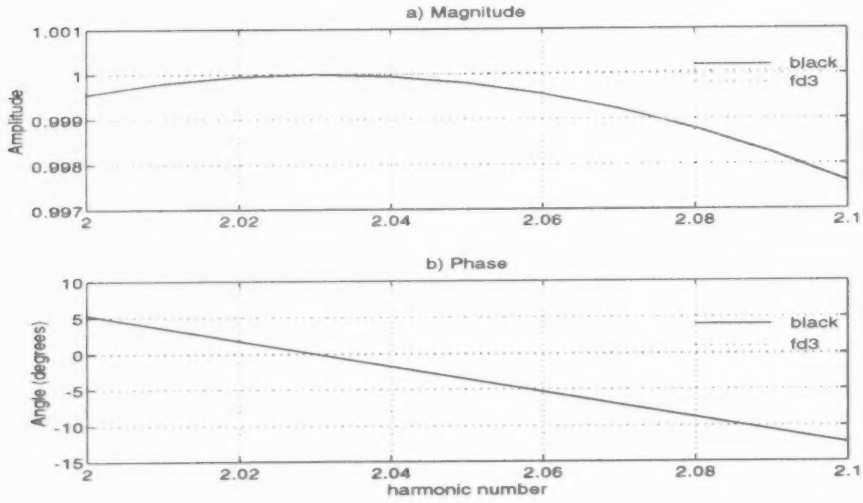

Figure 3.3 Expanded DFT Plots for the Blackman and the Fast Decaying 3-term Windows in a 2nd harmonic computation (N=60, Δ=0.9)

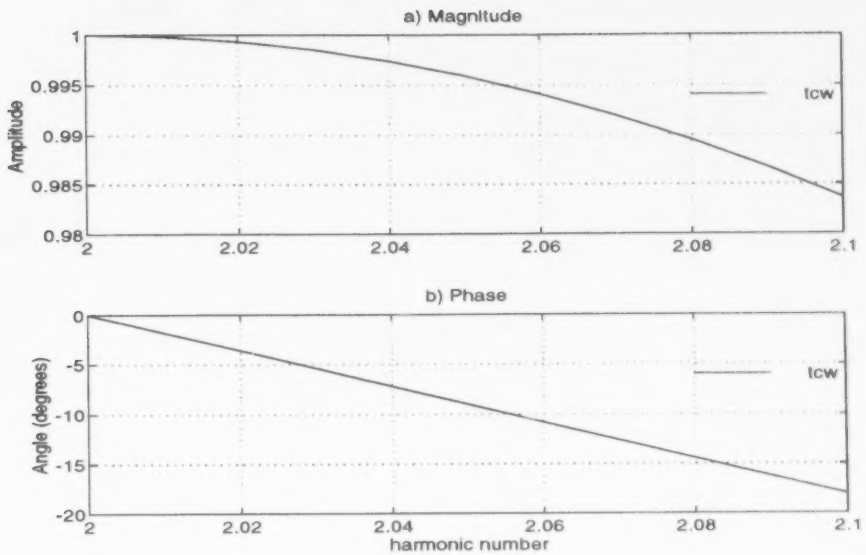

Figure 3.4 Expanded Plots for the TCW employing a modified DFT in a 2nd harmonic computation (N=60, Δ=0.9)

3.4 Experimental Results

The TCW will be applied to a two signals and compared with some classical windows applied to the same signals. A signal simulating long and short term leakage effects will be employed, in addition to a PWM signal.

3.4.1 A Waveform Exhibiting Long and Short-Term Leakage

The waveform employed is described by the following equation [4]

$$\sum_{j=1}^{10} A_j . \sin\{2\pi fjt + \frac{\pi}{10} j\} \qquad (3.4.1)$$

where f = 50.005 Hz

The amplitude values A_j are indicated in Table 3.1.

TABLE 3.1 The Amplitude values for Equation 3.4.1

j	1	2	3	4	5	6	7	8	9	10
A_j	6V	1V	0.5V	1.5V	0.5V	1V	0.5V	0.5V	1.5V	0.5V

Each harmonic amplitude was chosen in such a way that the 2nd harmonic measurement is affected by a predominant long-range leakage error and that the 9th harmonic measurement is affected by a predominant short-range leakage error [4]. The signal was acquired over 3 periods and comparison was based on 749 and 750 (this being the number of samples on either side of 3 cycles of the signal under consideration).

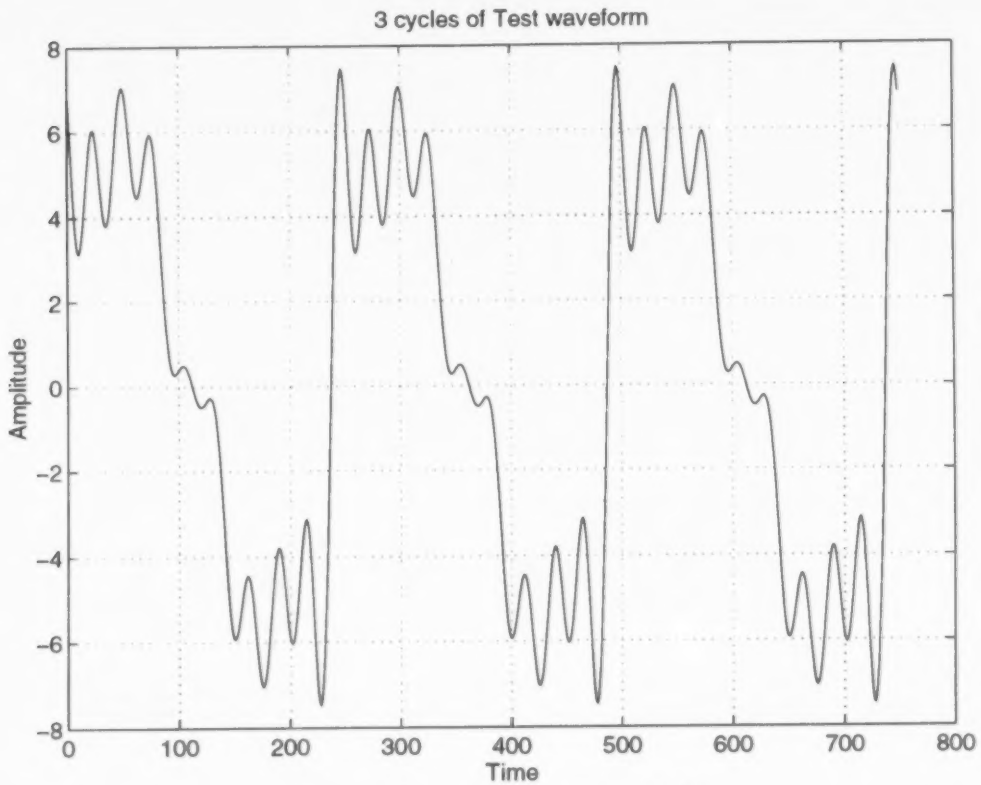

Figure 3.5 Plot of Equation 3.4.1

The DFT was applied to the signal in Equation 3.4.1, using various windows. In addition, the TCW and the modified DFT algorithm were applied to the signal. The maximum harmonic order of 10 implies a maximum signal frequency of 500.05Hz. The sampling frequency was 12.5kHz. this was chosen equal to that in Reference [4] to make comparisions easier. The percentage errors for the magnitude and phase results are tabulated in Tables 3.2 and 3.3 respectively.

TABLE 3.2 Percentage errors in Magnitude determination

harm. order	Rect.	TCW	Hanning	Hamming	Blackman	FD3
1	-0.0414	-1.36e-05	0.0321	-3.44e-03	-1.14e-03	-0.017
2	0.0415	-1.62e-04	-0.0611	-0.0477	1.67e-03	0.231
3	-1.47	-4.74e-04	0.107	-0.134	-0.0134	-0.451
4	-0.504	-2.0e-04	2.42e-04	-0.0751	-0.0103	-0.0485
5	-1.3	-6.67e-04	-5.61e-03	-0.204	-0.0175	-0.0595
6	-0.768	-3.38e-04	-0.0132	-0.126	-0.0256	-0.0704
7	-1.25	-5.62e-04	-0.0616	-0.243	-0.0247	0.111
8	-2.63	-3.09e-04	0.251	-0.18	-0.0637	-1.21
9	-0.141	3.23e-05	-0.063	-0.0748	-0.0594	-0.046
10	3.39	6.51-04	-0.485	0.0864	-0.0696	1.45

TABLE 3.3 Percentage errors in Phase determination

harm. order	Rect.	TCW	Hanning	Hamming	Blackman	FD3
1	-4.52	-7.87e-05	-3.69	-3.81	-3.7	-3.73
2	-6.36	-1.82e-04	-3.69	-4.03	-3.69	-3.95
3	-7.27	-1.15e-04	-3.62	-4.13	-3.69	-4.06
4	-4.47	1.95e-05	-3.59	-3.8	-3.7	-3.75
5	-5.64	2.04e-04	-3.68	-3.91	-3.7	-4.0
6	-4.39	1.65e-04	-3.61	-3.78	-3.7	-3.77
7	-4.89	4.39e-04	-3.64	-3.82	-3.69	-3.9
8	-4.66	5.19e-04	-3.63	-3.78	-3.7	-3.97
9	-3.87	1.87e-04	-3.69	-3.72	-3.7	-3.74
10	-4.25	5.58e-04	-3.66	-3.75	-3.7	-3.85

The number of samples = 750
$\Delta = 0.925007$
The number of periods = 3

For the TCW and modified DFT approach:
The number of samples = 751
$\Delta = -0.074993$
The number of periods = 3

The results indicate the superiority of the algorithm employed in this thesis for the signal under consideration in both amplitude and phase determination for the first ten harmonic components of the signal. Three periods of the signal were used in order

to minimize the medium-range effects due to the wide main lobes of the Blackman and fast-decaying 3-term windows.

3.4.2 Simulated Bandlimited PWM signal

Various switching strategies may be employed to generate PWM waveforms. The regular sampling scheme which is particularly advantageous when implemented using digital or microprocessor techniques will be used [2]. An example of a 2-level regular sampled PWM waveform is shown in Figure 3.6.

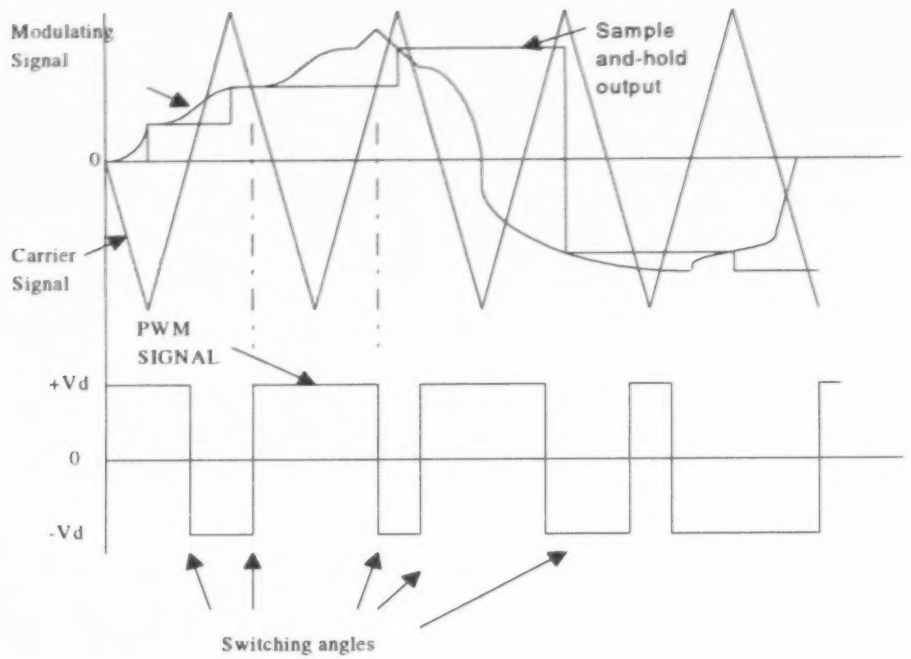

Figure 3.6 2-level regular sampled PWM waveform

In a regular sampling scheme the triangular carrier wave is not compared directly with the sinusoidal modulating signal but with a sampled-and-hold version of it to determine the points of intersection and the switching angles. The sample-and-hold device is enabled to hold the modulating wave value at the time instances corresponding to the peak of the triangular carrier wave. The next switching time the PWM signal changes its levels is when the value of the modulating signal equals that of the carrier wave. This level change instant when expressed in angular units is referred to as the switching angle. The level change is typically in volts. A 2-level

PWM signal can assume one of 2 voltage levels. A 3-level PWM signal can have one of 3 voltage levels.

As previously stated (Section 1.2), the sampling frequency should be greater than the signal Nyquist frequency in order to reduce aliasing effects. One method of achieving this for a theoretical PWM as in Figure 3.5, is to perform a low-pass filtering of the signal prior to sampling. In this simulation a typical 2-level PWM waveform obtained by regular sampling is employed. A sharp cutoff lowpass filter is employed which is assumed to severely attenuate harmonics above the 51st that these can be neglected. The waveform has the following parameters.

Vd = 100 V (Signal swings between +100 and -100 V)
R = 9 (Ratio of the carrier signal frequency to the modulating signal frequency)
M = 0.48 (Ratio of the modulating signal amplitude to the carrier signal amplitude)
harm = 51 (Maximum harmonic order)
f = 24 (Modulating signal frequency in Hertz)

The General PWM waveform can be represented by the Fourier series

$$v_{a0}(t) = \sum_{k=0}^{\infty} C_k \cos\theta_k . \cos(2\pi kft) + C_k \sin\theta_k . \sin(2\pi kft) \tag{3.4.2}$$

In the regular symmetric sampling of PWM signals used [2], the transitions (switching angles) occur at the angles denoted by α_i.

The initial transition from zero to the maximum positive value occurs at: $\alpha_0 = 0$
Subsequent switching values satisfy the equation:

$$\alpha_i = \frac{\pi}{2R}\left\{2i + (-1)^{i+1} M \sin(\frac{i\pi}{R})\right\} \tag{3.4.3}$$

where $i = \{1,2,3.....\}$

Since v_{a0} has quarter and half-wave symmetry, then:

$C_k \sin\theta_k = 0$, for even k

$C_k \cos\theta_k = 0$, for all k

The PWM signal can thus be expressed as [13].

$$v_{a0}(t) = \sum_{k=1}^{\infty} C_k \sin\theta_k . \sin(2\pi kft) \tag{3.4.4}$$

where k takes only odd values.

Since v_{a0} has a constant value between two consecutive switches of the PWM waveform, the expression for odd k values of $C_k \sin\theta_k$ is:

$$C_k \sin\theta_k = \frac{4.Vd}{k\pi}\left[1+2\sum_{i=1}^{N}(-1)^i \cos(k\alpha_i)\right] \tag{3.4.5}$$

where N equals the number of switches per quarter cycle.

Table 3.4 indicates the switching angles obtained.

TABLE 3.4 Switching Angles of Simulated PWM Signal

Switching angle number	Switching angle in degrees
0	0
1	21.642
2	36.915
3	64.157
4	75.273
5	104.73
6	115.84
7	143.09
8	158.36
9	180
10	201.64
11	216.91
12	244.16
13	255.27
14	284.73
15	295.84
16	323.09
17	338.36
18	360

Using these switching angles, the harmonic components of the PWM waveform are computed using equation 3.4.5. These results are tabulated in Table 3.5

TABLE 3.5 The Harmonic Components of the PWM Waveform based on Switching Angles and Parameters indicated

Harmonic Order	C_k	$C_k\cos\theta_k$	$C_k\sin\theta_k$	θ_k/degrees
0	0	0	0	0
1	47.958	0	47.958	90
3	0.12584	0	0.12584	90
5	0.018978	0	0.018978	90
7	6.8377	0	6.8377	90
9	109.86	0	109.86	90
11	10.296	0	10.296	90
13	0.27079	0	0.27079	90
15	-2.8524	0	2.8524	-90
17	-36.816	0	36.816	-90
19	34.321	0	34.321	90
21	5.1129	0	5.1129	90
23	1.7757	0	1.7757	90
25	17.128	0	17.128	90
27	3.2345	0	3.2345	90
29	17.189	0	17.189	90
31	2.2404	0	2.2404	90
33	-8.986	0	8.986	-90
35	-11.902	0	11.902	-90
37	9.3434	0	9.3434	90
39	10.918	0	10.918	90
41	7.5238	0	7.5238	90
43	12.059	0	12.059	90
45	-10.237	0	10.237	-90
47	8.9098	0	8.9098	90
49	3.5556	0	3.5556	90
51	-8.2473	0	8.2473	-90

The theoretical PWM waveform is shown in Figure 3.7. The lowpass filtered waveform derived from that in Figure 3.7 and used for the subsequent analysis is plotted in Figure 3.8.

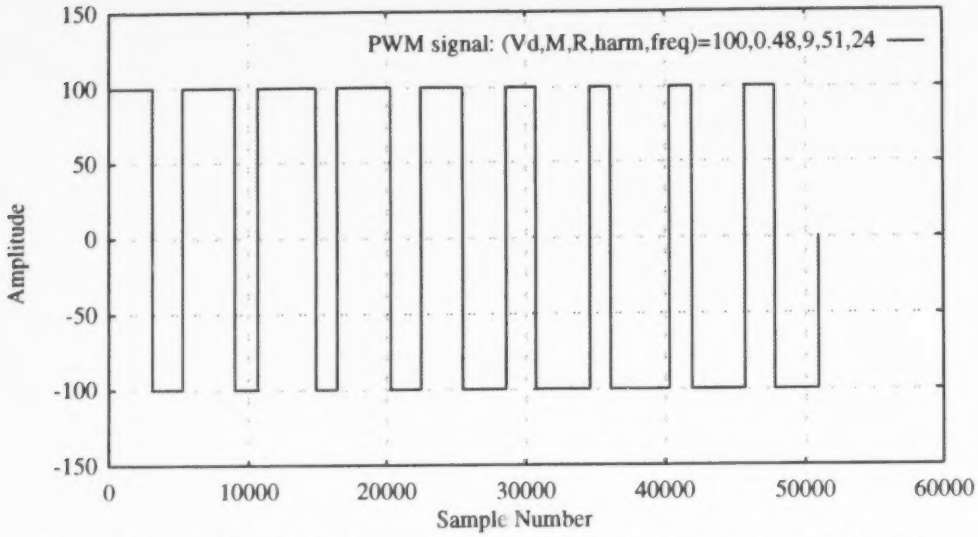

Figure 3.7 Plot of PWM waveform based on switching angles in Table 3.4.

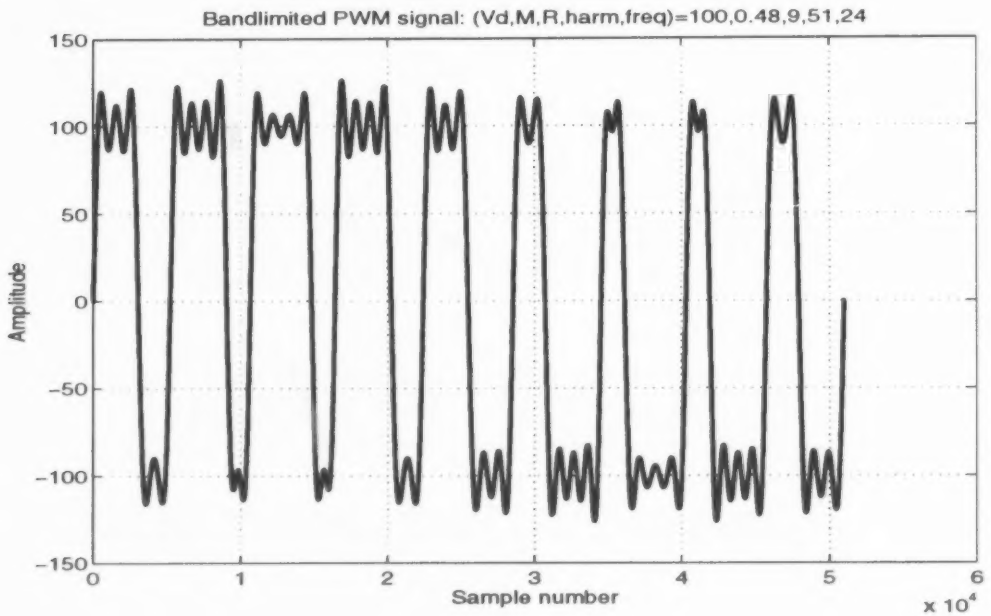

Figure 3.8 Plot of Low-Pass Filtered PWM waveform for parameters and values in Table 3.5

The DFT was applied to the signal in Figure 3.8, using various windows. In addition, the TCW and the modified DFT algorithm were applied to the signal. The maximum harmonic order of 51 implies a maximum signal frequency of 1224Hz. A sampling frequency of 24.995kHz is used. The percentage errors for the magnitude

and phase results are tabulated in Table 3.6 and Table 3.7 respectively. Three periods of the signal were used in order to minimize the medium-range effects due to the wide main lobes of the fast-decaying 3-term window. The extreme ringing, sharp transitions and sampling frequency to maximum signal frequency of 20.4 make it a challenging measurement case.

TABLE 3.6 Percentage errors in Low Pass Filtered PWM Signal Magnitude determination (3 periods)

Harm	Rect.	TCW	Hann	Hamm	Black	FD3
1	-0.176	0.000296	0.00028	-0.0259	0.000104	-0.000537
3	-67.1	0.114	0.0176	-9.92	0.0115	-0.0106
5	312	0.778	1.63	-74.4	0.649	-2.92
7	-1.85	0.00224	0.0251	-0.253	0.00883	-0.0505
9	-0.0664	0.000147	-0.000541	-0.0103	-0.000476	-0.000241
11	-0.124	0.00166	-0.0168	-0.0326	-0.00637	0.0315
13	-17.6	0.0674	-0.0548	-2.65	-0.0205	0.105
15	-3.02	0.00687	0.0382	-0.415	0.013	-0.079
17	-0.212	0.000575	0.000469	-0.0309	-0.000849	-0.00566
19	-0.0423	0.000667	-0.00552	-0.011	-0.00324	0.00508
21	0.0512	0.00486	-0.0246	-0.0133	-0.0104	0.0415
23	-1.94	0.0152	0.0202	-0.271	0.00498	-0.0505
25	-0.197	0.00171	-0.00447	-0.033	-0.00379	-0.00128
27	-0.932	0.00984	-0.00168	-0.14	-0.00315	-0.00853
29	-0.15	0.00201	-0.0072	-0.0283	-0.00553	0.000536
31	-0.777	0.0167	-0.0197	-0.132	-0.0103	0.0243
33	-0.429	0.00451	-0.0025	-0.0657	-0.00473	-0.0129
35	-0.225	0.00368	-0.00884	-0.0409	-0.00744	-0.00234
37	-0.175	0.00507	-0.0108	-0.0352	-0.00868	-0.000798
39	-0.0802	0.00467	-0.0129	-0.0229	-0.00995	0.000815
41	-0.0794	0.0073	-0.0115	-0.0216	-0.01	-0.00459
43	0.0038	0.00489	-0.0134	-0.0108	-0.0113	-0.00375
45	0.241	0.00618	-0.0189	0.0195	-0.0139	0.00434
47	0.494	0.0076	-0.0246	0.0523	-0.0166	0.0124
49	1.27	0.0203	-0.0238	0.167	-0.0172	0.00681
51	0.662	0.00936	-0.0271	0.0751	-0.0189	0.0107

TABLE 3.7 Percentage errors in Low Pass Filtered PWM Signal Phase determination (3 Periods)

Harm	Rect	TCW	Hann	Hamm	Black	FD3
1	-0.072	6.38e-07	-0.072	-0.072	-0.072	-0.072
3	-0.213	0.000732	-0.216	-0.216	-0.216	-0.216
5	200	0.00811	-0.364	-0.368	-0.362	-0.353
7	-0.504	3.22e-05	-0.504	-0.504	-0.504	-0.504
9	-0.648	2.62e-06	-0.648	-0.648	-0.648	-0.648
11	-0.792	3.5e-05	-0.792	-0.792	-0.792	-0.792
13	-0.934	0.00161	-0.937	-0.936	-0.936	-0.935
15	-1.08	0.000182	-1.08	-1.08	-1.08	-1.08
17	-1.22	1.65e-05	-1.22	-1.22	-1.22	-1.22
19	-1.37	2.04e-05	-1.37	-1.37	-1.37	-1.37
21	-1.51	0.000157	-1.51	-1.51	-1.51	-1.51
23	-1.66	0.000516	-1.66	-1.66	-1.66	-1.66
25	-1.8	6.06e-05	-1.8	-1.8	-1.8	-1.8
27	-1.94	0.000362	-1.94	-1.94	-1.94	-1.94
29	-2.09	7.65e-05	-2.09	-2.09	-2.09	-2.09
31	-2.23	0.000656	-2.23	-2.23	-2.23	-2.23
33	-2.38	0.000182	-2.38	-2.38	-2.38	-2.38
35	-2.52	0.000153	-2.52	-2.52	-2.52	-2.52
37	-2.66	0.000216	-2.66	-2.66	-2.66	-2.66
39	-2.81	0.000204	-2.81	-2.81	-2.81	-2.81
41	-2.95	0.000327	-2.95	-2.95	-2.95	-2.95
43	-3.1	0.000225	-3.1	-3.1	-3.1	-3.1
45	-3.24	0.00029	-3.24	-3.24	-3.24	-3.24
47	-3.38	0.000365	-3.38	-3.38	-3.38	-3.38
49	-3.53	0.001	-3.53	-3.53	-3.53	-3.53
51	-3.67	0.000471	-3.67	-3.67	-3.67	-3.67

The number of samples = 3125
$\Delta = 0.375$
The number of periods = 3

The same waveform is used with the same sampling periods however the sampling was performed over one period. As is to be expected, the errors are considerable for the wider main lobe windows. The percentage errors obtained are shown in Tables 3.8 and 3.9 for the ampitude and phase errors respectively

TABLE 3.8 Percentage errors in Low Pass Filtered PWM Signal Amplitude determination (1 Period)

Harm	Rect	TCW	Hann	Hamm	Black	FD3
1	-0.646	0.000996	0.0113	-0.0861	9.56	44.4
3	45.8	0.385	0.0262	-36.4	3.63e+03	1.69e+04
5	1.68e+03	2.62	60.2	26.6	3.54e+03	1.62e+04
7	-6.8	0.00756	1.09	-0.0775	155	715
9	-0.24	0.000494	0.00457	-0.0316	1.49	6.92
11	-0.45	0.00559	-0.677	-0.643	101	471
13	-64.5	0.227	-2.19	-11.4	459	2.14e+03
15	-11.1	0.0231	1.71	-0.182	126	581
17	-0.763	0.00194	0.121	-0.00985	9.81	45.1
19	-0.139	0.00225	-0.11	-0.115	11.5	53.6
21	0.197	0.0164	-0.883	-0.723	65.8	309
23	-7.13	0.0512	1.13	-0.0904	121	560
25	-0.695	0.00576	0.0236	-0.0829	2.81	13
27	-3.41	0.0331	0.212	-0.325	101	470
29	-0.511	0.00676	-0.0163	-0.0896	3.01	14.1
31	-2.85	0.0563	-0.488	-0.838	110	514
33	-1.53	0.0152	0.278	0.0102	15.4	70.7
35	-0.778	0.0124	0.0488	-0.0736	14.7	68.2
37	-0.593	0.0171	0.0218	-0.0694	23.3	108
39	-0.235	0.0157	-0.0183	-0.0504	14.7	68.2
41	-0.235	0.0246	0.11	0.0589	29.2	135
43	0.0873	0.0165	0.0808	0.0817	14.2	65.5
45	0.96	0.0208	-0.0883	0.0669	19.4	90.4
47	1.9	0.0256	-0.267	0.0542	14.3	67.6
49	4.71	0.0684	-0.102	0.611	46	214
51	2.54	0.0315	-0.24	0.172	3.82	18.6

TABLE 3.9 Percentage errors in Low Pass Filtered PWM Signal Phase determination (1 Period)

Harm	Rect	TCW	Hann	Hamm	Black	FD3
1	-0.0881	2.63e-06	-0.088	-0.088	-0.0727	-0.0342
3	200	0.00301	-0.277	-0.281	-0.093	-0.089
5	200	0.0328	-0.555	200	-0.606	-0.608
7	-0.616	0.000133	-0.618	-0.618	-0.723	-0.77
9	-0.792	1.08e-05	-0.792	-0.792	-0.793	-0.795
11	-0.968	0.000144	-0.97	-0.969	-0.88	-0.824
13	-1.12	0.00662	-1.17	-1.17	-1.06	-1.05
15	-1.32	0.000748	-1.32	-1.32	-1.42	-1.47
17	-1.5	6.78e-05	-1.5	-1.5	-1.51	-1.54
19	-1.67	8.41e-05	-1.67	-1.67	-1.66	-1.63
21	-1.85	0.000648	-1.85	-1.85	-1.79	-1.73
23	-2.02	0.00212	-2.03	-2.03	-2.08	-2.11
25	-2.2	0.00025	-2.2	-2.2	-2.2	-2.21
27	-2.38	0.00149	-2.38	-2.38	-2.38	-2.38
29	-2.55	0.000315	-2.55	-2.55	-2.55	-2.55
31	-2.73	0.0027	-2.73	-2.73	-2.7	-2.68
33	-2.91	0.000751	-2.91	-2.91	-2.92	-2.95
35	-3.08	0.00063	-3.08	-3.08	-3.08	-3.08
37	-3.26	0.000889	-3.26	-3.26	-3.26	-3.25
39	-3.43	0.000841	-3.43	-3.43	-3.43	-3.43
41	-3.61	0.00135	-3.61	-3.61	-3.61	-3.62
43	-3.79	0.000924	-3.79	-3.79	-3.79	-3.8
45	-3.96	0.00119	-3.96	-3.96	-3.96	-3.95
47	-4.14	0.0015	-4.14	-4.14	-4.13	-4.1
49	-4.31	0.00412	-4.32	-4.32	-4.31	-4.31
51	-4.49	0.00194	-4.49	-4.49	-4.48	-4.46

The number of samples = 1042
$\Delta = 0.458333$
The number of periods = 1

3.5 Summary of results

It should be noted that in these simulations it is assumed that all the classical windowing methods are being employed in a scheme which allows the record length to be within one sample interval of an integral number of signal cycles. It should be stated

that this is not the general case in existing instrumentation and much larger errors could be expected than those obtained when the above-mentioned record length condition is not valid. The results indicate the improvement in measurement accuracy obtained using the TCW approach, this confirms the theoretical relations obtained. The accuracy in the measurement of the harmonic magnitudes using the TCW algorithm compared to the other methods employed is far superior in the 1st signal example. Both amplitude and phase measurements are improved by a least a factor ten over that of the algorithm proposed in [4].

The results obtained using the bandlimited simulated PWM signal also indicates good measurement accuracy with the TCW algorithm. In the 3 period case, although the magnitude errors were not always better than the other methods, the error values were in most cases comparable to the best among the other methods. The phase measurements were far better than the other methods. The measurements were taken over more than one cycle of the signal fundamental period due to the wide main lobes of some of the windows used. This results in a more appropriate comparison.

It must be pointed out that some situations exist where only a single cycle of the input waveform is available. In such situations, windows which contribute appreciable medium-term and short-term leakage over a single cycle, will provide inaccurate results for the very low harmonic frequency measurements. The use of the TCW and the modified DFT algorithm can achieve accurate results even when only a single period of the given waveform is available. This is demonstrated by the results in Tables 3.8 and 3.9. A scheme for a TCW-based measuring setup in such a case could be the use of two sets of analog-to-digital converters and Δ determination schemes, with each being employed for alternate signal cycles. Analysis can be performed following each cycle of sampled values to obtain the relevant harmonic components. The system hardware platform for this thesis did not have the flexibility to perform this type of analysis.

The accurate magnitude and phase results by using the TCW algorithm translate directly into accurate real and imaginary values for the Fourier series components of the signal under consideration.

4. THE FOURIER ANALYZER HARDWARE

The TCW algorithm is implemented on hardware which is a modification of the sampling wattmeter constructed previously [11]. The main modifications being the use of programmable logic devices to reduce the chip count and a current sensing module in place of shunt resistors for current sensing. Readily available software and hardware tools led to the choice of a 16-bit 68000 microprocessor running at 8MHz with no wait states. The analyzer uses easily available off the shelf components and has 4 input channels (2 voltage channels and 2 current channels). 12-bit Analog-to-Digital converters are used. The microprocessor design facilitates the incorporation of simple hardware support for debugging, thus simplifying system maintenance.

The hardware description is based on the sub-units detailed in the Fourier Analyzer block diagram in Figure 4.1. The sub-units being; the CPUmain module, the memory module, the EPLD1 module, the I/O module, the timing-controller module, the analog-to-digital interface module, the input module and the power supply module.

The circuit schematics can be found in the Appendix.

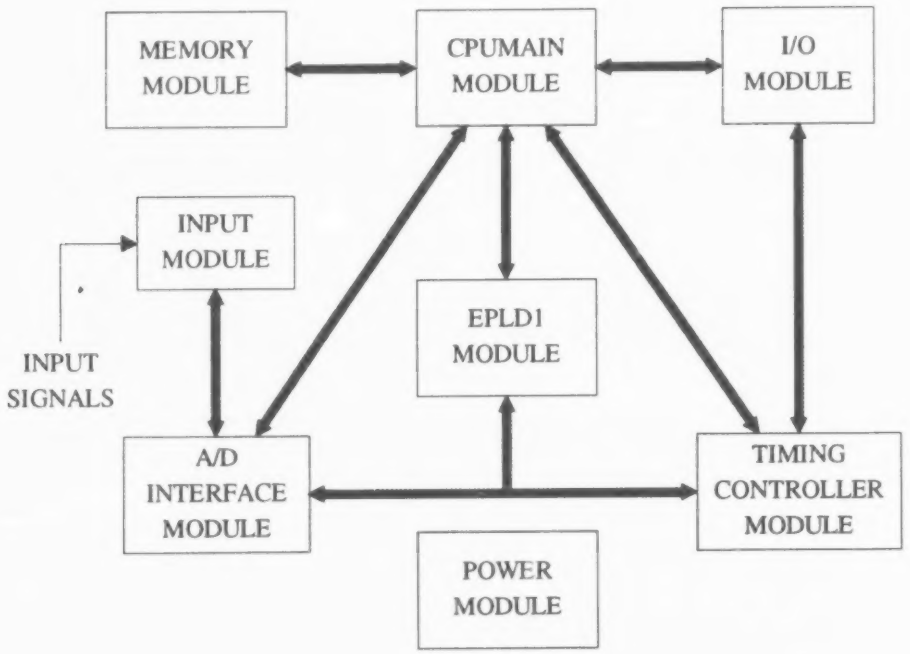

Figure 4.1 Block diagram of Fourier analyzer

4.1 CPUmain Module

The block diagram of this circuitry is shown in Figure 4.2. The system clock comprises an 8MHz oscillator module. A 74LS245 IC is employed as a buffer for the bidirectional data bus, while two 74LS244 ICs are employed for buffering the unidirectional address lines and the R/W* , EClock, AS* and reset* lines.
The reset circuitry is a 100µs one-shot circuit based on a 555 timer design. This provides the required processor reset signal on power up.

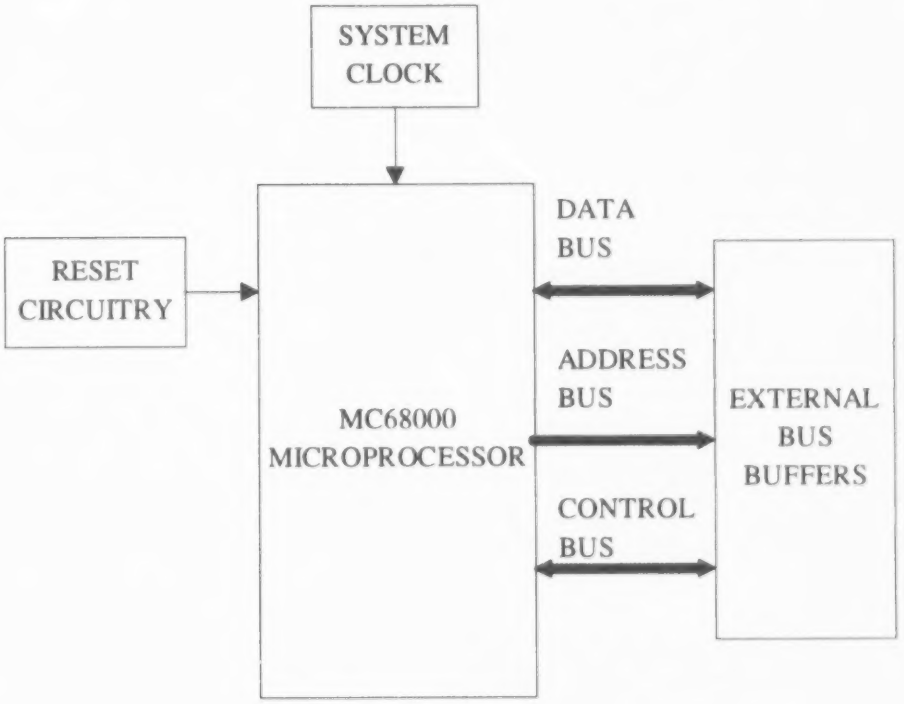

Figure 4.2 Block diagram of Cpumain module

4.2 Memory module

The block diagram of this module is shown in Figure 4.3. The 16-bit data bus of the microprocessor necessitates the use of a pair of byte-wide memory devices. The components employed are thus two 150ns 32KB byte-wide SRAMs (20256) as well as two 200ns 32KB byte-wide EPROMS (27C256). The latter devices store the program code and other permanent data. Decoding the EPROMS at base address 000000hex results in a simplified reset and interrupt circuitry. The static RAMs are decoded at a base address starting at 200000hex and store the sampled data as well as temporary

variables. 16K of 16-bit words are allocated for the storage of the sampled data values. Each 12-bit ADC output is stored as a 16-bit value. This implies a maximum of 4096 16-bit values per channel. The top 2K bytes of the SRAM address space is allocated to the system stack.

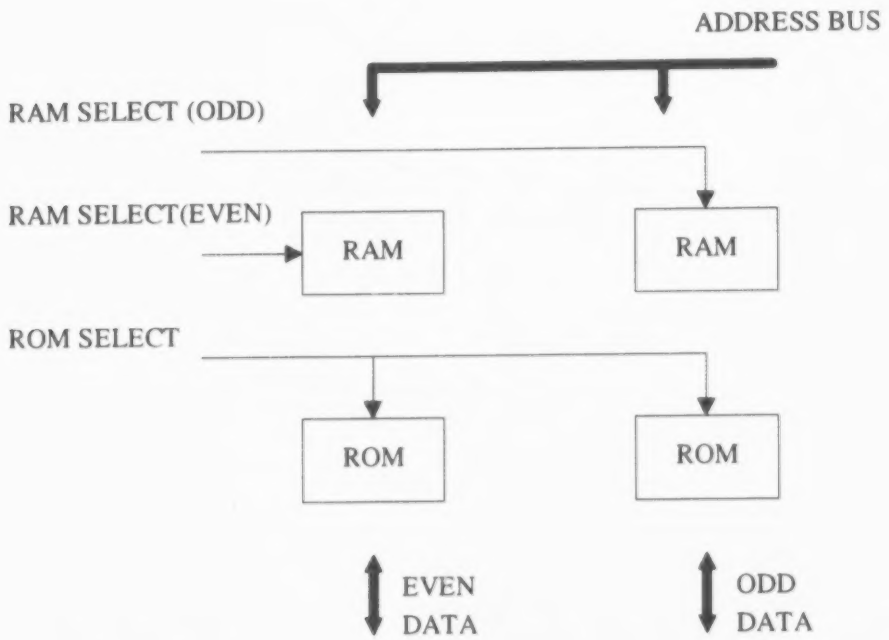

Figure 4.3 Block diagram of memory module

4.3 EPLD1 module

This module consists of a 68-pin Intel D5C180 (equivalent to the Altera EP1800) erasable programmable logic device.

The D5C180 IC performs all the address decoding for the I/O devices, the analog-to-digital converter data latches and the gainsetting ICs. The microprocessor signals; BERR*, DTACK* and VPA* are also generated by this IC. In addition, it generates the signals required by the microprocessor in order to process device interrupts and generates the signal (BUFFEN) which enables the buffers on the Cpumain module for signal transfer to the other modules. A final function is the selection of the channel to serve as the trigger source (By default, channel 1 is selected).

The 68000 microprocessor utilizes a memory-mapped addressing scheme. The 16 Megabyte direct address space is utilized as characterized as indicated in Figure 4.4.

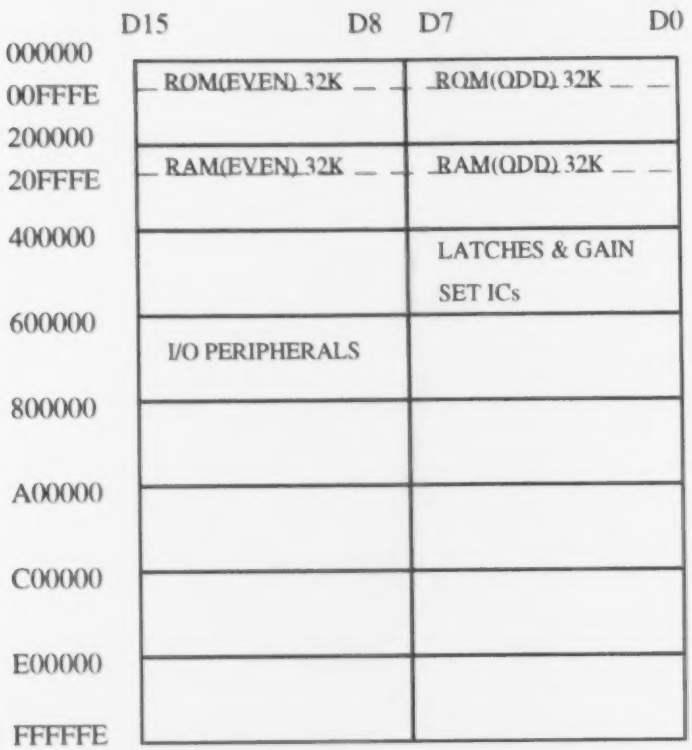

Figure 4.4 System Memory map

A partial address decoding scheme is employed. At the heart of the decoding devices is a 1-of-8 decoder. Using address lines A21-A23, 8 address blocks are obtained, as indicated in the system memory map in Figure 4.4. The 68000 Address strobe line (AS*) enables the 1-of-8 decoders. Addresses in the 000000_{16} - 20000_{16} block enable the ROMs. Even addresses in the 200000_{16} to $3FFFFF_{16}$ select the even RAM (the corresponding 1-to-8 decoder output ORed with UDS*) while odd addresses in the 200000_{16} to $3FFFFF_{16}$ select the odd RAM (the corresponding 1-to-8 decoder output ORed with LDS*). The latches and gainset ICs have the following addresses

Device Address	Device
400001_{16}	latch1
400003_{16}	latch2
400005_{16}	latch3
400007_{16}	latch4
400009_{16}	gainset1
$40000b_{16}$	gainset2
$40000d_{16}$	gainset3
$40000f_{16}$	gainset4

In a similar manner, further partial address decoding of address block 600000_{16} to $8FFFFF_{16}$ is done using address lines A18-A20, to obtain the following device addresses.

Device Address	Device
600000_{16}	6840 PTM
640000_{16}	GPIA
680000_{16}	PIA
$6C0000_{16}$	LCD display
700000_{16}	Keyboard decoder IC

The output of the EP310 IC is accessed by decoding a location denoted tim_latch at address 800001_{16}. This partial address decoding scheme is adequate for this instrument.

The $\overline{BERR}$ signal of the microprocessor is asserted if, following a valid AS* signal, AS* is not deasserted in 4 E clock cycles (40 system clock cycles). The hardware circuitry is a 4-bit shift register formed by 4 D Flip-Flops.

The interrupt generating devices, the PTM, Keyboard decoder IC and the GPIA are assigned autovector interrupt levels 4,5 and 6 respectively.

A simple phase detector indicating if the voltage in a phase leads the corresponding current is provided by applying the comparator outputs of each channel to a D Flip-Flop. The voltage outputs are applied to the data (D) inputs and the current outputs to the clock input. During an AC acquisition cycle, a high on the flip-flop output indicates the current lags the voltage, and a low that the current leads the voltage. The outputs of these labeled phase 1 and phase 2 are subsequently applied as inputs to the PIA.

The comparator outputs are also applied to a 4-input multiplexer which provides the trigger signal employed in the timing controller module. Two trigger select inputs obtained from the PIA outputs, select the appropriate signal source under software control.

4.4 I/O Module

This module consists of 5 peripherals interfacing to the 68000 microprocessor via the synchronous control signals. The peripherals are the GPIA, PIA, PTM, Keyboard controller IC and the Display.

The PTM subunit is centered around the 6840 programmable timer module. This unit is employed in the detection of an AC signal in the RMS and DFT modes. In these modes, the output of timer 1 is connected to the input of timer 2. The gate input of timer 1 is connected to the trigger signal line. The frequency of the trigger signal is also obtained, in the frequency mode, using the period measurement function of the PTM. The detailed circuit diagram of this unit is shown in the Appendix.

The keyboard controller circuitry is centered around the Intel 8279 programmable keyboard and display controller IC. This unit decodes a key input via the 4 by 4 matrix keypad and interrupts the microprocessor accordingly.

The PIA subunit is based on a 6821 peripheral interface adapter IC. This unit serves as a microprocessor controlled latch. Port A lines are configured as outputs driving the 7 LEDs in the DISPLAY subunit. Bit 0 of PORT A also drives the input relays to disconnect the input terminals from the rest of the system. Port B has 2 inputs (Phase 1 and Phase 2), which determine if a leading or lagging phase is present on channels 1 or 2 , as previously mentioned in the EPLD1 module description. The other 6 output lines of Port B provide the ST (start), AC_PIA (ac signal mode), EN_KEYB (enable keypad), REM/LOC (remote/local), TRIG_SEL1 and TRIG_SEL2 signals. Keypad interrupts are only enabled when both EN_KEYB and REM/LOC are at a logic 1. This is the default power-up state. These outputs perform the interrupt masking function in the EPLD1 module. TRIG_SEL1 and TRIG_SEL2 select the input trigger source in the EPLD1 module.

The DISPLAY subunit utilizes a 4 by 20 column LCD display and a set of 7 LEDs for results and status indication. The LEDs are activated through port A of the PIA.

The GPIA subunit is centered around the 68488 GPIA IC. It can be configured as a listener or talker as per the IEEE 488.1 specifications.

4.5 Timing-Controller Module

This module comprises a 5C090 erasable programmable logic device and a 20-pin EP310 erasable programmable logic device. The schematic of this circuitry is in the Appendix. The 5C090 IC generates the clock and other timing signals for the sample and hold as well as the analog-to-digital converters. The timing signals are generated from the master 8MHz CPU clock in order to minimize jitter, although the circuitry also allows the connection of an external clock source. This allows the implementation of an external clock source based on a multiple of the 'trig' signal, and hence the input signal source, thus allowing a synchronous sampling system implementation. Each channel signal is low-pass filtered and passed through a separate zero-crosing detector to generate a square wave. The selected square wave is the 'trig' signal which is used for the determination of Δ as well as frequency measurement. The 1 Mhz A/D converter clock signals is generated by a 4-bit counter clocked by the 8MHz system clock. A second 4-bit counter produces the 2µs start of conversion signal (CS_ADC) at 32µs intervals (also the sampling interval) from the terminal count output terminal of the previous 4-bit counter. However an option of generating this signal through an external clock source based on a multiple of the "trig" signal, and hence the input signal source, is provided, thus allowing a near synchronous sampling system implementation. The S/H signal required for the sample-and hold devices is produced by a logical NANDing of the CS_ADC signal and the ADC BUSY signals. This module provides the 2 types of sampling modes required. In the DC case where the

signals are not gated to the input signal, and the AC case where this gating is required as well as information on the position in the current signal cycle being sampled, to indicate if sampling should be continued or terminated after 1 or 2 samples. Under software control, the signals ST (start sampling) and AC_PIA (set to a logic 1 if an AC or DFT mode acquisition cycle is requested) are provided by the PIA. Two D flip-flops in addition provide the signal cycle information required. This has been detailed in the software section. The signal ZC (zero-crossing) is obtained by doubling the period of the 'trig' signal in a divide-by-2 circuit. This signal is thus at a logic 1 for the duration of the selected signal input period.

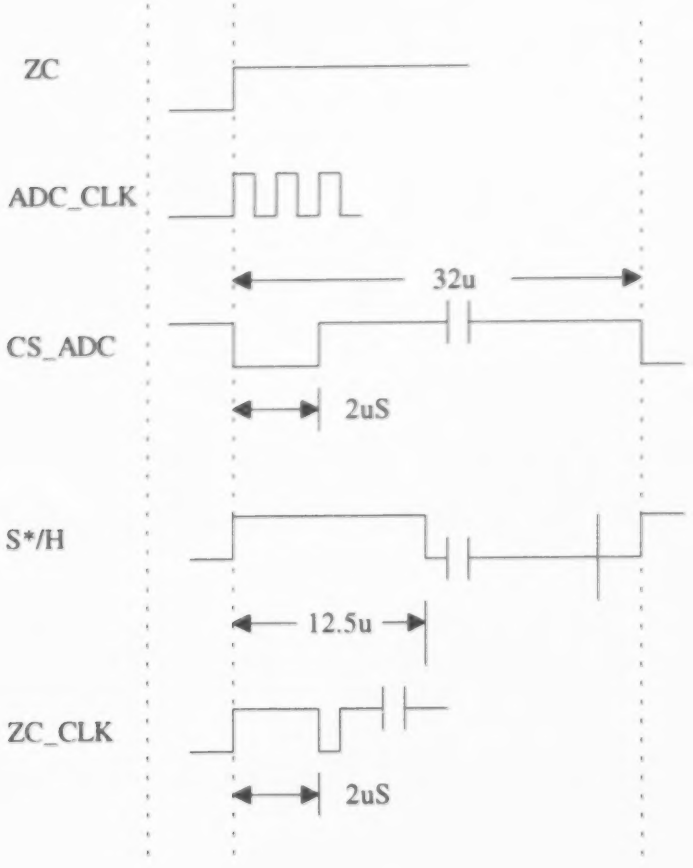

Figure 4.5 Timing relationships among timing-controller signals

The EP310 IC performs the determination of the end-correction (Δ) employed in the computations involving periodic signals by utilizing a counter, identical in function to the 74161 4-bit binary counter, clocked by the terminal count output (ZC_CLK). The up-counting sequence of the 16-bit counter is inhibited until a

logic high occurs on the ZC line (indicating the start of a cycle) connected to the enable P and T inputs of the counter. The value held when ZC goes low is thus 16*Δ.

The timing relationships for some signals in this module are indicated in Figure 4.5. Due to the non-zero propagation delay through the components, the following signal delays were obtained by an actual measurement. ZC leads CS_ADC by 250ns. ZC also leads ADC_CLK by 200ns. In addition, ZC leads ZC_CLK by 100ns.

4.6 Analog-to-Digital Interface Module

The block diagram of this module is shown in Figure 4.6 below. This module consists of 4 similar sections each comprising a 12-bit A/D converter, a S/H amplifier, 2 latches for storing the results of a conversion and an input OPAMP for scaling and translating the [-10, +10] input voltage range to the [0,5] volt range required for the ADCs employed. The 12-bit ADC implies that the output can have 1 of 2^{12} (4096)) values. Thus a one-bit output value will occur for an input voltage change of $5/2^{12}$ volts (1.22mV). Thus the input voltage change at the scaling opamp inputs required for a one-bit change at the ADC output will be 4.88mV (1.22mV*20/5). Based on this calculation, the results are displayed to a maximum of two decimal places. It will of course be expected that using a signal of -500 to +500V will produce a one-bit ADC output change for an input change of 0.244V (4.88mV*500/10). The latched ADC outputs enable the conversion results to be read at will without affecting ongoing conversions. During an acquisition cycle, samples are generated every 32μs. The latches are decoded as synchronous memory-mapped devices.

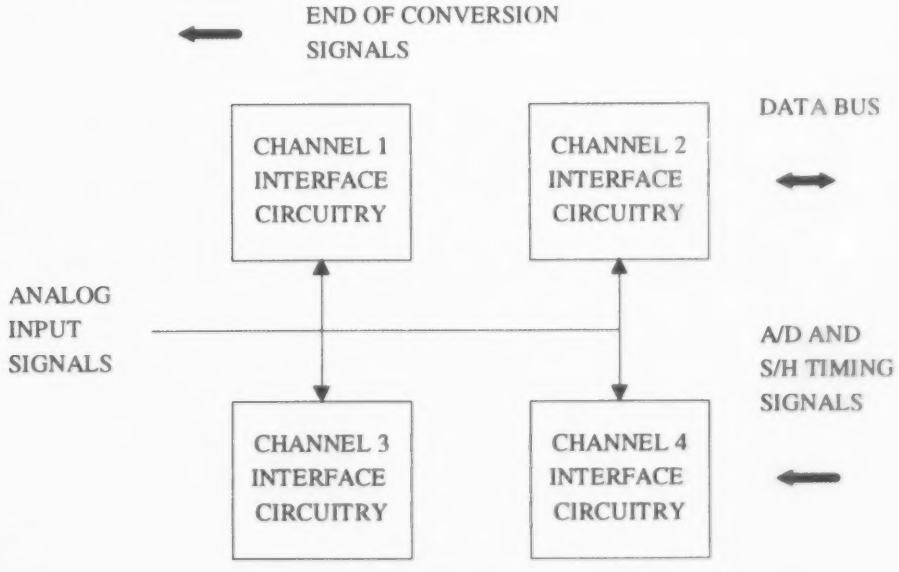

Figure 4.6 Block diagram of Analog-to-Digital interface module

4.7 Input Module

This module comprises 3 subunits: the phase 1 subunit, phase 2 subunit and the comparator subunit. The block diagram of this module is shown in Figure 4.7.

Phase 1 and phase 2 units each handle one voltage and one current input. The voltage section has an input resistive attenuator, followed by a buffer amplifier and a variable gain stage. The variable voltage gain stage comprises a non-inverting opamp and a gainset IC which simply allows one to select various resistor combinations thus varying the gain of an opamp. The voltage signal from this stage is fed to the comparator subunit and the analog-to-digital interface module. The gainset ICs are decoded as synchronous memory-mapped devices.

The current is sensed by a coil wound around a current sensing module (Manufactured by LEM of Switzerland) which produces a voltage proportional to the coil flux density, and hence to the current. The output is fed through a buffer opamp stage and a variable voltage gain stage similar to that in the voltage section outline above. The voltage signal from this stage is fed to the comparator subunit and the analog-to-digital interface module.

The comparator subunit consists of 4 separate zero-crossing detectors which each generate a TTL compatible square wave based on each channel input signals.

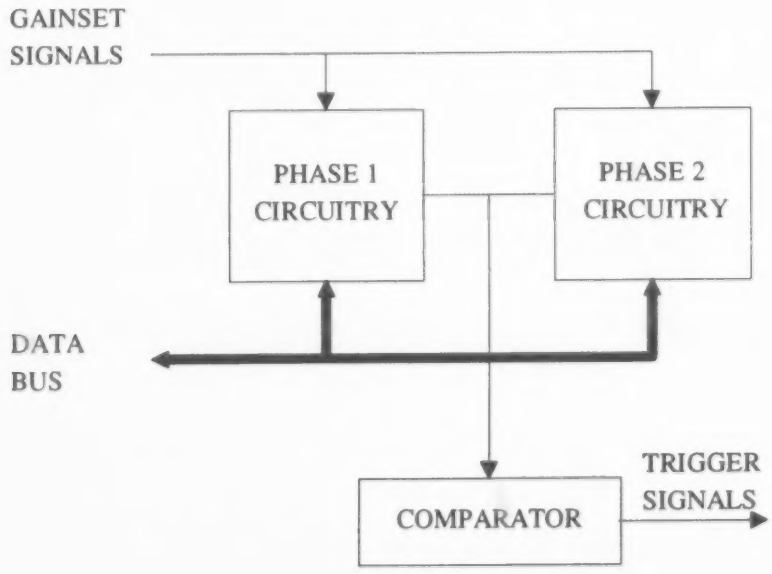

Figure 4.7 Block diagram of the Input module

4.8 Power Supply Module

This subunit generates the onboard DC supply voltages of +5V, +15V and -15V.

The 5V DC is generated by a full-wave rectified AC voltage from a step-down transformer which is then regulated by a LM338 IC. A 48VA 115-8V transformer is used.

The +15V and -15V DC voltages are provided by a full-wave rectified and regulated AC from a 115-12V 48VA transformer. Regulation for the +15V line is provided by a LM317 and the -15V line by a LM337 IC.

5. FOURIER ANALYZER SOFTWARE

The software scheme employed in the Fourier analyzer is discussed in this chapter. An overview of the software scheme will be introduced. This will be followed by a description of the various software modules. Flowcharts will be used in describing the program flow in each module.

The software structure is geared towards the efficient and speedy implementation of the necessary mathematical manipulations and other analyzer functions required. This ties in suitably with the design goal of implementing a very accurate system using reasonably priced off-the-shelf components.

The hardware and software marriage is effectively achieved with 'idle' periods such as occur during sampling intervals being utilized for program code execution by the microprocessor.

With ease of use and maintenance in mind, a user-friendly software interface is provided, as well as routines to simplify the system calibration and maintenance. The majority of the system routines were implemented using the C programming language, and cross-compiled to 68000 assembly language. The time-critical routines were however implemented directly in assembly language.

5.1 Software Overview

The flowchart in Figure 5.1 indicates the program flow of the Fourier analyzer.

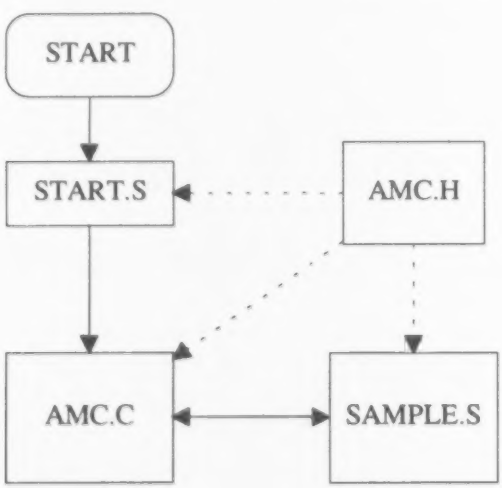

Figure 5.1 Program files interactions

The source code for the program consists of a single 'C' language file (AMC.C) and two 68000 assembly language files (START.S and SAMPLE.S). Definitions of various constants and labels required by the assembler and 'C' source files are included in the header file, amc.h. The microprocessor runs in the default supervisor mode. The code whose source is in file start.s, is executed by the system on startup. The operations performed by this include setting up the stack pointer, pointer size allocations as well as memory allocation for the malloc() function when required. Other functions performed by the code indicated by the start.s file include initializing the 256 vectors, zeroing out uninitialized RAM, initializing other RAM from ROM, and then finally transferring program execution to the main program (source file amc.c). The final object code is obtained after linking the 'C' and assembly language files with the 'C' compiler code for floating point arithmetic. The absence of a math coprocessor entails all the computations being performed in software.

The file SAMPLE.S is a 68000 assembly language code source file. The compiled code, when executed, acquires and stores the resulting data during a data acquisition cycle. The process involves setting up the ADC and sample-and-hold devices as well as the detection of the presence of a low frequency signal using a countdown timer in the PTM IC. Two subroutines are used; acquire_ac (used for AC signals) and acquire_dc (for DC signals). In both subroutines, following the issuance of the start of conversion signal, the microprocessor acquires the latched data. This resulting two's complement value, obtained when the respective channel 16-bit zero offset is subtracted from the latched 16-bit value, is subsequently stored in the static RAM devices. This process is performed for all 4-channels well within the 32μs sampling interval. In the acquire_dc routine, 1024 samples are acquired. In addition to acquiring samples and storing the sampled values in the two's complement format, the acquire_ac routine determines the state of the sampling process during an AC acquisition cycle. This determination is performed immediately after the results of the previously converted analog input signals of all 4 A/D converters have been stored in the system RAM. An AC acquisition cycle is the time interval during which the crossing signal (ZC) is at a logic high state, (which is a period of the input waveform) obtained by using a comparator. The software procedure for obtaining the state information is the logic state of lines D0-D4 of the EP310 EPLD chip. Based on the information obtained, a look-up table (Table 5.1) is used to determine the next stage of program execution as indicated below.

TABLE 5.1 Software and Hardware interaction in sampling routine

Logic state of relevant line of EP310				**Action taken by routine**
BD3(1Q)	BD2(2Q)	BD1(ZC)	BD0	
0	0	0	*	Restart sampling
0	0	1	*	Restart sampling
0	1	0	*	Restart sampling
0	1	1	*	Restart sampling
1	0	0	*	Stage 1 (One more sample required)
1	0	1	*	Continue(1st conversion underway)
1	1	0	*	Stage 2 (2 more samples required)
1	1	1	*	Continue(ZC high)

* - A don't care condition

In all the computations, the results are immediately displayed prior to computing the next value. For computation of power values, the sample values used for subsequent computations are obtained by multiplying corresponding voltage and current samples.

5.2 The Main Program

The flowchart for this module is indicated in Figure 5.2. This module primarily contains code generated from the compilation of the C source file amc.c. This section begins with the disabling of all system interrupts. Subsequently, the flip-flops and timing controller are initialized. This is followed by the initialization of the microprocessor peripheral devices namely; the 6821 PIA, the 8279 programmable keyboard and display controller IC, the 6840 PTM, the LCD display and finally the MC68488 GPIA IC. The routines executed are; pia_init(), key_init(), time_init(), disp_init() and gpia_init() respectively.

On successful completion of the above procedure, the voltage, current and power scale factors are stored in the static RAMs. Next, the program mode variables are initialized and all interrupts are enabled. Subsequently, the analog-to-digital interface module has its inputs switched to the outputs of channels 1 to 4. All microprocessor interrupts are enabled.

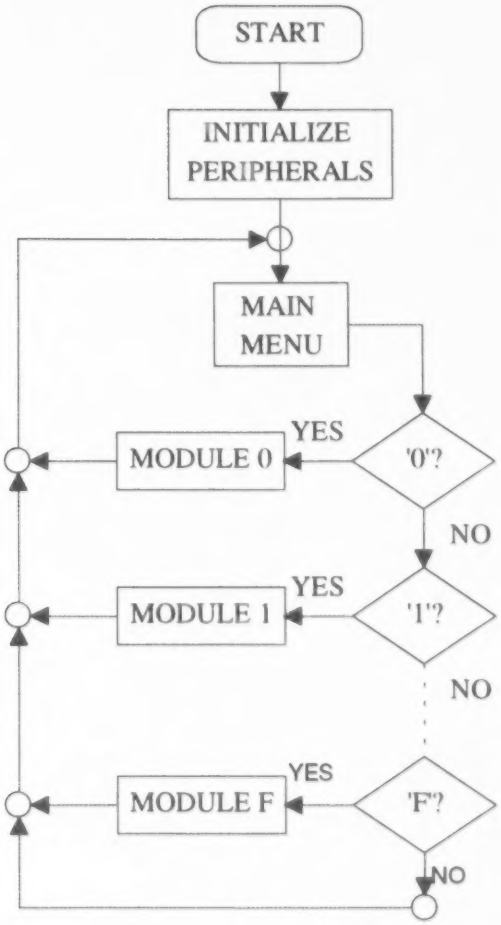

Figure 5.2 Flowchart of main program code in file AMC.C

5.2.1 The Main Menus

The routines used in this stage are the input and LCD string display routines. 4 menu screens are possible, since each key of the 16 key keypad is allotted a single line item in each menu. FOUR menu screens are used. The last menu having no key assignments. Following a system reset or power-up, Menu 1 is displayed. The screen displays relating to normal system functioning are indicated in Figure 5.3 . The display of the next menu is always initiated when an F is entered on the keypad. While the display of the previous menu is initiated when a B is entered on the keypad. Following the execution of a particular keypad command, the previous main menu displayed is

always entered.

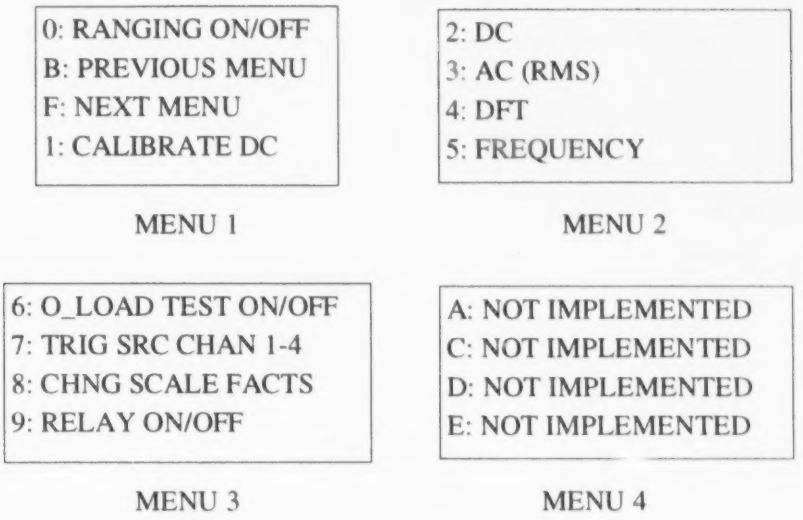

Figure 5.3 Detailed menu displays

Following the execution of the main menu, the program reads the input key_buffer, testing for the presence or absence of each valid key input. On the detection of a valid key input, program execution is transferred to the appropriate module. Provision has been made in each module for exiting that module if a key input is detected during execution. On entry into each module, a byte-wide memory location which reflects the input key (key_buffer) is initialized to a value of FF_{16}. A value different from FF_{16} when the key_buffer location is polled, indicates that a user key input was processed by the key input interrupt service routine.

5.2.2 Module 0

The flow diagram of this module is shown in Figure 5.4. This module is executed when a '0' is entered by the user following a display of "MENU 1". This module toggles the autoranging state. Autoranging enables the selection of the most appropriate gain values for each channel. This action is performed by the source code indicated by the 'C' routine range(register unsigned short countval). This routine is executed following an acquisition cycle and transfers program execution to the acquisition of a new sample set on exit, if a change in any of the channel gains was performed. The judicious use of this routine is thus required, since a quickly changing signal amplitude can prevent the program from exiting the ranging-acquisition cycle. With auto-ranging disabled, subsequent data acquisition cycles use the previous gains

set by the software. By default on power-up, the gain setting ICs are set up for a gain of 1 (the minimum gain possible).

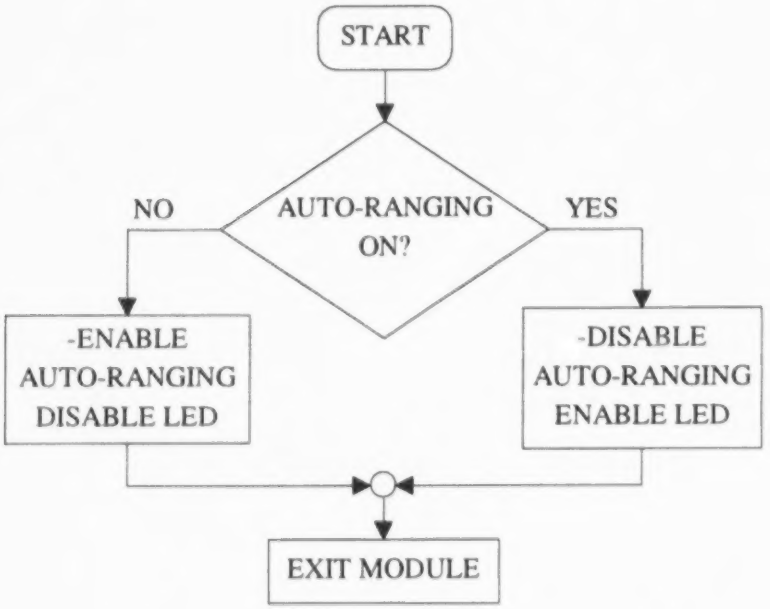

Figure 5.4 Flowchart of Module '0'

5.2.3 Module 1

The flow diagram of this module is shown in Figure 5.5. This module is executed when a '1' is entered. The calibration routine should be executed with the inputs grounded. The purpose of this routine is to set up the hex value corresponding to a zero on the input terminals of the meter thus minimizing device tolerance which could cause a drift from the 800_{16} output ADC value for an ADC analog input of zero. The average hex value of the 1024 samples obtained for each channel are stored as the new system offsets for differentiating positive and negative values obtained from the ADCs.

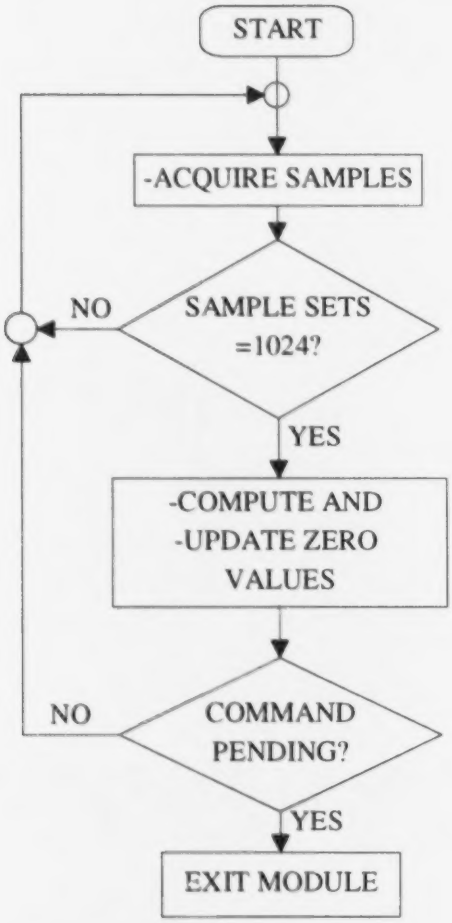

Figure 5.5 Flowchart of Module 1

5.2.4 Module 2

The flow diagram of this module is shown in Figure 5.6. This module is executed when a '2' is entered. This module computes the voltage, current and power for DC signals. On entry, the submenu shown below is displayed. Program execution loops until one of the appropriate inputs (1,2 or 3) is entered, thus enabling the appropriate measurement mode.

ENTER:
1 FOR PHASE 1
2 FOR PHASE 2
3 FOR 3-PHASE

The parameters computed and displayed in the 'Phase 1' selection mode are the average value of the voltage signal on channel 1, the average value of the current signal on channel 2 and the active power using the product of the channel 1 voltage samples and the channel 2 current samples. These show up on the display lines 2, 3 and 4 as V1, I1 and W1 respectively. Similarly, the 'Phase 2' selection uses the voltage signal on channel 3 and the current signal on channel 4. The corresponding parameters are displayed as V2, I2 and W2. The '3-PHASE' selection displays the active power W1 and W2. In each case, the word 'DC' is displayed in the centre of line 1 of the display.

The routine dc_mode() is used and the necessary semaphores are enabled to ensure selection of the appropriate sampling and computation routines depending on the selection mode entered in the sub-menu. The end-correction is of course not used in this mode. A total of 1024 sample sets are obtained, averaged, and multiplied by the appropriate scale factors to obtain the required parameters (voltage, current or power) depending on the phase selection made. In the Phase 1 and Phase 2 modes, the DC voltage, current and active power are computed and displayed for inputs on the first pair (V1 and I1) and second pair of terminals (V2 and I2) respectively. And in the 3 phase mode, only the power in each phase is computed and displayed based on the inputs on the first pair and second pair of input terminals.

The formula shown below is used for the computations. The DC voltage or DC current are computed using integer arithmetic as coded in 'C' routine eval1(register short *first), and the DC power as coded in the 'C' routine eval3(register int cnt, register short *first, register short *second).

$$DC(y_j) = \frac{1}{N} \cdot \sum_{j=0}^{N-1} y_j$$

y_i= (Voltage sample) x (Corresponding current sample) for power computations.
else
y_i= (Voltage sample) or (Current sample)

The final result is multiplied by the appropriate scale factor (depending on the channel gains) implemented in 'C' routine units1(..) for the DC voltages and currents, and for DC power values, the 'C' routine units2(..) is used. The scale factors used for the DC ,

AC and the DFT results display are expressed as:

$$\frac{N}{2^D}$$

The value N being stored as the numerator value, and D stored as the denominator value. This mode of storage enables division to be performed by simply shifting a binary value D places to the right.

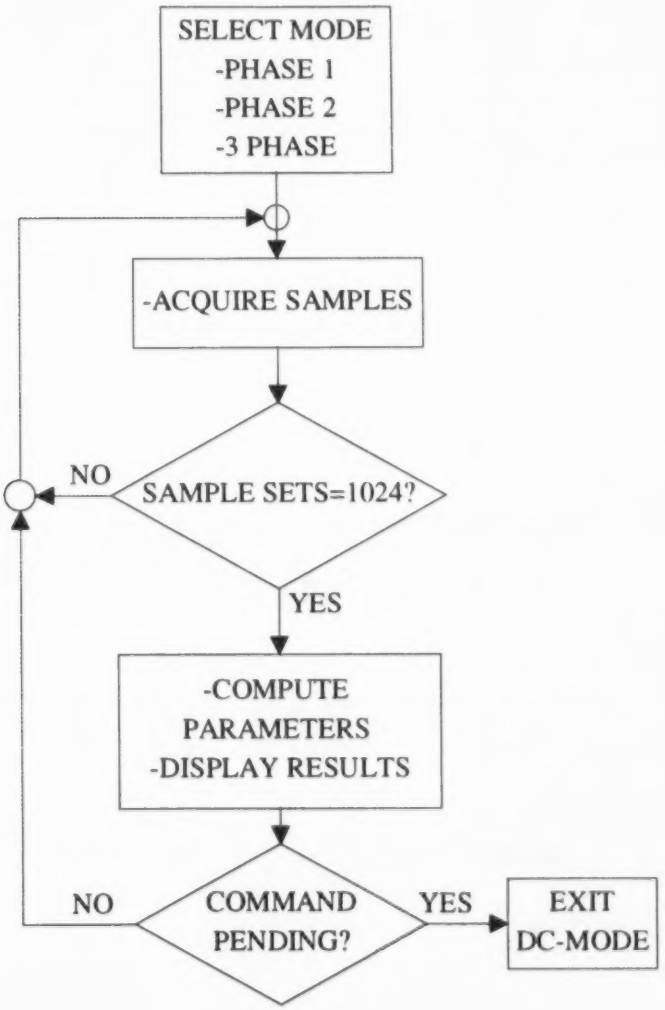

Figure 5.6 Flowchart of module 2

5.2.5 Module 3

The flow diagram of this module shown in Figure 5.7 is executed when a '3' is entered.

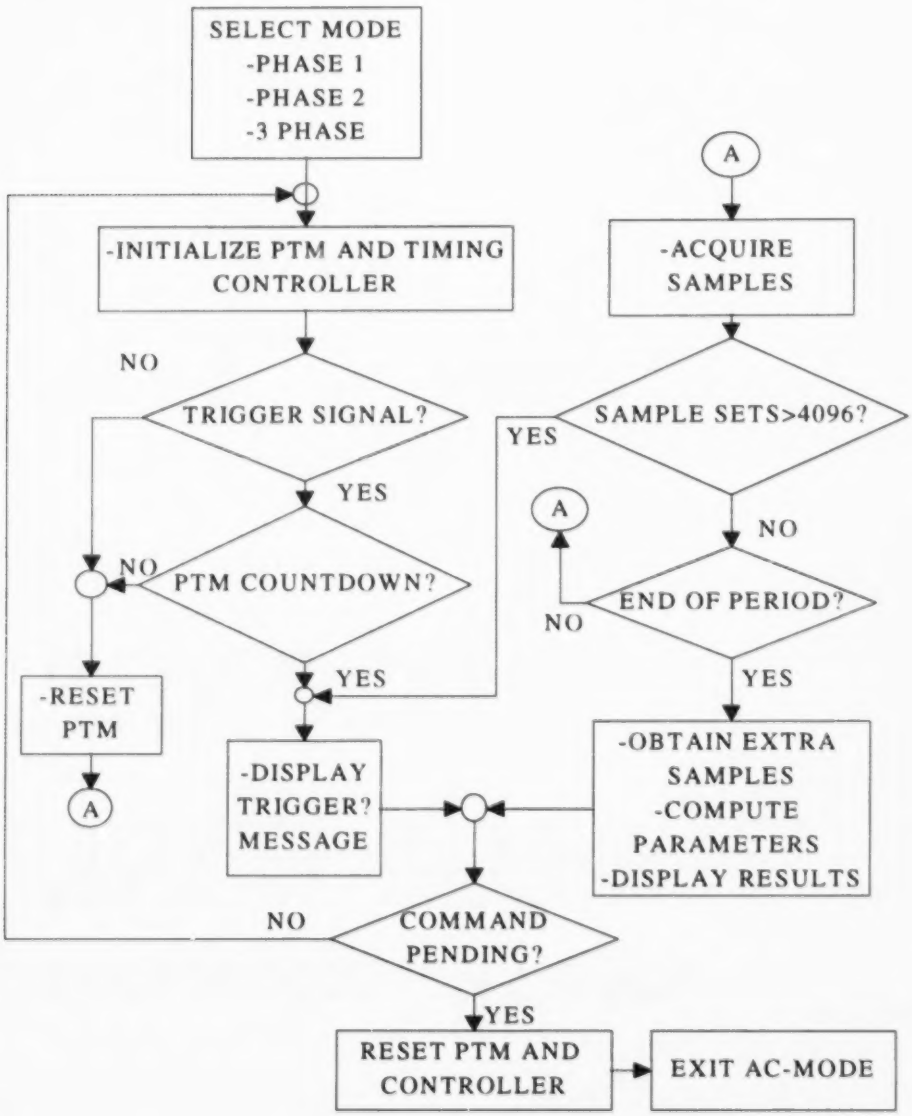

Figure 5.7 Flowchart of module 3

This module computes the RMS voltage, current and power for AC signals.

On entry, the submenu shown below is displayed. Program execution loops until one of the appropriate inputs (1,2 or 3) is entered, thus enabling the appropriate measurement mode.

ENTER:
1 FOR PHASE 1
2 FOR PHASE 2
3 FOR 3-PHASE

The parameters computed and displayed in the 'Phase 1' selection mode are the RMS of the voltage signal on channel 1, the RMS of the current signal on channel 2 and the active power using the product of the channel 1 voltage samples and the channel 2 current samples. These show up on the display lines 2, 3 and 4 as V1, I1 and W1 respectively. Similarly, the 'Phase 2' selection uses the voltage signal on channel 3 and the current signal on channel 4. The corresponding parameters are displayed as V2, I2 and W2. The '3-PHASE' selection displays the active power W1 and W2 as explained above, on lines 2 and 3. In each case, the word 'AC' is displayed in the centre of line 1 of the display.

The TCW is used in all the computations. The routine ac_mode() is used and the necessary semaphores are enabled to ensure selection of the appropriate sampling and computation routines. The PTM is employed as a countdown timer by connecting the output of timer 2 to the input of timer 1. Timer 2 has a count value of $FFFF_{16}$, while timer 1, which generates the interrupt, has a count value of 10. With the 800kHz clock, the countdown time, which causes a trigger to occur, is about 0.8secs. If a start of trigger pulse does not occur within this time, as monitored by the software, or more than 4096 sample sets are acquired, the program indicates a "TRIGGER ?" message and reinitializes the PTM waiting for a trigger. After the signal acquisition, 16 times the end correction for the TCW (Δ) is read from the upper 4 bits of memory address tim_latch (the EP310 IC output). In addition the number of samples acquired is displayed in a hex format in the top left corner of the display.

The mean product (MP) values of the required parameters are computed depending on the selected mode, using the following formula. The formula is implemented by the 'C' function eval2(register int cnt, register short *first, register short *second).

$$MP(y_j) = \frac{1}{16 \cdot N + 16 \cdot \Delta}\left[\left(16 \cdot \sum_{j=1}^{N-1} y_j\right) + 0.5 \cdot (16 + 16 \cdot \Delta) \cdot (y_0 + y_N)\right]$$

y_i= (short *first) x (short *second) as indicated table 5.2 below.

TABLE 5.2 Parameters of 'C' function eval2()

Mode	register short *first	register short *second
Phase 1	Voltage	Same voltage value
Phase 2	Current	Same current value
3-phase	Voltage	Corresponding vurrent value

The summation term in the above formula had to be implemented in floating point arithmetic which reduces the computational speed of the instrument. For the RMS computations, the square-root of the mean product value obtained as per the above-equation is computed. The square-root algorithm ('C' function sqrt1(register int arg)) is based on the sum-of-prime-numbers approach to computing the square-root of integral values. The final result is multiplied by the appropriate scale factor (depending on the channel gains) implemented in 'C' routine units1(..) for RMS voltages and currents, and the mean product is scaled appropriately for AC power values in the 'C' routine units2(..).

5.2.6 Module 4

The flow diagram of this module is shown in Figure 5.8. This module is executed when a '4' is entered. This module computes the DFT (harmonic components) of the voltage, current and power signals using the TCW. On entry, the submenu shown below is displayed. Program execution loops until one of the appropriate inputs (1,2 or 3) is entered, thus enabling the appropriate measurement mode.

ENTER:
1 FOR PHASE 1
2 FOR PHASE 2
3 FOR 3-PHASE

The parameters computed and displayed in the 'Phase 1' selection mode are the harmonic components of the voltage signal on channel 1, the harmonic components of the current signal on channel 2 and the harmonic components of the power signal obtained using the product of the channel 1 voltage samples and the channel 2 current samples. These show up on the display as V1, I1 and W1 respectively with the corresponding harmonic being displayed in the centre of the first line on the display. Similarly, the 'Phase 2' selection uses the voltage signal on channel 3 and the current signal on channel 4. The corresponding parameters are displayed as V2, I2 and W2. The '3-PHASE' selection displays the active power W1 and W2 as explained above as well as the harmonic number.

The routine ac_mode() is used and the necessary semaphores are enabled to ensure selection of the appropriate sampling and computation routines. The signal acquisition procedure is identical to that employed in the AC-mode. The computation of the harmonic components however employ a single-precision floating-point representations based on a DFT using the TCW is employed. The code implemented in 'C' routine dft1(register unsigned short cnt, register short *first) determines the DFT of the voltage or current signal in the selected mode. 'C' routine dft(register unsigned short cnt, register short *first, register short *second) is the corresponding power signal harmonic computation routine.

The formula used is:

$$X(k)=\frac{1}{N+\Delta}[\sum_{i=1}^{N-1} y_i e^{-jik\phi}+(\frac{1+\Delta}{2})\cdot(y_N e^{-jNk\phi}+y_0 e^{-j0k\phi})]$$

where $\phi=2\pi/(N+\Delta)$
and the y_i values are as indicated in Table 5.3

TABLE 5.3 Value of y_i used in the various modes.

Mode	y_i
Phase 1	Voltage
Phase 2	Current
3-phase	Product of corresponding Voltage and current

The trigonometric values $e^{-jik\phi}$ are computed using the routine trig(unsigned short cnt, unsigned short k). The index i is passed through the variable 'cnt'. In this routine, the computation of the sine and cosine values is based on a table of 1024 single-precision floating point values for angles between 0 and $\pi/2$ radians. Basically, the product $ik\phi$ is reduced to a value between 0 and $\pi/2$ radians. The cosine and sine values are then read from the lookup table.

The routines inherently, produce the results in the real-imag form. If the magnitude-phase option was selected, the magnitude of the result of the above equation is computed as the square-root of the sum of the squares of the real and imaginary components. The arctan function is used to determine the phase.

The final result is multiplied by the appropriate scale factor (depending on the channel gains) implemented in 'C' routine units2b(..) for voltages and currents, and the 'C' routine units2(..) for the power signal harmonic values.

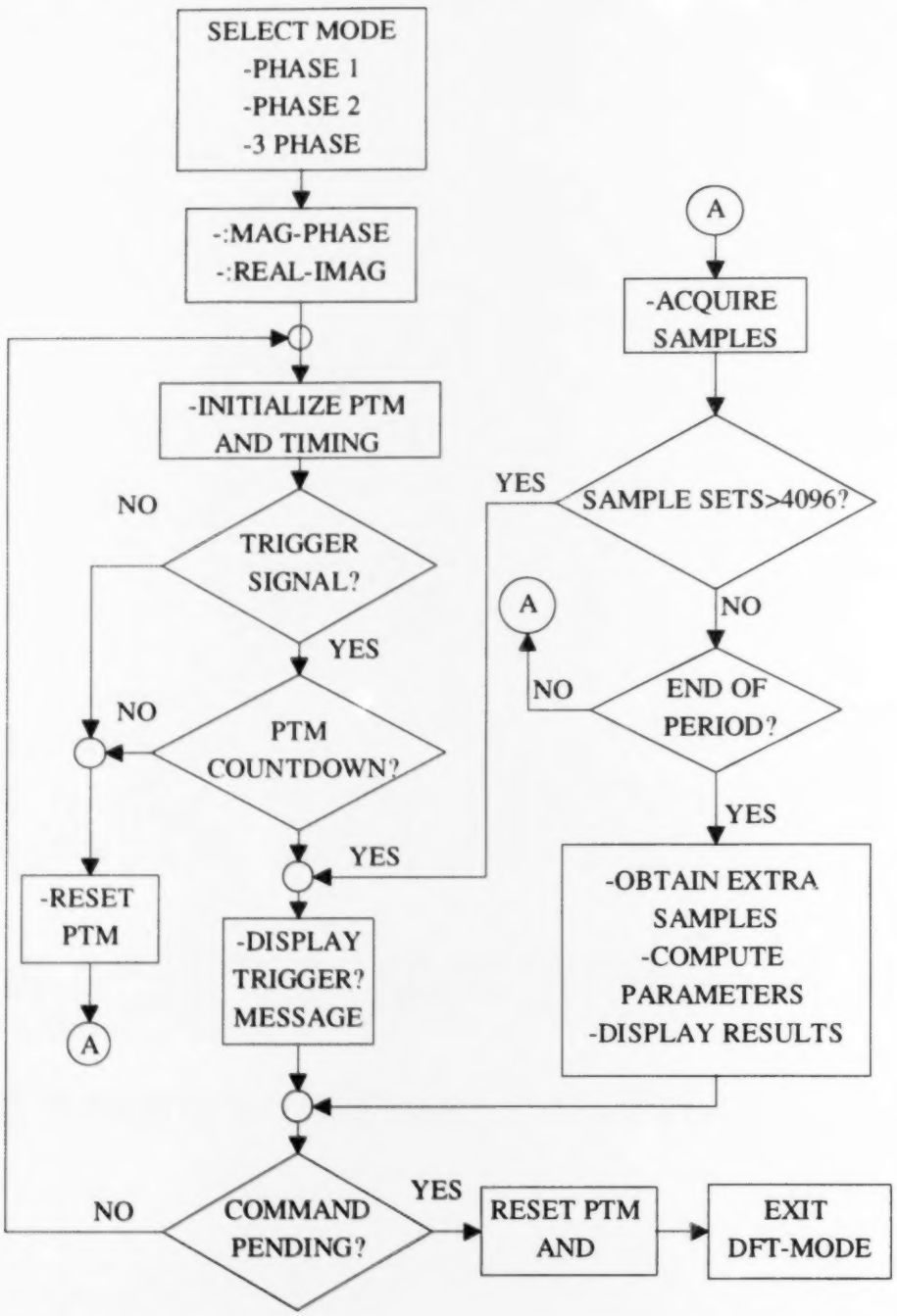

Figure 5.8 Flowchart of module 4

5.2.7 Module 5

The flow diagram of this module is shown in Figure 5.9. This module is executed when a '5' is entered. This module computes and displays the frequency of the trigger signal using timer 3 of the 6840 PTM IC. In addition, the minimum and maximum frequencies are also displayed.

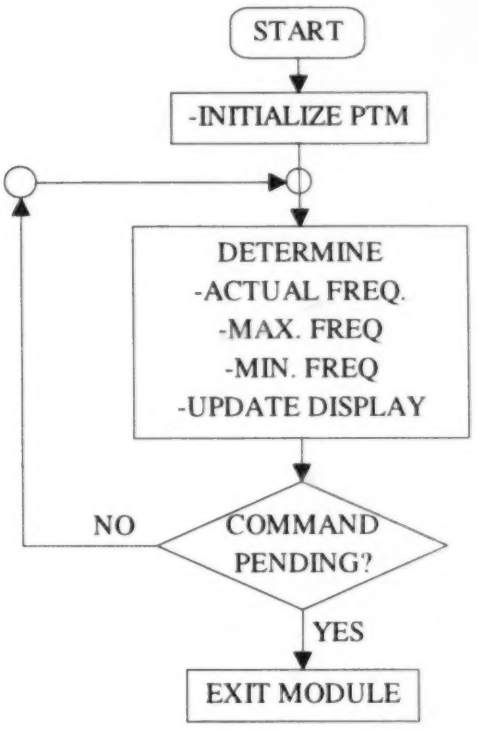

Figure 5.9 Flowchart of Module 5

5.2.8 Module 6

The flow diagram of this module is shown in Figure 5.10. This module is executed when a '6' is entered. It's purpose is to toggle the status of the overload test (enable or disable overload testing).

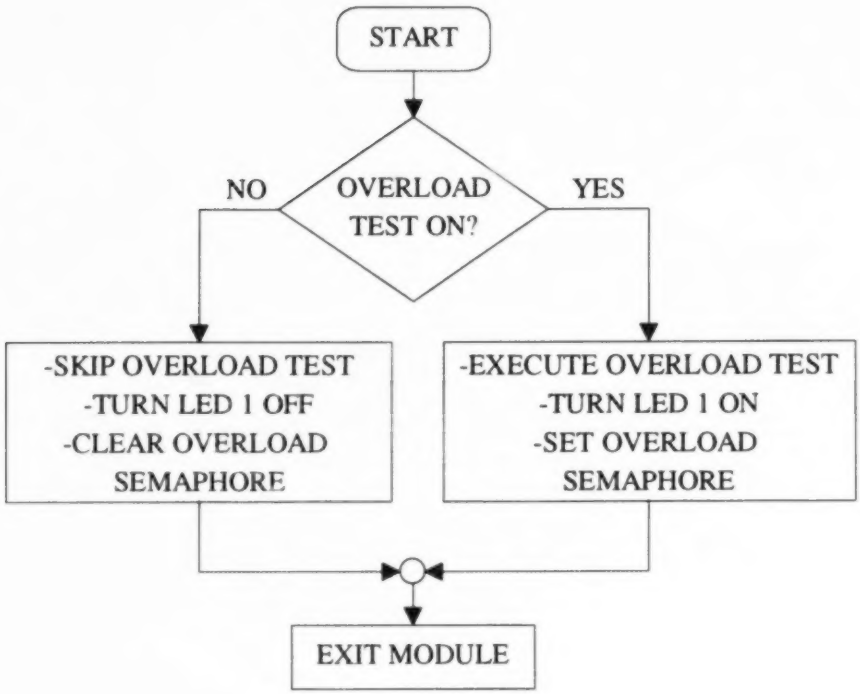

Figure 5.10 Flowchart of module 6

5.2.9 Module 7

The flow diagram of this module is shown in Figure 5.11. This module is executed when a '7' is entered. On entering this module, a sub-menu is presented which enables the user select the appropriate channel to set up as the trigger source. The user input results in the selection of the appropriate PIA outputs which enable the required trigger channel as explained in the EPLD MODULE in the hardware description section. By default, following the system power-up, channel 1 is used as the system trigger source.

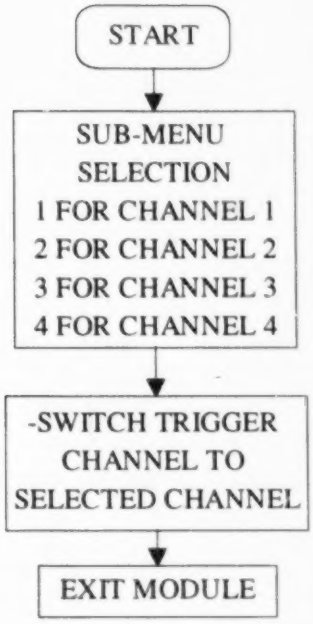

Figure 5.11 Flowchart of module 7

5.2.10 Module 8

The flow diagram of this module is shown in Figure 5.12. This module is executed when a '8' is entered. The purpose of this routine is to increase or decrease the scale factors (numerator and denominator) for each channel. On entering this module, a sub-menu is presented, which enables the user select the appropriate channel to set up as the trigger source. The actual value changes are performed in subroutine sc_fact(..), where the 'f' key increases the value while 'b' decreases it. The module is exited when a 'c' is entered. This routine is entered twice for each channel selection. The first time is for changing the numerator value N and the second time for the denominator value D . As previously noted, the scale factor is expressed as:

$$\frac{N}{2^D}.$$

Subroutine sc_fact(..) can be expressed in pseudo-code as:

```
do{
        switch(key_input)
        {
        case 'f':
                increment value;
                break;
        case 'b':
                decrement value;
                break;
        default:
                break;
        }
}while (key_input != 'c')
```

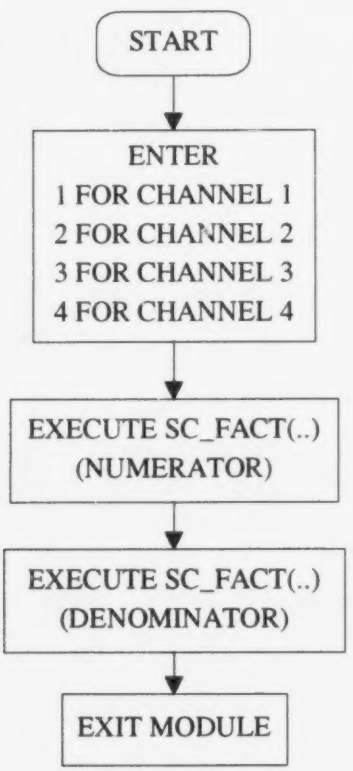

Figure 5.12 Flowchart of module 8

5.2.11 Module 9

The flow diagram of this module is shown in Figure 5.13. This module is executed when a '9' is entered. The purpose of this routine is to toggle the state of the input relays to disconnect the input terminals from the rest of the system, or connect the input terminals to the rest of the system.

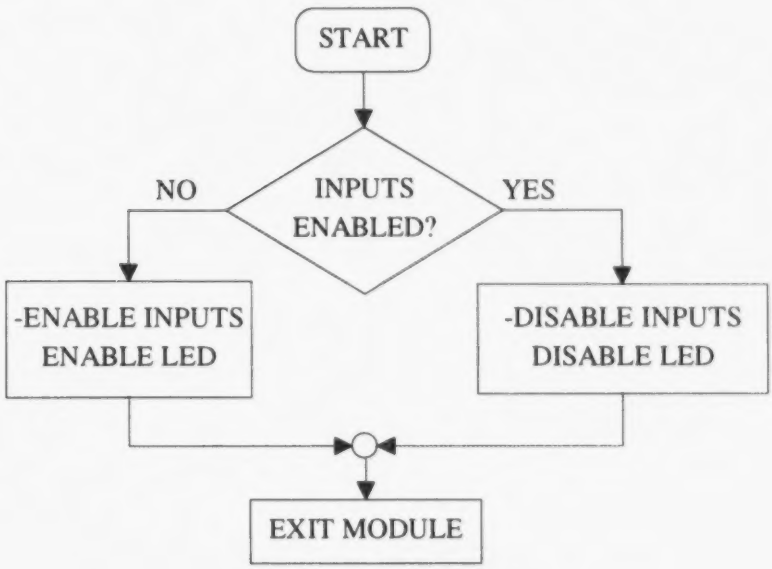

Figure 5.13 Flowchart of module 9

5.2.12 Module 10

This module is executed when an 'A' is entered. This key has not been assigned to any function. Thus, this module simply results in the display of the message: "NOT IMPLEMENTED".

5.2.13 Module 11

This module is executed when a 'B' is entered. The purpose of this routine is to cause the previous menu to be displayed. The effect of this key entry on the menus is depicted in Figure 5.14.

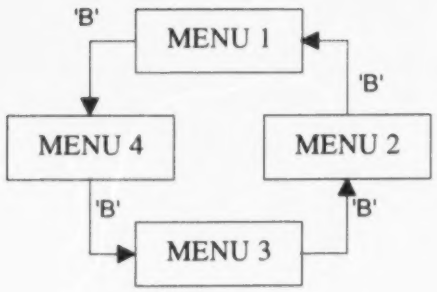

Figure 5.14 Flowchart of module 11

5.2.14 Module 12

This module is executed when a 'C' is entered. This key has not been assigned to any function. Thus, this module simply results in the display of the message: "NOT IMPLEMENTED".

5.2.15 Module 13

This module is executed when a 'D' is entered. This key has not been assigned to any function. Thus, this module simply results in the display of the message: "NOT IMPLEMENTED".

5.2.16 Module 14

This module is executed when an 'E' is entered. This key has not been assigned to any function. Thus, this module simply results in the display of the message: "NOT IMPLEMENTED".

5.2.17 Module 15

This module is executed when a 'F' is entered. The purpose of this routine is to cause the next menu to be displayed. The effect of this key entry on the menus is depicted in Figure 5.15.

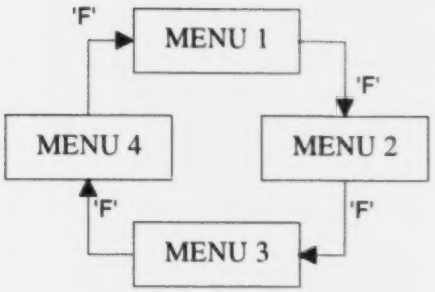

Figure 5.15 Flowchart of module 15

6. ERROR ANALYSIS

To completely analyze any measurement technique as implemented on a particular hardware and software platform, the effects of various error situations are analyzed. The factors which can contribute to the error in the measured amplitude and phase values are analyzed in order to determine the predominant error sources.

The major contributions to measurement accuracy aside from theoretical limitations are likely those due to; ADC quantization, sampling jitter, numerical errors in the DFT algorithm employed, the system hardware component tolerance effects. The means and variances of the computed signal magnitudes and phases as a result of the ADC quantization and sampling jitter effects will be evaluated for $k\phi << 1$ (i.e. $k << N$). The condition is easily met in practise. In addition, an analysis of the sensitivity of the DFT algorithm to numerical errors will be performed. This will be followed by an approximate analysis of the analog signal error due to the system hardware components in the voltage and current channels and finally the error due to determining Δ to a finite precision.

6.1 ADC quantization errors [19]

The quantization step δ of a signal having a dynamic range of 2D (peak-to-peak) applied to an ideal k-bit ADC of range 2D is:

$$\delta = \frac{2D}{2^k} = 2^{-(k-1)} D \tag{6.1.1}$$

For a 12-bit ADC as used and D=2.5V, $\delta = 1.22 \cdot 10^{-3}$

The ADC output $x_q(i)$ for the ith sample is:

$$x_q(i) = x(i) + e(i) \tag{6.1.2}$$

where e(i) is the *ith* quantization error.

For most practical cases, the statistical representation of the quantization error 'e' is based on the following assumptions, resulting in the pictorial probability density function in Figure 6.1:

1. The error sequence e(i) is a sample sequence of a stationary random process.
2. The error sequence is uncorrelated with the signal sequence (x_i).
3. The random variables of the error process are uncorrelated; i.e. the error is a white-noise process.
4. The probability density of the error process is uniform over the range of quantization error.

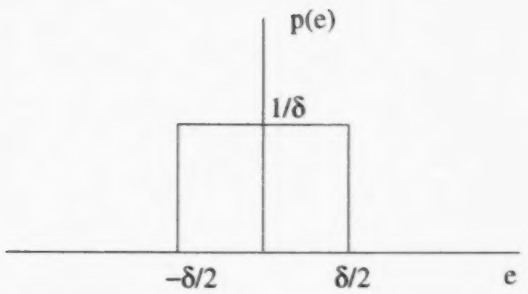

Figure 6.1 Probability density function of quantization error

The quantization error 'e' thus has a mean value given by:

$$\hat{e} = \int_{-\infty}^{\infty} e.p(e)de = 0 \qquad (6.1.3)$$

and variance

$$\begin{aligned}\sigma_e^{\,2} &= \int_{-\infty}^{\infty} (e-\hat{e})^2 p(e)de \\ &= \int_{-\infty}^{\infty} e^2 p(e)de \\ &= \frac{1}{\delta}\int_{-\delta/2}^{\delta/2} e^2 de \\ &= \frac{\delta^2}{12}\end{aligned} \qquad (6.1.4)$$

For a 12-bit ADC as used

$$\sigma_e^{\,2} = 1.2417 \cdot 10^{-7}$$

The time-domain signal in Equation 2.1.2 can be expressed as:

$$\begin{aligned} x_c(t) &= C_0 + \sum_{k=1}^{M} C_k \cos(\frac{2\pi k}{T} t - \theta_k) \\ &= C_0 + \sum_{k=1}^{M} C_k \cos\theta_k . \cos(\frac{2\pi k}{T} t) + C_k \sin\theta_k . \sin(\frac{2\pi k}{T} t) \\ &= C_0 + \sum_{k=1}^{M} A_k . \cos(\frac{2\pi k}{T} t) - B_k . \sin(\frac{2\pi k}{T} t) \end{aligned} \qquad (6.1.5)$$

Using the results in Reference [19], the DFT is applied to the sampled values windowed with the TCW.

Let $\mathbf{X1_k}$ and $\mathbf{X2_k}$, be random variables given by

$$\begin{aligned} X1_k &= \frac{2}{N+\Delta} \Theta_i \left[e(i) \cos\left(\frac{2\pi k i}{N+\Delta} \right) \right] \\ X2_k &= \frac{2}{N+\Delta} \Theta_i \left[e(i) \sin\left(\frac{2\pi k i}{N+\Delta} \right) \right] \end{aligned} \qquad (6.1.6)$$

Where $\mathbf{\Theta_i}$ is a summation operator based on the TCW, applied to samples of index *i*.

The computed values of the harmonic amplitudes and phases, C_{kc} and θ_{kc}, of the time-domain signal components can thus be expressed as:

$$\begin{aligned} C_{kc} &= \sqrt{(A_k + X1_k)^2 + (B_k - X2_k)^2} \\ \theta_{kc} &= -\tan^{-1}\left(\frac{B_k - X2_k}{A_k + X1_k} \right) \end{aligned} \qquad (6.1.7)$$

The parameters C_{kc} and θ_{kc}, are functions of two random variables $X1_k$ and $X2_k$. To determine the means and variances of C_{kc} and θ_{kc}, the approach in Reference [19] will be used. This entails computing the expected value and variance of $X1_k$ and $X2_k$.

$$\begin{aligned} E(X1_k) &= \frac{2}{N+\Delta} E\{ \Theta_i \left[e(i) \cos\left(\frac{2\pi k i}{N+\Delta} \right) \right] \} \\ &= 0 \end{aligned} \qquad (6.1.8)$$

In addition,

$$E(X2_k) = \frac{2}{N+\Delta} E\{\Theta_i\left[e(i)\sin\left(\frac{2\pi ki}{N+\Delta}\right)\right]\}$$
$$= 0 \qquad (6.1.9)$$

The expected value of the product $X1_k * X2_k$ will be computed in order to determine the correlation between the two random variables.

$$E(X1_k \cdot X2_k) = \frac{4}{(N+\Delta)^2} \cdot E[\Theta_{l,l\neq m}\Theta_m\{e(l).e(m)\cos\frac{2\pi kl}{N+\Delta}\sin\frac{2\pi km}{N+\Delta}\}$$
$$+\Theta_h\{e^2(h).\cos\frac{2\pi kh}{N+\Delta}.\sin\frac{2\pi kh}{N+\Delta}\}] \qquad (6.1.10)$$

From Reference [19], since $e(l)$ and $e(m)$ are uncorrelated for $l \neq m$, the first term is zero. In addition, $E[e^2(h)] = \sigma_e^2$. Hence after interchanging the expectation and summation operations Equation 6.2.10 simplifies to

$$E(X1_k \cdot X2_k) = \frac{2.\sigma_e^2}{(N+\Delta)^2} \cdot \Theta_h\{\sin\frac{4\pi kh}{N+\Delta}\} \qquad (6.1.11)$$

The result of evaluating Equation 6.1.1 depends on the windowing function employed. The results from references [10] and [11] indicate that for $k\phi << 1$,

$$\Theta_h\{\sin\frac{4\pi kh}{N+\Delta}\} \approx \frac{\Delta^2}{24}(2k\phi)^3 \cdot (\Delta^2 - 1)$$
$$= \frac{\Delta^2}{3}(k\phi)^3 \cdot (\Delta^2 - 1)$$
$$\approx 0$$

This indicates that $X1_k$ and $X2_k$ can be considered uncorrelated. The variance in the real part of the DFT of the error signal is thus:

$$(\sigma_{X1_k})^2 = E[(X1_k)^2]$$
$$= \frac{4.\sigma_e^2}{(N+\Delta)^2} \cdot \Theta_i\left[\cos^2\left(\frac{2\pi ki}{N+\Delta}\right)\right]$$
$$= \frac{2.\sigma_e^2}{(N+\Delta)^2} \cdot \Theta_i\left[1+\cos\left(\frac{4\pi ki}{N+\Delta}\right)\right] \qquad (6.1.12)$$

Again the results from References [10] and [11] indicate that for $k\phi << 1$, the second term

$$\Theta_h\{\cos\frac{4\pi kh}{N+\Delta}\} \approx \frac{\Delta}{12}.(2k\phi)^2 \cdot (1-\Delta^2)$$
$$= \frac{\Delta}{3}.(k\phi)^2 \cdot (1-\Delta^2)$$
$$\approx 0$$

Hence Equation 6.1.12 can be approximated as.

$$(\sigma_{X1_k})^2 \approx \frac{2.\sigma_e^{\,2}}{N+\Delta}$$
$$= \frac{\delta^2}{6.(N+\Delta)}$$
$$\approx \frac{\delta^2}{6.N} \qquad (6.1.13)$$

Similarly, it can be shown that

$$(\sigma_{X2_k})^2 = \frac{2.\sigma_e^{\,2}}{N+\Delta}$$
$$= \frac{\delta^2}{6.(N+\Delta)}$$
$$\approx \frac{\delta^2}{6.N} \qquad (6.1.14)$$

If we let

$$\sigma_{X_k}^{\,2} = (\sigma_{X1_k})^2 = (\sigma_{X2_k})^2 \qquad (6.1.15)$$

As an example for N=512 and using the value of δ from Equation 6.1.1.

$$\sigma_{X_k}^{\,2} \approx 2.9 \cdot 10^{-9}$$

6.1.1 Amplitude Measurement

The quantization-free amplitude and phase expressions are:

$$C_k = \sqrt{(A_k)^2 + (B_k)^2}$$

$$\theta_k = -\tan^{-1}\left(\frac{B_k}{A_k}\right) \tag{6.1.16}$$

Using a second-order Taylor's series representation (i.e retaining only the linear terms) for a function of two random variables, the expected value of the amplitude expression in Equation 6.2.7 is:

$$E[C_{kc}] \approx [C_{kc} + \frac{1}{2}(\sigma_{X1_k}{}^2 \frac{\partial^2 C_{kc}}{\partial X1_k{}^2} + \sigma_{X2_k}{}^2 \frac{\partial^2 C_{kc}}{\partial X2_k{}^2})]\Big|_{X1_k, X2_k=0}$$

$$= C_k + \frac{\sigma_{X_k}{}^2}{2}(\frac{1}{C_k} - \frac{1}{C_k}(\frac{A_k}{C_k})^2 + \frac{1}{C_k} - \frac{1}{C_k}(\frac{B_k}{C_k})^2)$$

$$= C_k + \frac{\sigma_{X_k}{}^2}{2C_k}$$

$$= C_k + \frac{\delta^2}{12.N.C_k} \tag{6.1.17}$$

The variance $\sigma_{C_{kc}}{}^2$ can be expressed as:

$$\sigma_{C_{kc}}{}^2 = E[(C_{kc})^2] - [E(C_{kc})]^2 \tag{6.1.18}$$

Now:

$$E[(C_{kc})^2] = [C_k]^2 + 2.\sigma_{X_k}{}^2$$

Substituting the above and Equation 6.1.17 into Equation 6.1.18 results in:

$$\sigma_{C_{kc}}{}^2 \approx \sigma_{X_k}{}^2 - \frac{\sigma_{X_k}{}^4}{4(C_k)^2}$$

$$\approx \sigma_{X_k}{}^2 \tag{6.1.19}$$

Thus:

$$\sigma_{C_k} \approx \frac{\delta}{\sqrt{6.N}} \tag{6.1.20}$$

Again for N=512 and using the value of δ from Equation 6.1.1 results in:

$$\sigma_{C_k} \approx 2.2 \cdot 10^{-5}$$

6.1.2 Phase Measurement

Using a Taylor's series representation for a function of two random variables and retaining only the linear terms, the expected value of the phase expression in Equation 6.2.7 is:

$$E[\theta_{kc}] \approx [\theta_{kc} + \frac{1}{2}(\sigma_{X1_k}{}^2 \frac{\partial^2 \theta_{kc}}{\partial X1_k{}^2} + \sigma_{X2_k}{}^2 \frac{\partial^2 \theta_{kc}}{\partial X2_k{}^2})]\Big|_{X1_k \cdot X2_k = 0}$$

$$= \theta_k + \frac{\sigma_{X1_k}{}^2}{2}\left(\frac{-2A_k B_k}{(A_k{}^2 + B_k{}^2)^2} + \frac{2A_k B_k}{(A_k{}^2 + B_k{}^2)^2}\right)$$

$$= \theta_k \tag{6.1.21}$$

From Reference [19]

$$\sigma_{\theta_{kc}}{}^2 = \frac{\sigma_{X_k}{}^2}{C_k{}^2}$$

Thus

$$\sigma_{\theta_{kc}} = \frac{\sigma_{X_k}}{C_k} = \frac{\delta}{C_k\sqrt{6.N}} \tag{6.1.22}$$

As an example with N=512, C_k=2.5 and using the value of δ previously calculated in Section 6.1 results in

$$\sigma_{\theta_{kc}} = \frac{2.2 \cdot 10^{-5}}{2.5} = 8.8 \cdot 10^{-6}$$

6.1.3 DC Component Measurement

The computed DC component, C_{0c} is:

$$C_{0c} = \frac{1}{N+\Delta}\Theta_i\left[x_q(i)\right]$$
$$= \frac{1}{N+\Delta}\Theta_i\left[x(i)+e(i)\right] \qquad (6.1.23)$$

With expected value:

$$E(C_{0c}) = \frac{1}{N+\Delta}\Theta_i[x(i)]$$

and variance

$$\sigma_{C_{0c}}^{2} = E\{\left[(C_{0c}) - E(C_{0c})\right]^2\}$$
$$= \frac{1}{(N+\Delta)^2}E\{\left[\Theta_i(e(i))\right]^2\}$$
$$\approx \frac{\sigma_e^2}{N} \qquad (6.1.24)$$

As an example, with N=512 and using the value of δ from Section 6.1 results in:

$$\sigma_{C_{0c}} \approx 1.55 \cdot 10^{-5}$$

6.2 Effect of sample jitter [20]

Sampling jitter effects on the harmonic components amplitude and phase determined by the algorithm employed can be analyzed based on the procedure in reference [20] for $k\phi << 1$. The effect of sampling jitter is expressed as a voltage change and the computation is as follows.

Considering a time-domain sinusoidal given by:

$$V(t) = C\cos(\Omega t - \theta)$$
$$= C\cos\theta.\cos\Omega t + C\sin\theta.\sin\Omega t \qquad (6.2.1)$$

The sampled version of this signal can be expressed as:

$$V(i) = C\cos\left[\Omega(iT_s + \tau) - \theta\right] \qquad (6.2.2)$$

where the sampling jitter, τ , is a random variable with properties similar to the quantization error 'e' in the previous section. In a sampled data system, the aperture delay time of the sample-and-hold amplifier forms the primary contribution to τ.

Differentiating Equation 6.2.1 results in:

$$dV(t) = -C\Omega \sin(\Omega t - \theta)dt \tag{6.2.3}$$

where *dt* is the sampling jitter τ , which is assumed to be much smaller than the sampling interval T. This is a valid assumption for the system which has 32μs sampling interval, and an aperture delay jitter in the nano-second range.,

For the *ith* sample, denoting (ΩiT_S-θ) by $\gamma(i)$ and the jitter by τ(i).
Equation 6.3.2 can be rewritten as:

$$dV(i) = -C\Omega.\tau(i)\sin\gamma(i) \tag{6.2.4}$$

The DFT (for harmonic components $1 \leq k \leq N-1$) is applied to the sampled values (index i) windowed with the TCW.

Let:

$$A = C\cos\theta$$
$$B = -C\sin\theta$$

and $\mathbf{X_1}$ and $\mathbf{X_2}$, random variables given by

$$X_1 = \frac{2}{N+\Delta}\Theta_i\left[(-C.\Omega.\tau(i)\sin\gamma(i))\cos\left(\frac{2\pi i}{N+\Delta}\right)\right]$$
$$X_2 = \frac{2}{N+\Delta}\Theta_i\left[(-C.\Omega.\tau(i)\sin\gamma(i))\sin\left(\frac{2\pi i}{N+\Delta}\right)\right] \tag{6.2.5}$$

Where $\mathbf{\Theta_i}$ is a summation operator based on the TCW, applied to samples of index *i*.

The computed values of the harmonic amplitudes and phases, C_c and θ_c, of the time-domain signal components can thus be expressed as:

$$C_c = \sqrt{(A+X_1)^2 + (B-X_2)^2}$$
$$\theta_c = -\tan^{-1}\left(\frac{B-X_2}{A+X_1}\right) \tag{6.2.6}$$

Applying a similar procedure to that used in section 6.1, results in the following as obtained from reference [20].

$$E[C_C] \approx C\left[1+\frac{\sigma_R^{\,2}}{2.N}\right] \tag{6.2.7}$$

and the variance by

$$\sigma_{C_C}^{\,2} \approx \frac{(C\sigma_R)^2}{N} \tag{6.2.8}$$

Where σ_R is the variance of the product $\Omega\tau(i)$ (i.e. the sampling jitter expressed as a phase jitter).

For the phase measurement,

$$E[\theta_c] \approx \theta \tag{6.2.9}$$

and

$$\sigma_{\theta_c}^{\,2} \approx \frac{\sigma_R^{\,2}}{N} \tag{6.2.10}$$

6.3 Extension to signals derived from product of two sampled signals

Power signal harmonics are computed from a product of sampled voltage and current signals.

Let the sampled values of voltage and current be: $V_S(i)$ and $I_S(i)$ respectively and the true values, V(i) and I(i). The corresponding quantization errors of the voltage and current signal being $e_v(i)$ and $e_i(i)$ respectively.

The true power at the harmonic is:

$$P(i) = P_s(i) + e_t(i)$$

$$\begin{aligned} V(i).I(i) &= (V_s(i)+e_v(i)).(I_s(i)+e_i(i)) \\ &= V_s(i)\,I_s(i)+[V_s(i)\,e_i(i)+I_s(i)\,e_v(i)]+e_v(i)\,e_i(i) \\ &= V_s(i)\,I_s(i)+e_t(i) \end{aligned} \tag{6.3.1}$$

Assuming $e_v(i)$ and $e_i(i)$ are uncorrelated,

$$
\begin{aligned}
E(e_t(i)) &= E[V_s(i).e_i(i) + I_s(i).e_v(i) + e_v(i).e_i(i)] \\
&= E(V_s(i).e_i(i)) + E(I_s(i).e_v(i)) + E(e_v(i).e_i(i)) \\
&= 0
\end{aligned}
\tag{6.3.2}
$$

and

$$
\begin{aligned}
\sigma_t^{\,2} &= E(e_t^{\,2}(i)) \\
&= E\{V_S^{\,2}(i)\, e_i^{\,2}(i) + I_S^{\,2}(i)\, e_V^{\,2}(i)\} \\
&= E\{V_S^{\,2}(i)\, e_i^{\,2}(i)\} + E\{I_S^{\,2}(i)\, e_V^{\,2}(i)\} \\
&= \sigma_e^{\,2} . E\{V_S^{\,2}(i) + I_S^{\,2}(i)\}
\end{aligned}
\tag{6.3.3}
$$

The variance thus depends on the voltage and current sampled values.

This variance can be used in the amplitude and sampling jitter computations in place of $\sigma_e^{\,2}$.

For a single input sinusoid where

$$
\begin{aligned}
V_s(i) &= V_{\max} \cos(i\phi) \\
I_s(i) &= I_{\max} \cos(i\phi - \theta)
\end{aligned}
\tag{6.3.4}
$$

the variance is

$$
\begin{aligned}
\sigma_t^{\,2} &= \sigma_e^{\,2} . E\{V_{\max}^{\,2} . \cos^2(i\phi) + I_{\max}^{\,2} . \cos^2(i\phi - \theta)\} \\
&= \sigma_e^{\,2} . E\{V_{\max}^{\,2} . (\frac{1+\cos(2i\phi)}{2}) + I_{\max}^{\,2} . (\frac{1+\cos(2i\phi - 2\theta)}{2})\} \\
&= \frac{\sigma_e^{\,2}}{2} . (V_{\max}^{\,2} + I_{\max}^{\,2})
\end{aligned}
\tag{6.3.5}
$$

6.4 Numerical Errors in the DFT Algorithm

The ADC employed are 12-bit types with each output value being an 11-bit number and the additional bit representing the sign bit. All the calculations could be done with 32-bit integer arithmetic representations with the final result being rounded to the number of decimal places required for the display. No computational errors due to the use of fixed point arithmetic occurs in these instances.

Computational errors could however occur, due to the use of floating-point representations. This form of numerical representation is used where trigonometric functions are used. A case in point is in the DFT calculation where a 32-bit floating-

point representation was used. A single-precision floating point representation is used, comprising a sign-bit, an 8-bit exponent and 23-bit mantissa. This was because double-precision values increased the computation time by over 50% for each harmonic. The floating point routines minimized computation errors by using double-precision arithmetic for the intermediate products and sums of the inner products of the DFT expression.

The error analyses used are based on the method in Reference [3]. The error model assumed is a linear-one in which the absolute errors are approximated by the first-order terms of the Taylor expansion in local relative errors, and is stochastic in the sense that these local errors are regarded as random variables, independently and identically distributed (i.i.d), for each elementary operation in which they arise.

Floating point numbers $x \in R$ are represented by the elements of a discrete set R_M, which if $x \neq 0$, are of the form

$$\tilde{x} = \pm m.2^{l}$$

Where m, referred to as the mantissa, is a binary number in the range [0.5,1]. l is an integer whose range depends on the floating point representation used.

If x and y are members of R_M, and f is an elementary operation, then the instrument will compute $\hat{f}(x,y)$, which is also in R_M and is such that

$\hat{f}(x,y) = f(x,y)(1+\varepsilon)$

where $|\varepsilon| \leq \varepsilon_M$,.

The bound ε_M is dependant on the instrument's representation of floating-point numbers which, with the rounding employed and double-precision intermediate result accumulator employed in this case, is 2^{-23} for additions and multiplications. This maximum relative error also holds for division where shift operations are not employed, as in division by numbers not multiples of two [21]. ε is the local relative error related to the operation f, and it can be expressed as follows:

$$\varepsilon = \frac{\hat{f}(x,y) - f(x,y)}{f(x,y)} \tag{6.4.1}$$

In this thesis, the computation of the harmonic terms employs the following formula.

$$X(k) = \frac{1}{N+\Delta}\left[\sum_{i=1}^{N-1} x_i e^{-ji k\phi} + \left(\frac{1+\Delta}{2}\right)\cdot\left(x_N e^{-jNk\phi} + x_0 e^{-j0k\phi}\right)\right] \tag{6.4.2}$$

Where the x_i values are machine numbers.

The harmonic components X(k) will have to be scaled appropriately to finally obtain the result in the required measurement units. With the exponential factors expressed as double-precision values, their error contributions will be insignificant.

We will assume the relative error in the addition of two machine numbers to be an independently and identically distriduted (i.i.d) random variable having a mean μ_a and variance σ_a^2. Also the relative error in the multiplication of two machine numbers, will be assumed to be an i.i.d random variable having a mean μ_m and variance σ_m^2. In addition, taking into account only the linear error terms, the following expressions can

be obtained for the bounds for the means and variances of the linear form of the additions errors $(\lambda a)_k$, and the multiplications errors $(\lambda m)_k$.

$$(N+\Delta)E[(\lambda a)_k] \le \mu_a \sum_{i=1}^{N-1}(\sum_{t=0}^{i}|x_t|) = \mu_a \cdot \sum_{i=1}^{N-1}(i+1)\left\|x\right\|_\infty$$

$$= \mu_a \cdot \frac{1}{2}(N^2+N-2)\left\|x\right\|_\infty \qquad (6.4.3)$$

$$(N+\Delta)E[(\lambda m)_k] \le \mu_m \cdot (N-1)\left\|x\right\|_\infty \qquad (6.4.4)$$

$$(N+\Delta)^2 \cdot \mathrm{var}[(\lambda a)_k] \le \sigma_a^{\,2} \cdot \sum_{i=1}^{N-1}(\sum_{t=0}^{i}\left|x_t\right|^2) = \sigma_a^{\,2} \cdot \sum_{i=1}^{N-1}\left\|x\right\|_2^{\,2}$$

$$= \sigma_a^{\,2} \cdot (N-1) \cdot \left\|x\right\|_2^{\,2} \qquad (6.4.5)$$

$$(N+\Delta)^2 \cdot \mathrm{var}[(\lambda m)_k] \le \sigma_m^{\,2} \cdot \sum_{s=1}^{N-1}\left|x_s\right|^2 \le \sigma_m^{\,2} \cdot \left\|x\right\|_2^{\,2} \qquad (6.4.6)$$

If an error distribution with properties similar to those assumed for the quantization errors is used (quite valid for practical cases), then

$\mu_a = \mu_m = 0$

and

$$\sigma_a^{\,2} = \sigma_m^{\,2} = \frac{(2^{-23})^2}{12}$$

$$\approx 1.2 \cdot 10^{-15}$$

Thus even assuming that the values of $|x_S|$ are all around the ADC maximum values of 2^{11}-1 (2047), (This is worst-case situation) for example with N=512 values we obtain:

$$\mathrm{var}[(\lambda a)_k] \le 1.2 \cdot 10^{-15} \cdot \left\|x\right\|_2^{\,2}$$

$$\approx 1.2 \cdot 10^{-15} \cdot 2^{-9} \cdot (2^{11}-1)^2$$

$$\approx 9.82 \cdot 10^{-12} \qquad (6.4.7)$$

and

$$\mathrm{var}[(\lambda m)_k] \le 1.2 \cdot 10^{-15} \cdot \left\|x\right\|_2^{\,2}$$

$$\approx 1.2 \cdot 10^{-15} \cdot 2^{-18} \cdot (2^{11}-1)^2$$

$$\approx 1.92 \cdot 10^{-14} \qquad (6.4.8)$$

These variances in the harmonic computations are quite insignificant. Hence the effects of using floating-point arithmetic for the computations of the harmonic components of the signal are negligible.

6.5 Hardware errors

The system hatdware from the input to the sample-and-hold input will be considered in this section. The analysis will be simplified by considering the errors due to the component tolerances assuming ideal op-amps. It is to be expected that the non-ideal op-amps will furthur increase the system error value.

6.5.1 Voltage channel errors

Each voltage channel consists of an input voltage attenuator followed by a gain of one non-inverting op-amp, which is followed by an inverting programmable gain stage using an LF13006 digital gain set IC and an op-amp.

The input voltage attenuator stage uses 1% tolerance resitors. This stage can be analyzed as consisting of two resistors R1 and R2 with values:

R1 = 100K ± 1% and

R2 = 5M ± 1% with the output voltage taken across resistor R1.

R1 can thus have values in the range 99K-101K ohms and R2, 4950K-5050K ohms. Hence for an input voltage, the gain R1/(R1+R2) can range from

$$\left[\frac{99}{99+5050}, \frac{101}{101+4950}\right]$$

$$= [0.019227, 0.019996]$$

If 0% tolerance resistors were used, the gain would be 0.0196, thus leading to a percentage error of [-1.94%,+1.98%]

The 2nd stage is a non-inverting op-amp stage of gain 2, using two 100K 1% tolerance resistors. The voltage gain of this stage neglecting the op-amp imperfections is in the range:

$$\left[1+\frac{99}{101}, 1+\frac{101}{99}\right]$$

$$= [1.98019, 2.0202]$$

If 0% tolerance resistors were used, the gain would be 2 thus leading to a percentage error of [-0.99%,+1.01]

The 3rd stage is the programmable gain stage centered around LF13006 digital gain set IC. This configuration results in a gain error of 0.3% (per the manufacturers specifications). Hence

The worst case percentage error due to the cascaded input stages is thus approximately 3.3% (1.98+1.01+0.3).

6.5.2 Current channel errors

Each currnet channel consists of a LEM 50-P current sensor whose output is taken across a 50ohm 1% resistor. this stage is followed by a gain of one non-inverting op-amp, which is followed by an inverting programmable gain stage using an LF13006 digital gain set IC and an op-amp.

The input stage of each current amplifier employs 5turns on a LEM 50-P current module. According to the manufacturers specification, this results in a measurement error of ±0.05A. Thus a 5A signal will be measured with a relative accuracy of 1%. This current is converted to a voltage across a 50ohm 1% tolerance resistor. The worst case error due to the LEM module - resistor combination is thus 2%. The remaining two stages are identical to those of the voltage channels.

The worst case percentage error in the measurement of a 5A current signal is thus approximately 3.3% (2+1.01+0.3).

6.6 Error analysis for inaccuracies in Δ measurement

The hardware setup resolves Δ to a finite number of values. Thus Δ can have one of 16 values using a 4-bit counter or one of 256 values for an 8-bit counter. The uncertainty in the measurement of Δ for an n-bit counter is thus $\frac{1}{2^n}$.

The following notations will be used

Δ_m = Measured value of Δ

Δ_t = True value of Δ

δ_e = Error in the measurement of Δ (Δ_m - Δ_t)

The maximum value of δ_e for the hardware scheme used is thus 1/16.

6.6.1 Amplitude Measurement errors

For Δ_m the scaled DFT of the TCW is as noted in Chapter 2:

$$S_{win} W_{tcw}(\omega) = \frac{1}{N+\Delta_m}\left[\frac{\sin\frac{N\omega}{2}}{\sin\frac{\omega}{2}}\cos\frac{\omega}{2} + \Delta_m \cos\frac{N\omega}{2}\right] e^{\frac{-jkN\phi}{2}}$$

Since $\Delta_m = \Delta_t + \delta_e$
the Amplitude expresion reduces to:

$$|S_{win} W_{tcw}(\omega)| = \left| \frac{1}{N+\Delta_t+\delta_e} \left[\frac{\sin\frac{N\omega}{2}}{\sin\frac{\omega}{2}} \cos\frac{\omega}{2} + (\Delta_t+\delta_e)\cos\frac{N\omega}{2} \right] \right|$$

$$= \left| \frac{1}{N+\Delta_t} \left(1+\frac{\delta_e}{N+\Delta_t}\right)^{-1} \left[\frac{\sin\frac{N\omega}{2}}{\sin\frac{\omega}{2}} \cos\frac{\omega}{2} + \Delta_t \cos\frac{N\omega}{2} + \delta_e \cos\frac{N\omega}{2} \right] \right|$$

$$= \left| \frac{1}{N+\Delta_t} \left(1-\frac{\delta_e}{N+\Delta_t}\right) \left[\frac{\sin\frac{N\omega}{2}}{\sin\frac{\omega}{2}} \cos\frac{\omega}{2} + \Delta_t \cos\frac{N\omega}{2} + \delta_e \cos\frac{N\omega}{2} \right] \right|$$

$$|S_{win} W_{tcw}(\omega)| = \left| \frac{1}{N+\Delta_t} \left[W_{TT} + \delta_e \cos\frac{N\omega}{2} - \frac{\delta_e}{N+\Delta_t} W_{TT} - \frac{\delta_e^{\,2}}{N+\Delta_t} \cos\frac{N\omega}{2} \right] \right|$$

$$\approx \frac{1}{N+\Delta_t} \left[W_{TT} + \delta_e \cos\frac{N\omega}{2} \right]$$

where

$$W_{TT} = \frac{\sin\frac{N\omega}{2}}{\sin\frac{\omega}{2}} \cos\frac{\omega}{2} + \Delta_t \cos\frac{N\omega}{2}$$

Since for $\omega << 1$, W_{TT} is small (TCW algorithm effect), the worst case error in the measurement of the amplitude is thus approximated by.

$$\frac{\delta_e}{N+\Delta_t} \cos\frac{N\omega}{2}$$

$$\approx \frac{\delta_e}{N}$$

With N=512 and the maximum value of δ_e for the hardware scheme used (1/16) results in the maximum amplitude error of:

$1.22 \cdot 10^{-4}$

6.6.2 Phase Measurement error

Based on the expression for the scaled DFT of the TCW as noted in Chapter 2:

$$S_{win}W_{tcw}(k\phi)=\frac{1}{N+\Delta}\left[\frac{\sin\frac{Nk\phi}{2}}{\sin\frac{k\phi}{2}}.\cos\frac{k\phi}{2}+\Delta.\cos\frac{Nk\phi}{2}\right].e^{\frac{-jkN\phi}{2}}$$

For $k\phi<<1$,
the Phase expresion is:

$$\angle S_{win}W_{tcw}(k\phi)=\frac{-kN\phi}{2}$$

$$=\frac{-k\pi N}{N+\Delta_i+\delta_e}$$

Neglecting δ_e^2 and higher powers, the above equation reduces to:

$$\angle S_{win}W_{tcw}(k\phi)=\frac{-kN\phi}{2}$$

$$=\frac{-k\pi N}{N+\Delta_i}\left(1-\frac{\delta_e}{N+\Delta_i}\right)$$

The maximum error in the phase measurement can thus be approximated by

$$\frac{k\pi\delta_e}{N}$$

expressed in degrees, this is:

$$\frac{180k\,\delta_e}{N}$$

and with N=512 and the maximum value of δ_e for the hardware scheme used (1/16) results in the maximum amplitude value at harmonic k being:

0.022k degrees
which results in a maximum phase deviation of 0.22 degrees for the 10th harmonic.

6.7 Summary of results

ADC quantization effects result in the harmonic amplitude means being slightly biased, while the phase means are unbiased. However, the standard deviation of both amplitude and phase vary inversely as the square root of N. In addition the phase standard deviation is inversely proportional to the harmonic amplitude.

Sampling jitter effects result in the harmonic amplitude means being slightly biased, while the phase means are unbiased. However, the standard deviation of both amplitude and phase vary inversely as the square root of N and proportional to the signal frequency and the standard deviation of the time jitter. In addition the harmonic phase standard deviation is proportional to the signal amplitude.

Errors due to the use of floating or fixed-point arithmetic computations will have a negligible effect on the accuracy of the computed harmonic components.

The errors due to the inaccuracy in the measurement of delta have far less of an effect on the amplitude measurement compared to the that of the phase measurement. For measurement up the 10th harmonic, the amplitude error contribution is up to order of 10^{-4} while the phase has a maximun error of 0.22 degrees. In general an increase in the resolution of mesurement of the end-correction will further minimize the error contributed by the inaccuracy in the end-correction measurement.

The significant sources of error will thus be due to the system hardware component tolerances and imperfections. Based on a knowledge of the actual hardware errors, a correction can be performed in software to account for these errors after a calibration of the system. This conclusion can be drawn from the approximately 3.3% error value for the voltage and current channels as opposed to the less than 1% error due to the quantization and computation scheme employed as well as the floating-point representation used.

7. FOURIER ANALYZER PERFORMANCE AND SPECIFICATIONS

The Fourier analyzer performnce when various input waveforms are applied is compared with those of other instruments in some cases, and in others a comparision with certain waveform components derived theoretically is performed. Another important feature examined here is the computational speed of the TCW algorithm on a given sample set using various hardware and operating system platforms.

7.1 Calibration

The calibration procedure is similar for all 4 channels. As with any typical instrument calibration, prior to performing the calibration, the instrument should be run for a while (at least a couple of hours). Ground all four channel inputs. With reference to channel 1, variable resistors R68 and R69 are adjusted till the voltage reading at test point CH1 is zero. The calibration menu should next be entered (key input 2). Resistor R3 should then be adjusted till a reading of 0800 is indicated on channel 1. A similar procedure for the other three channels are next performed using the appropriate variable resistors.

7.2 Performance Checks

The digital instrument RMS readings were compared to a test digital voltmeter. The results are tabulated in Table 7.1 and plotted in Figure 7.1. As indicated in Figure 7.1, a linear relationship between the computed rms value and input signal amplitude occurred when a sinusoidal at 58.87Hz was applied to the channel 1 input.

TABLE 7.1 RMS readings of Fourier analyzer and a 4-1/2 digit test digital meter

FOURIER ANALYZER RMS READING /Volts	TEST DIGITAL METER (4-1/2 digit) READING /Volts
0.70	0.73
4.71	4.91
9.6	9.97
14.54	15.09
19.53	20.25
24.04	24.9
29.06	30.1
33.90	35.1
38.65	40.01
43.52	45.01
48.21	50.0
53.14	55.05
58.30	60.4
62.70	65.00
67.56	69.96
72.55	75.15
77.54	80.3
82.94	85.88
88.11	91.3
92.62	95.96
97.37	100.81
102.36	106.0
106.51	110.35
111.74	115.76
115.66	119.91

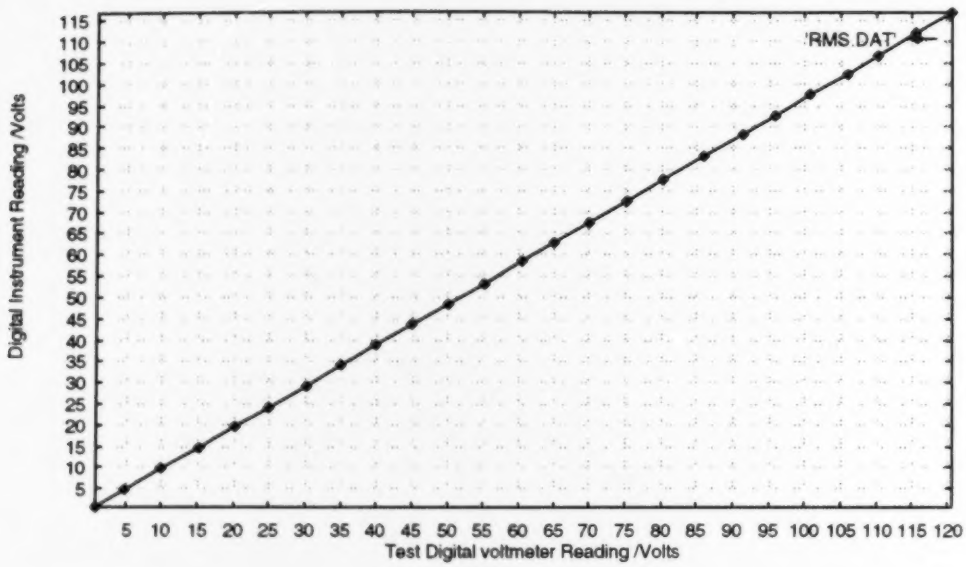

Figure 7.1 RMS reading of a test voltmeter and the Fourier analyzer

The results of the analyzer readings using a square-wave of peak-to-peak value of 20V and a frequency of 59.95Hz as input, is tabulated in Table 7.2. The magnitude plot is indicated in Figure 7.2. The results are compared with a scaled and translated result obtained from a theoretical square waveform which is also plotted in Figure 7.2. The theoretical fitted waveform resulted in a correlation coefficient of 0.99999. The results indicate non-zero values at harmonic components which theory indicates should read zero. This is due to the system hardware error effects. Primariliy the limited bandwidth of the instrument and the non-uniform slew-rate effects of the op-amps employed (different rising and falling edge slew-rate values) result in a voltage offset from zero at the sample-and-hold amplifier inputs.

TABLE 7.2 Fourier analyzer readings for a 20V p-p 59.95Hz square wave

Harmonic Number	Magnitude /Volts	Phase /degrees
0	0.28	0.00
1	12.03	0.32
2	0.17	0.02
3	4.01	0.32
4	0.17	0.03
5	2.4	0.32
6	0.20	0.04
7	1.72	0.32
8	0.2	0.05
9	1.33	0.32
10	0.17	0.09
11	1.09	0.31
12	0.17	0.11
13	0.92	0.31
14	0.14	0.14
15	0.80	0.31
16	0.11	0.21
17	0.68	0.31
18	0.13	0.18
19	0.61	0.30
20	0.17	0.16
21	0.54	0.30
22	0.17	0.18
23	0.49	0.29
24	0.20	0.17
25	0.45	0.28
26	0.17	0.20
27	0.41	0.28
28	0.17	0.22
29	0.37	0.27
30	0.14	0.26

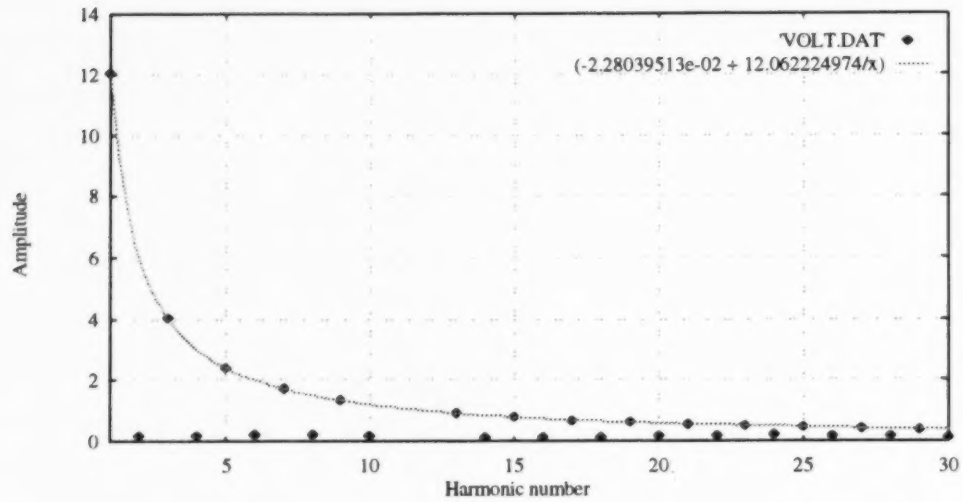

Figure 7.2 Plot of the Fourier analyzer amplitude results and fitted square wave

The results of the Fourier analyzer readings with a triangular wave of peak-to-peak value of 20V and a frequency of 60.01Hz as input, is tabulated in Table 7.3. The magnitude plot is indicated in Figure 7.3. The results are compared with a scaled and translated result obtained from a theoretical triangular waveform which is also plotted in Figure 7.3. The theoretical fitted waveform resulted in a correlation coefficient of 0.99999.

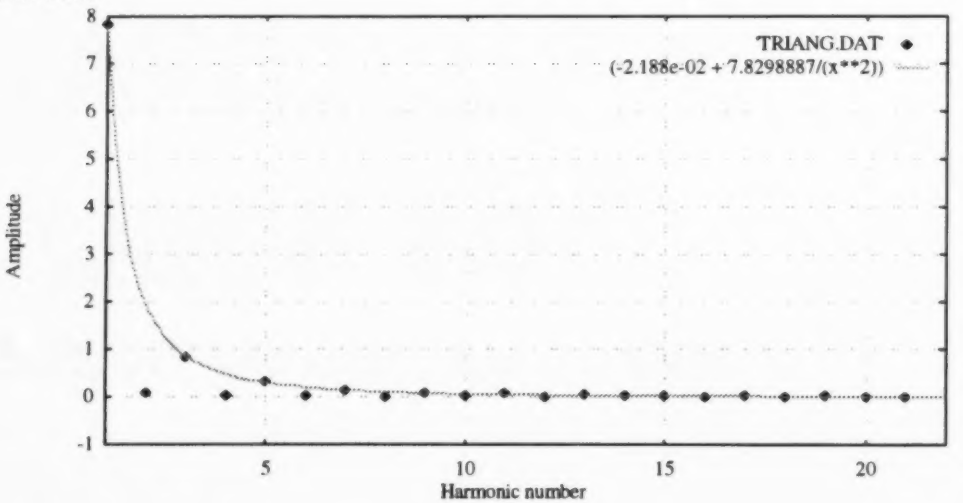

Figure 7.3 Plot of the Fourier analyzer amplitude results and fitted triangular wave

TABLE 7.3 Fourier analyzer readings for a 20V p-p 60.01Hz triangular wave

Harmonic	Magnitude /Volts	Phase /Degrees
0	0.25	0
1	7.81	0.32
2	0.08	0.16
3	0.84	0.29
4	0.02	0.02
5	0.31	0.23
6	0.02	0.26
7	0.14	0.10
8	0.00	0.66
9	0.08	0.01
10	0.01	0.30
11	0.07	0.17
12	0.00	0.66
13	0.04	0.27
14	0.01	0.21
15	0.03	0.26
16	0.00	0.66
17	0.02	0.30
18	0.00	0.66
19	0.02	0.30
20	0.00	0.66
21	0.00	0.40

7.3 Specifications

The Fourier analyzer specifications as defined by the hardware platform on which the TCW algorithm algorithm is implement are indicated below.

Input Voltage /V	-500 ... 500
Load current /A	-10 ... 10
Maximum Power /W	5000
Frequency Range /hz	12 ... 1000

	Acquisition, computation and display times (display enabled)	Acquisition, computation and display times (display disabled)
Calibrate DC (all channels sequentially)	70ms	
DC (Phase 1 or Phase 2)	90ms	
DC(3- Phase)	100ms	
AC (1-phase)	1.7s	
AC power (3-phase)	1.2s	
Frequency (60Hz signal)	33ms	
DFT(521 samples,Phase 1)	Mag-Phase mode: 12s (≈ 4s per harmonic) Real-Imag mode: 10s (≈ 3.3s per harmonic)	10s

Power requirements

+5volts 1.2A
+15volts 120mA
-15volts 150mA

Voltages and power readings are read to one decimal place. Current and power factor readings can be read to two decimal places.

7.4 Algorithm performance on various platforms

To determine the speed of computation of the modified DFT algorithm using the TCW, computer simulations were performed on various hardware and operating system platforms. The simulation results are found in Table 7.4. The sample values were obtained from a multi-frequency signal having Δ = -0.125 and N=521. The simulation program read these sample values from a lookup table.

TABLE 7.4 Harmonic Computation Benchmarks for various platforms

Machine	Computation time for 260 harmonics (display disabled)	Computation time for 260 harmonics (display enabled)
286-10Mhz PC /8MB ram	363.09s (1)	371.01s (1)
486 DX33 PC /16MB ram	3.24s (1) 3.23s	5.68s (1) 5.65s
486 DX 40 PC /8MB ram	2.73s (1) 2.71s	5.19s (1) 5.19s
486 DX2-66 PC /8MB ram	1.63s (1) 1.63s	2.97s (1) 2.90s
Sun Sparcstation IPC	1.0s	1.267s
Sun Sparc station LX	0.475s	0.65s
HP9000-715	0.185s	0.24s
HP9000-735 (> 20 users)	0.095s	0.1s

(1)- Floating point emulation used

It can be seen that on the right platform (hardware and operating system), the algorithm can be used for the speedy computation of the DFT components. The platform used in the thesis is not the best in demonstrating speed of computation.

8. CONCLUSIONS

The TCW algorithm has been analyzed and the various error contributions in a practical instrumentation implementation have been examined. Signals sampled synchronously at frequencies an order of magnitude greater than the Nyquist frequency can be measured accurately by DFT type algorithms in existence. Hence the thrust in this thesis was on asynchronously sampled signals.

The DC value measurement of asynchronously sampled distorted signals was initially examined. The results of the analysis in Chapter 2, indicates the reduction of long and medium range leakage effects. The medium range error reduction is due to the fact that the first null of the window DTFT main lobe is close to the fundamental frequency. The width of the TCW varies with the period of the signal and results in the subsequent nulls of the window DTFT being close to the actual harmonic frequencies. This latter effect of the TCW minimizes the long range leakage effects. Since long and medium range leakage are the main contribution to errors in the DC computation of asynchronously sampled signals, the excellent measurement accuracy of this algorithm was not unexpected.

The general harmonic computation problem was next examined in Chapter 3. The knowledge of the end-correction Δ enables the computation of signal harmonic components at the actual harmonic frequencies. This latter advantage of the TCW algorithm thus reduces the last form of leakage error; short-range effects. Measurement accuracy of both amplitude and phase components have thus been established. Two waveform examples which confirmed the superiority of this algorithm in precision harmonic measurements have been included in the analysis.

The hardware and software implementation of the Fourier analyzer were also discussed. The stand-alone instrument uses readily available components and can measure the parameters of two loads simultaneously. The software utilizes a menu-driven interface. The system software also consists of a number of subprograms which are used in acquiring, storing, computing and displaying various parameters and the system status.

As in every measurement scheme, the effect of non-ideal situations arising from practical implementations has been examined in Chapter 6. Errors due to quantization effects, sampling jitter, arithmetic computation schemes, hardware component tolerances and inaccuracy in the measurement of the end-correction errors have been examined. The major error contribution being due to the hardware component tolerances.

Performance results of the instrument indicate a close correlation with theoretical waveforms which point to the fact that the minimization of hardware errors using more precise hardware would result in results close to the theoretical expectations of the TCW algorithm.

The TCW algorithm has been shown to improve both the amplitude and phase measurement accuracy of signals while using a windowing-modified DFT approach,

without resorting to post-processing interpolation or other techniques. Some areas of the benefits of improved amplitude and phase measurement are important in PWM waveform analysis, design for the proper compensation of non-active powers, effective reduction of the harmonic content and correct revenue metering in electrical networks.

8.1 The unique contributions of this thesis

- The introduction of the TCW algorithm for improved accuracy harmonic computations of the amplitude and phase of periodic signals without necessarily resorting to more than one period of the signal.

- The class of compensating windows has been introduced opening a whole new field of precision harmonic analysis instrumentation. This is based on the concept of the knowledge of the end-correction included in an appropriate classical window.

- The first practical implementation of a Fourier analyzer based on the trapezoidal compensating window or any other compensating window approach.

8.2 Limitations of the TCW scheme as implemented in this thesis

- The hardware platform is the main limitation on the instrument system accuracy (see Chapter 6). The existing hardware platform on which the TCW algorithm is implemented has been shown to have an accuracy of at least 3.3%.

- Real time display could not be attained due to the underlying hardware and software speed limitations

8.3 Suggestions for further work

Although the system met the design specifications, finance and the available components placed a limitation on some desirable features which could be included. Further work that can be done include the following:

- Improvement of the hardware data acquisition system. Some suggestions include the incorporation of devices to support a higher sampling rate and precision front-end analog components and circuitry. Including components with higher frequency bandwidths will also enable the upper frequency limit of the instrument to be extended.

- The use of a math coprocessor or a device suited to multiply-accumulate type operations (e.g. DSP chips, or certain RISC implementations such as the PowerPC series) would boost the system performance.

- Further work can be performed in the implementation of faster algorithms for the evaluation of the modified DFT based on the TCW and the introduction of new compensating windows derived from existing classical windows.

- In a fast sampling setup, a scheme could set up to process a subset of the acquired samples to satisfy a particular error figure. This sample subset can be obtained by employing a decimation scheme.

- A simulation of a compete instrument for the study and verification of all errors.

- A study of alternate hardware schemes for the measurement of the end-correction. Studying the effect of noise on zero-crossing detectors and methods for the improvement of the measurement accuracy of Δ.

- The use of a suitably designed data acquisition board and computer setup. The data acquisition board should have a means of determining the end-correction (Δ). The TCW algorithm could be compiled to run on the PC. This will allow comparisons to be made with various other algorithms effectively. The user software can produce a graphical on-screen display of the harmonic components. Real-time display can be implemented if adequate processing power is available.

- Comparisons of the effects on measurement accuracy as a result of averaging versus single sample sampling can also be further examined.

REFERENCES

[1] ANDRIA G., SAVINO M., TROTTA A., "Windows and Interpolation Algorithms to Improve Electrical Measurement Accuracy". *IEEE Transactions on Instrumentation and Measurement*, vol. 38, no. 4, pp. 856-863, August 1989.

[2] BOWES S. R., MIDOUN A., "Suboptimal Switching Strategies for Microprocessor-Controlled PWM inverter drives", *IEE Proceedings*, vol. 132, pt. B, no. 3, pp. 133-148, May 1985.

[3] CALVETTI D., "A Stochastic Roundoff Error Analysis for the Fast Fourier Transform", *Mathematics of Computation*, vol. 56, no. 194, pp. 755-774, April 1991.

[4] FERRERO A., OTTOBONI R., "A New Approach to the Fourier Analysis of Periodic Signals For the Minimization of the Phase Errors". *IEEE Transactions on Instrumentation and Measurement*, vol. 40, no. 4, pp. 694-698, August 1991.

[5] GRANDKE T., "Interpolation Algorithms for Discrete Fourier Transforms of Weighted Signals". *IEEE Transactions on Instrumentation and Measurement*, Vol. IM-32, pp. 350-355, June 1983 .

[6] HARRIS F. J., "On the Use of Windows for Harmonic Analysis with the Discrete Fourier Transform". *Proceedings of the IEEE*, vol. 66, no. 1, pp. 51-83, January 1978.

[7] JAIN V. K., COLLINS W. L., DAVID D. C., "High Accuracy Analog Measurements via the Interpolated FFT", *IEEE Transactions on Instrumentation and Measurement*, vol IM-28, no. 2, pp. 113-122, June 1979 .

[8] NONWEILER T. R. F., *Computational Mathematics - An introduction to numerical approximation*, Ellis Horwood Ltd., 1984.

[9] NYARKO D., STROMSMOE K., "Analysis of Truncation Errors in Asynchronous Sampling of Periodic Signals", *Proceedings of the 34th Midwest Symposium on Circuits and Systems*, Monterey, California, pp. 1117-1120, May 14-17, 1991.

[10] NYARKO D., STROMSMOE K., "Error Analysis in Digital Sampling Instruments Employing Numerical Integration Techniques", *Proceedings of the IASTED international Symposium: Computers, Electronics, Communication and Control*, Calgary, Canada, pp. 212-215, April 8-10, 1991 .

[11] NYARKO D., "A High Accuracy Digital Sampling Wattmeter", MSc. Thesis, University of Alberta, 1989.

[12] OPPENHEIM A.V., SCHAFER R.W., *Discrete-Time Signal Processing*, Prentice-Hall, 1989.

[13] PATEL H. S., HOFT R. G., "Generalized Techniques of Harmonic Elimination and Voltage Control in Thyristor Inverters: Part 1-Harmonic Elimination", *IEEE Transactions on Industry Applications*, vol. IA-9, no. 3, pp. 310-317, May/June 1973 .

[14] SALVATORE L., TROTTA A., "Flat Top windows for Pwm Waveform Processing Via DFT", *IEE Proceedings*, vol. 135, pt. B, no. 6, pp. 346-361, November 1988.

[15] STENBAKKEN G. N., "High-Accuracy Sampling Wattmeter", *IEEE Transactions on Instrumentation and Measurement*, vol. 41, no. 6, pp. 974-978, December 1992.

[16] STENBAKKEN G. N., "A Wideband Sampling Wattmeter", *IEEE Transactions on Power Apparatus and Systems*, vol. PAS-103, no. 10, pp. 2919-2925, October 1984.

[17] TURGEL R. S., "Digital Wattmeter using a Sampling Method", *IEEE Trans. on Instrumentation and Measurement*, vol. IM-23, no. 4, pp. 337-341, December 1974.

[18] VAN DEN BOS A., "Best Linear unbiased Estimation of the Fourier Coefficients of Periodic Signals", *IEEE Transactions on Instrumentation and Measurement*, vol. 42, no. 1. pp. 49-51, February 1993.

[19] WAGDY M. F., "Effect of ADC Quantization Errors on some Periodic Signal Measurements", *IEEE Transactions on Instrumentation and Measurement*, vol. IM-36, no. 4, pp. 983-989, December 1987.

[20] WAGDY M. F., AWAD S. S., "Effect of Sampling Jitter on some Sine Wave Measurements", *IEEE Transactions on Instrumentation and Measurement*, vol. 39, no. 1, pp. 86-89, February 1990.

[21] WILKINSON J. H., *Rounding errors in algebraic processes*, Prentice-Hall 1963.

[22] ZU-LIANG L., "An Error Estimate for Quasi-Integer-Period Sampling and an Approach for Improving its Accuracy", *IEEE Transactions on Instrumentation and Measurement*, vol IM-37, no. 2, pp. 219-222, June 1988.

APPENDIX

SCHEMATIC DIAGRAMS

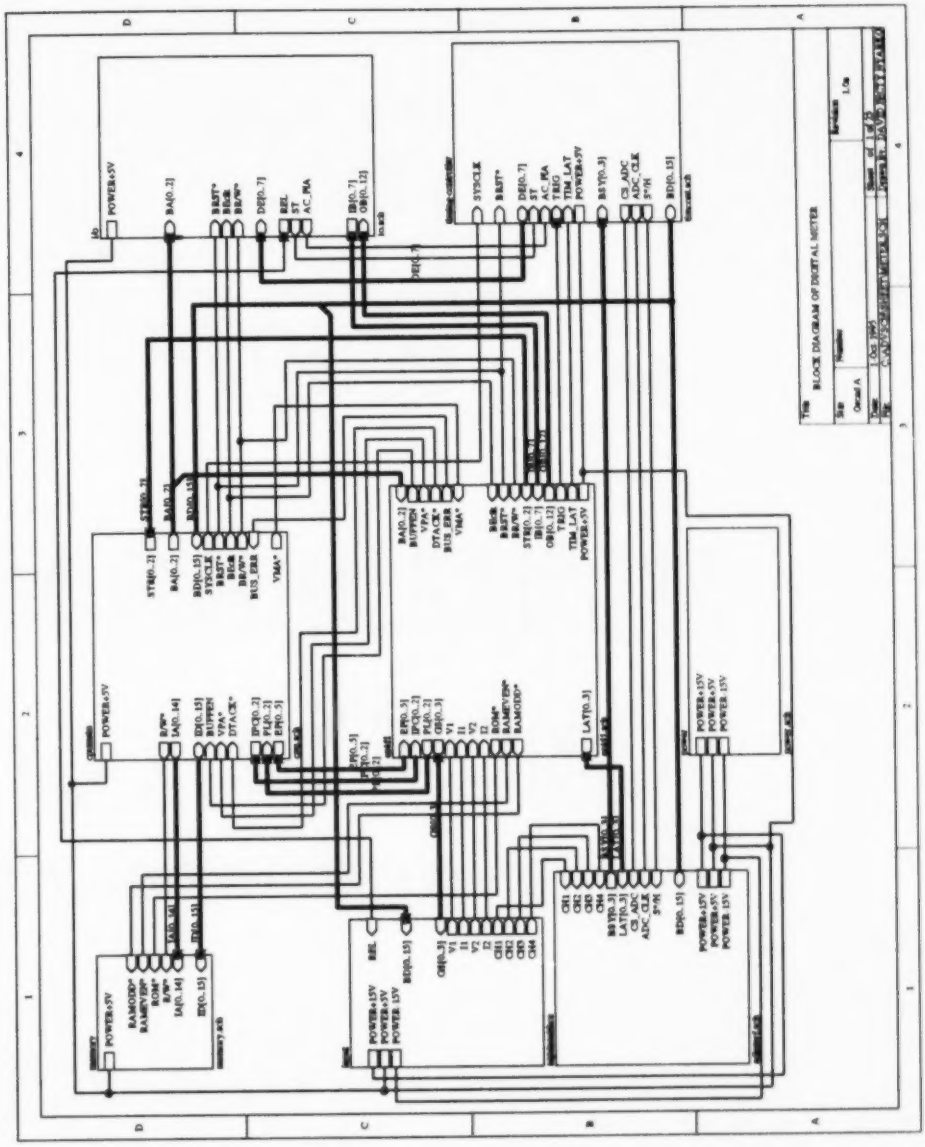
BLOCK DIAGRAM OF DIGITAL METER

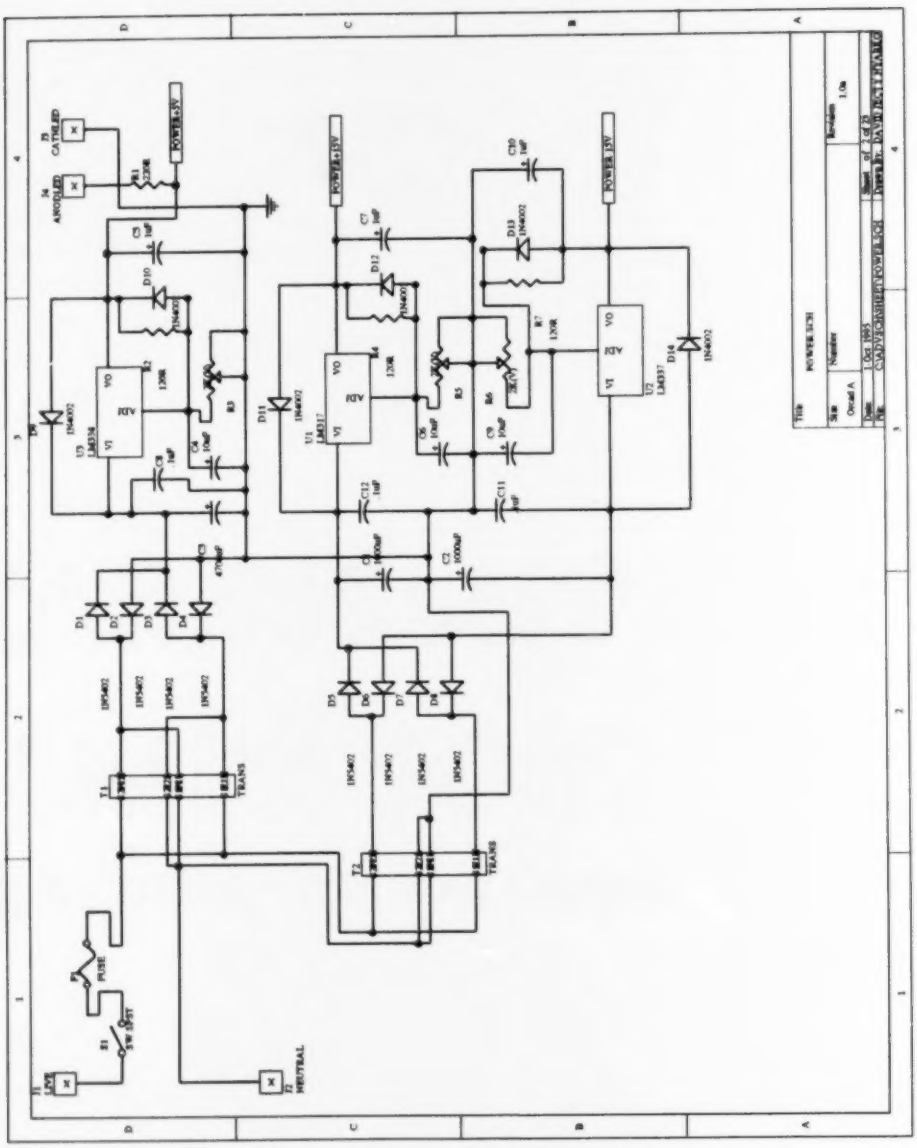

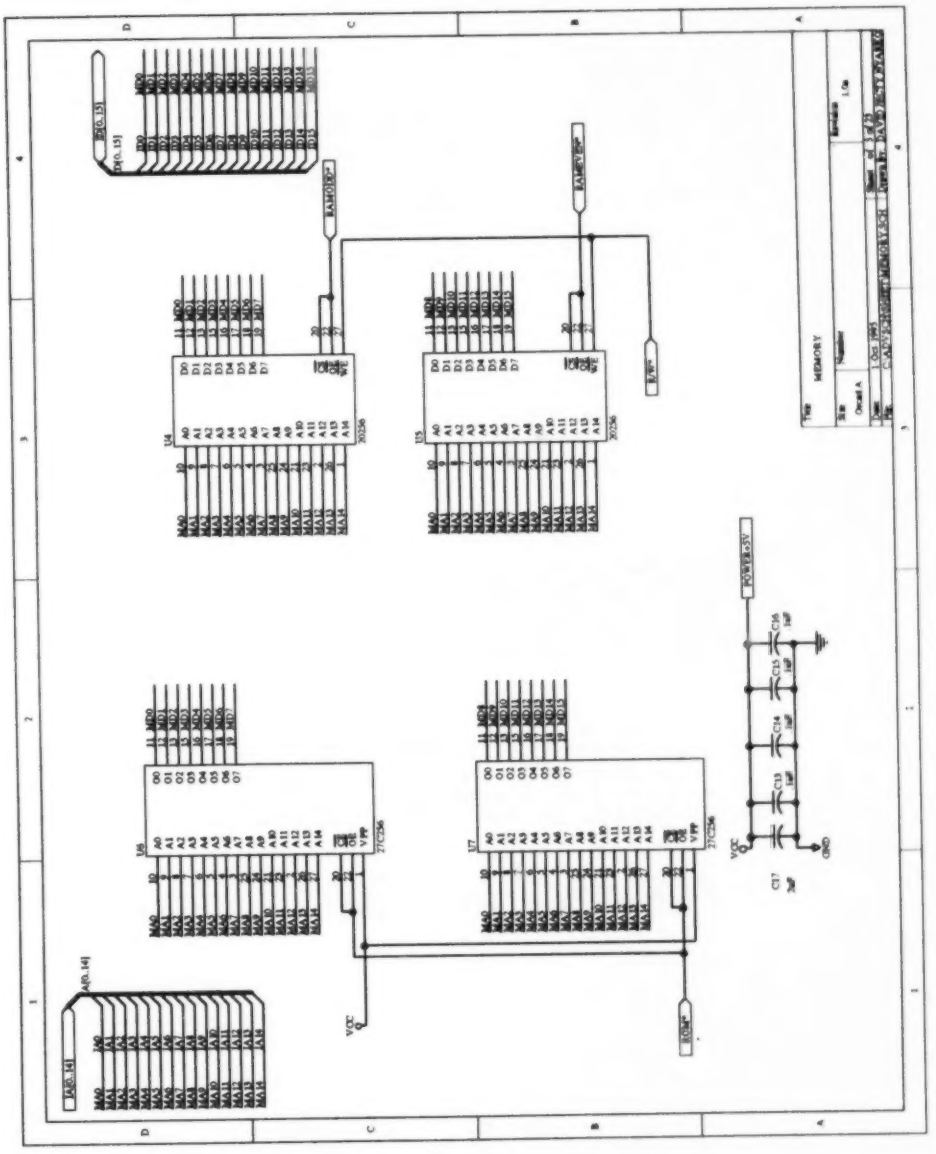
MEMORY
U4
U5
U6
U7
27C256
VCC
GND
POWER5V

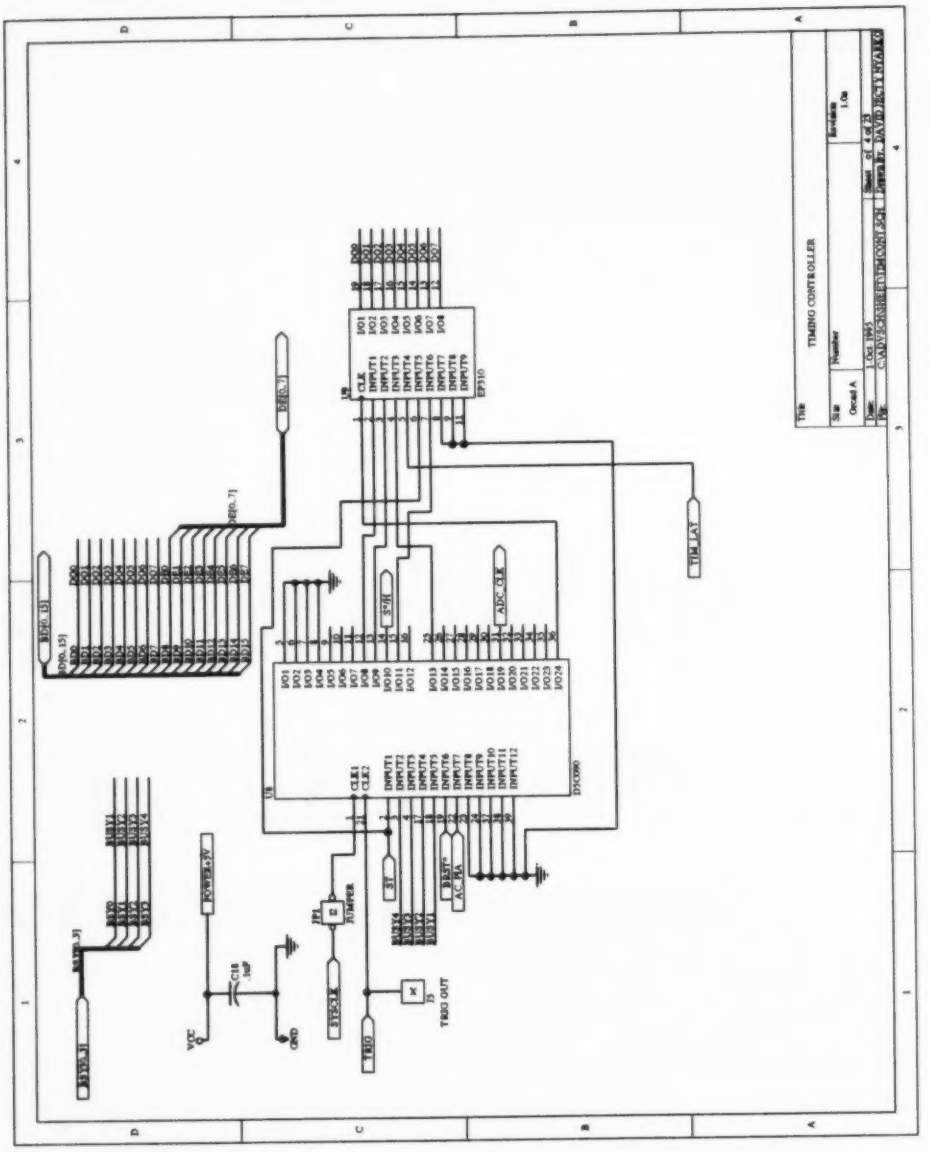
TIMING CONTROLLER
TIM_LAT
ADC_CLK
TRIG OUT
VCC
GND
JUMPER
EP310
DSC090

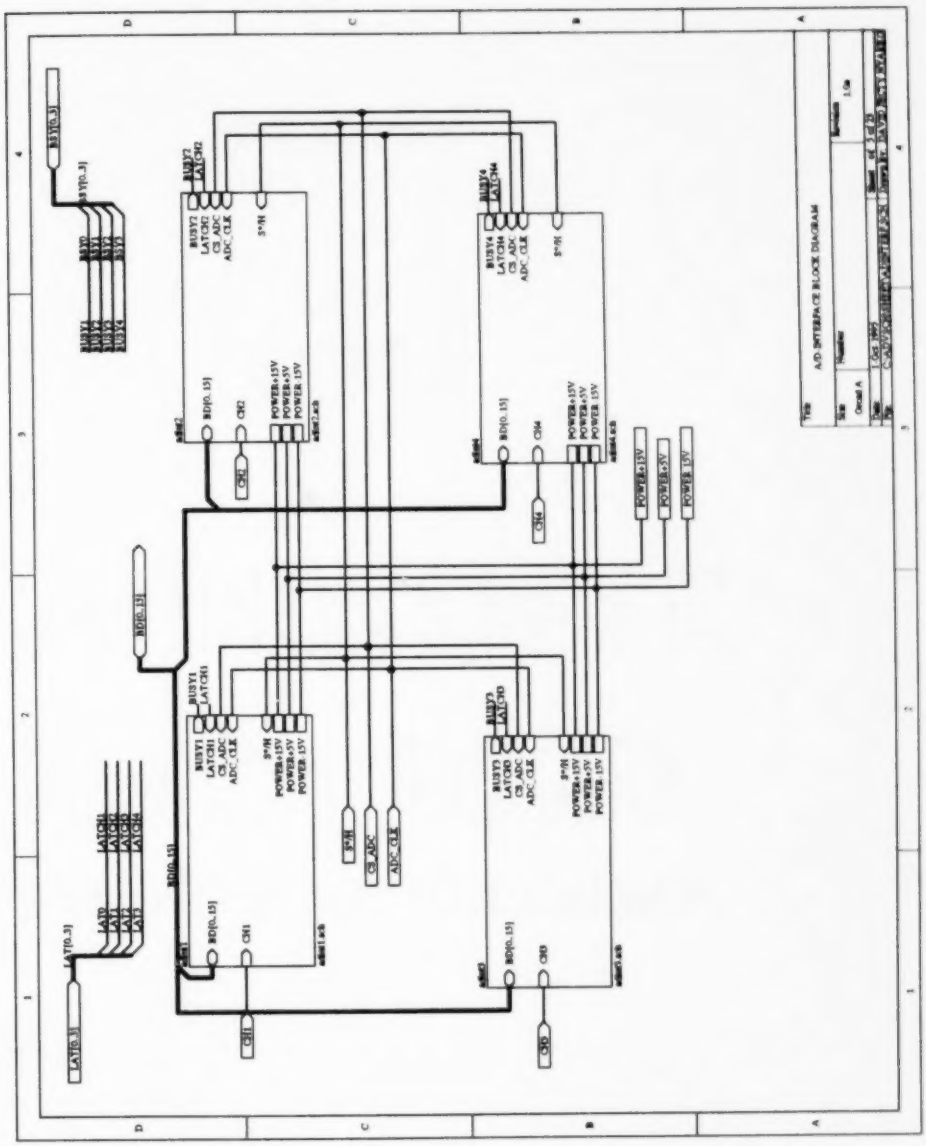
A/D INTERFACE BLOCK DIAGRAM

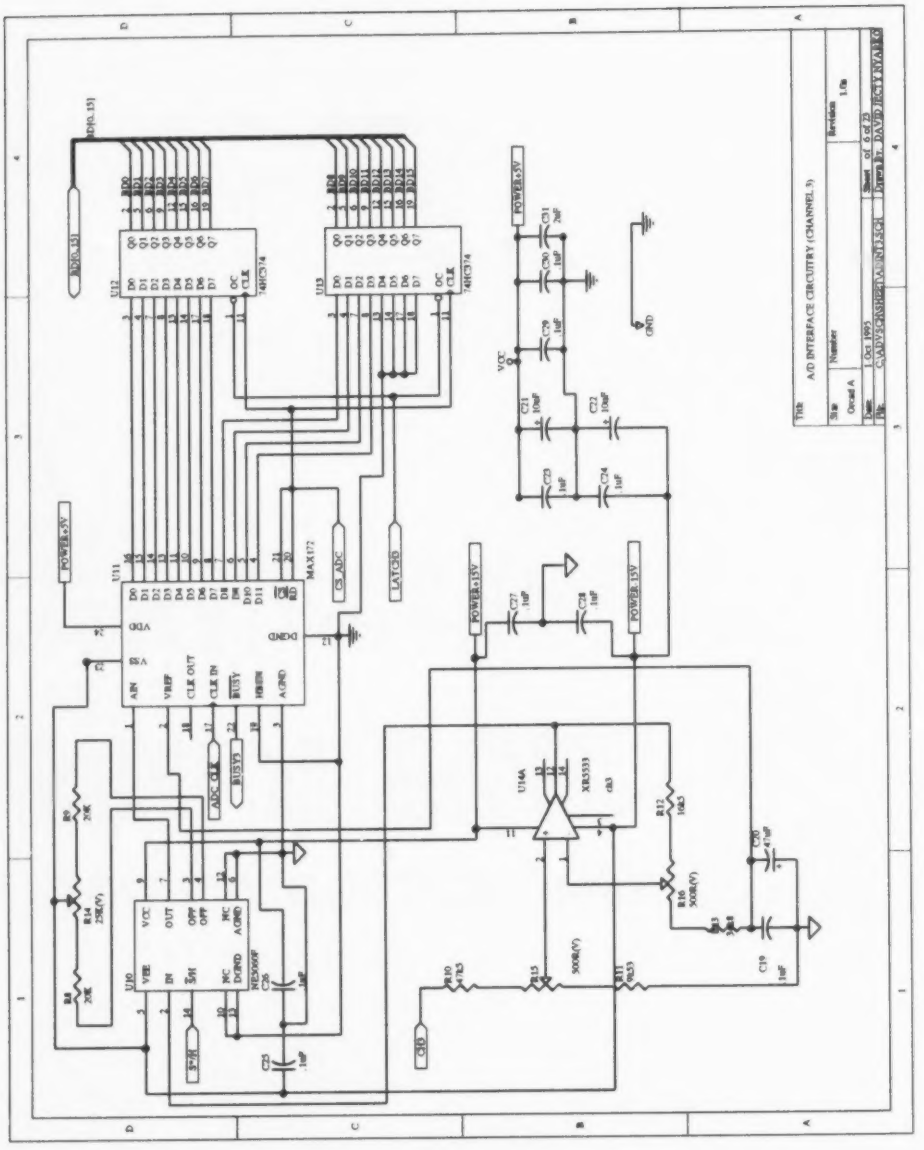
A/D INTERFACE CIRCUITRY (CHANNEL 5)
MAX172
74HC374
XR5533
NE5000P
CS_ADC
LATCH5
ADC CLK
BUSY5
POWER+15V
POWER-15V
POWER+5V
VCC
GND

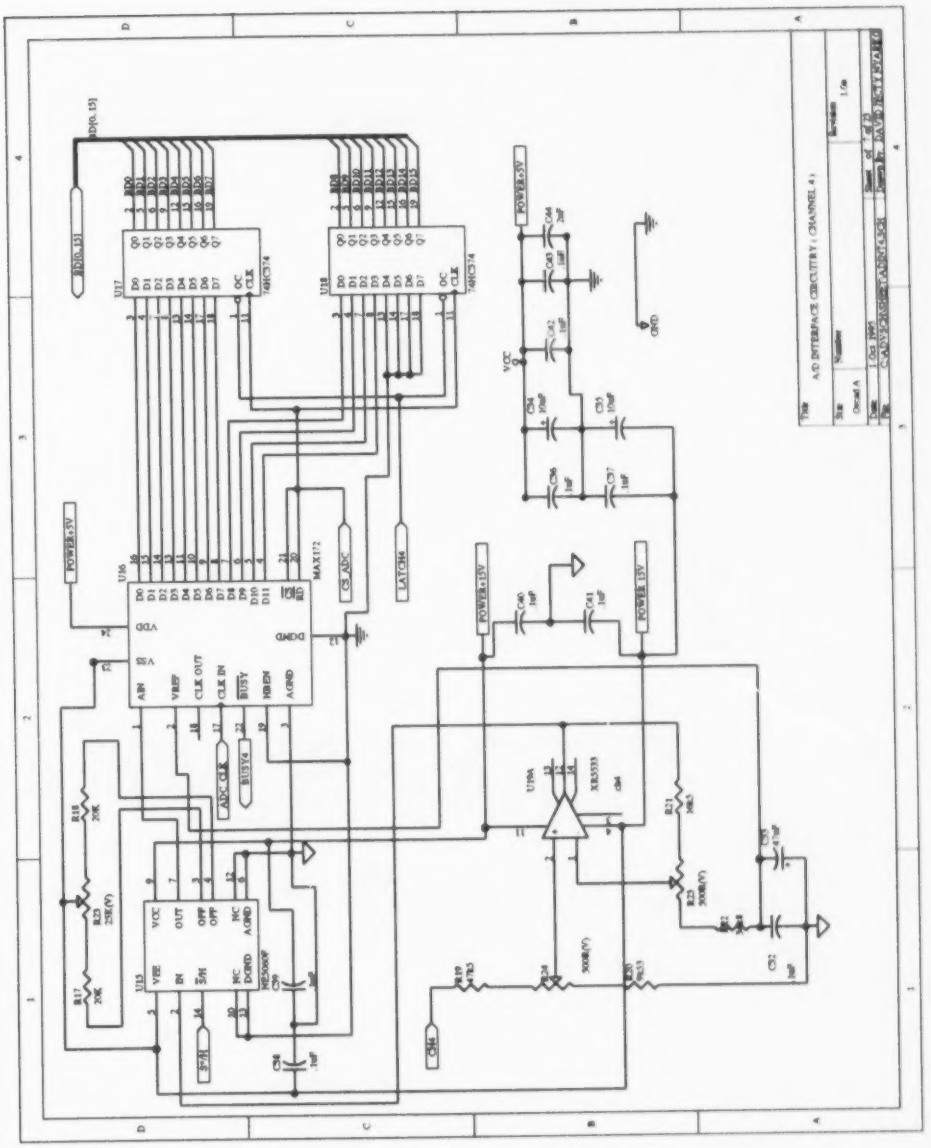

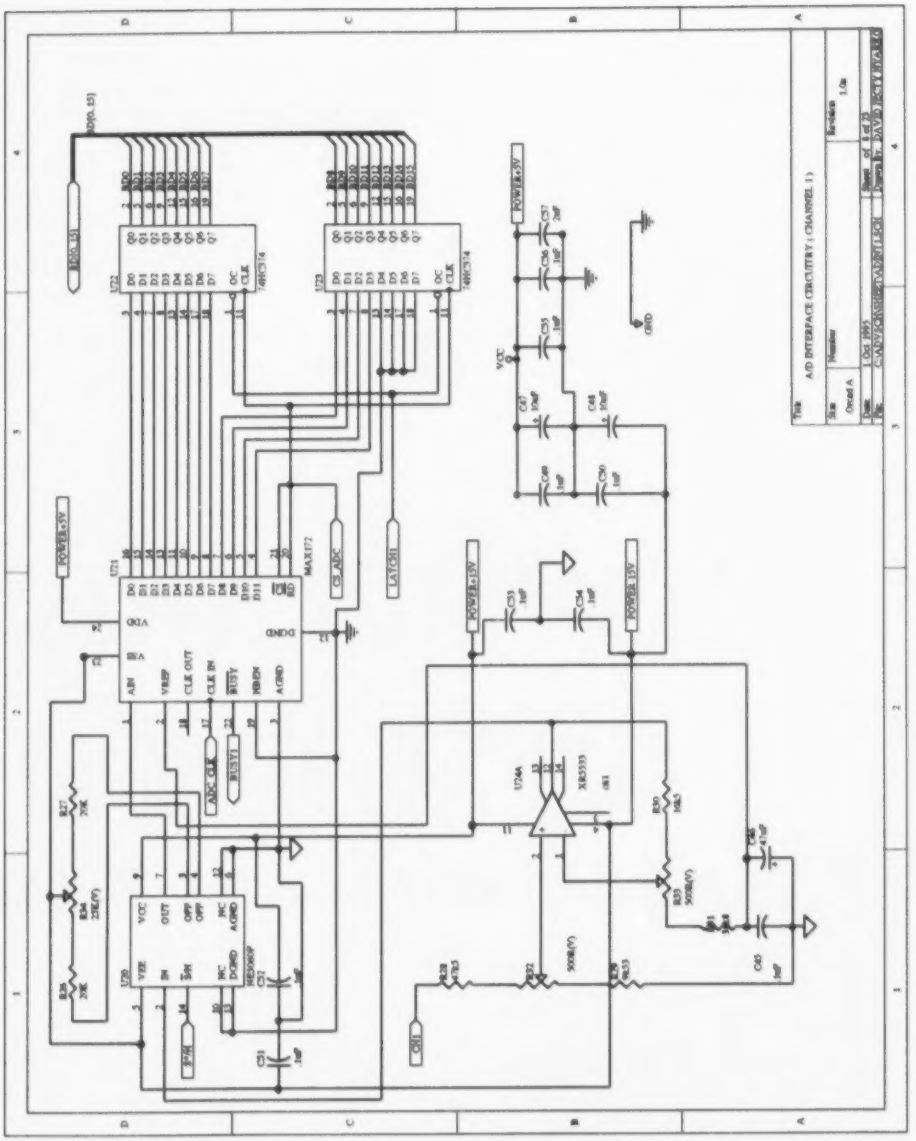
A/D INTERFACE CIRCUITRY (CHANNEL 1)
MAX172
74HC374
U1744
XR5533
POWER+5V
POWER-15V
GND
ADC_CLK
BUSY
CS_ADC
LATCH1
DB0..15
CH1

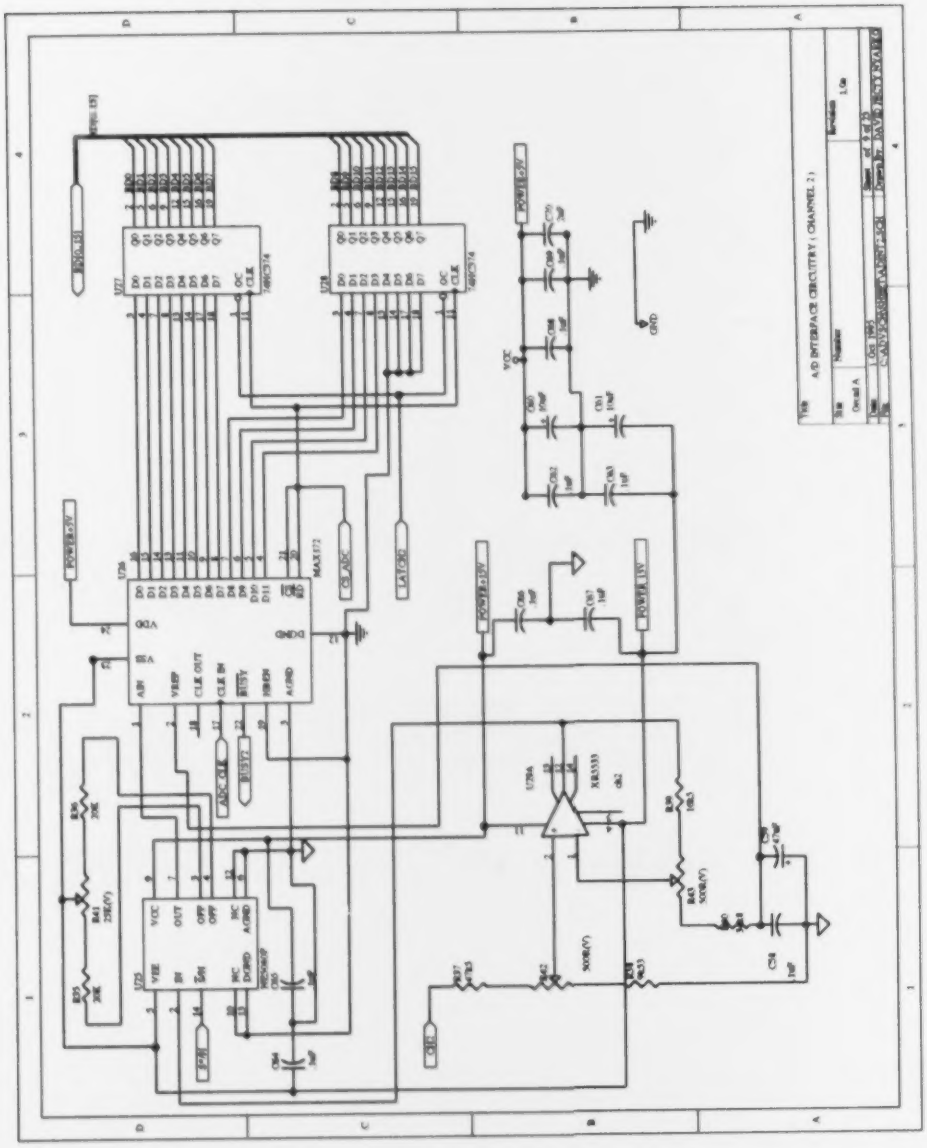

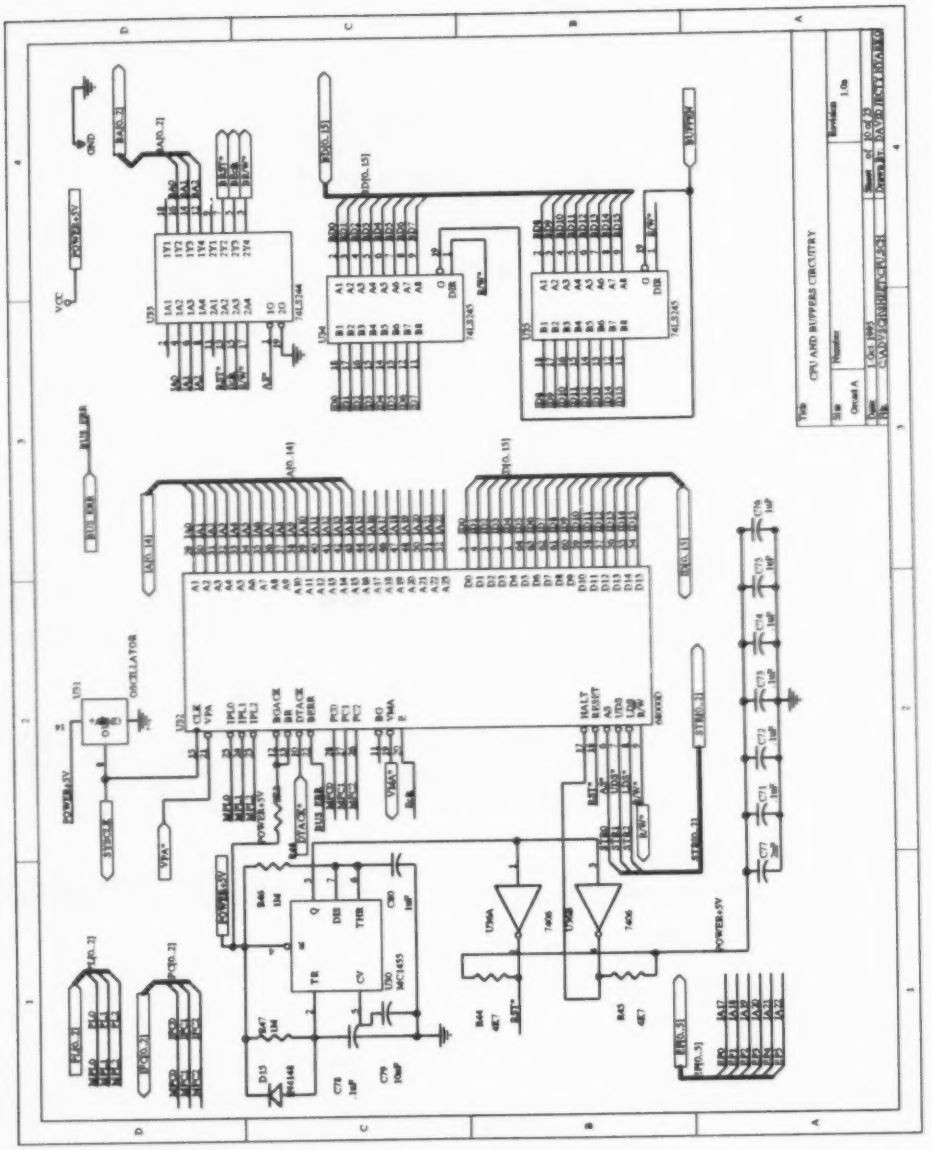

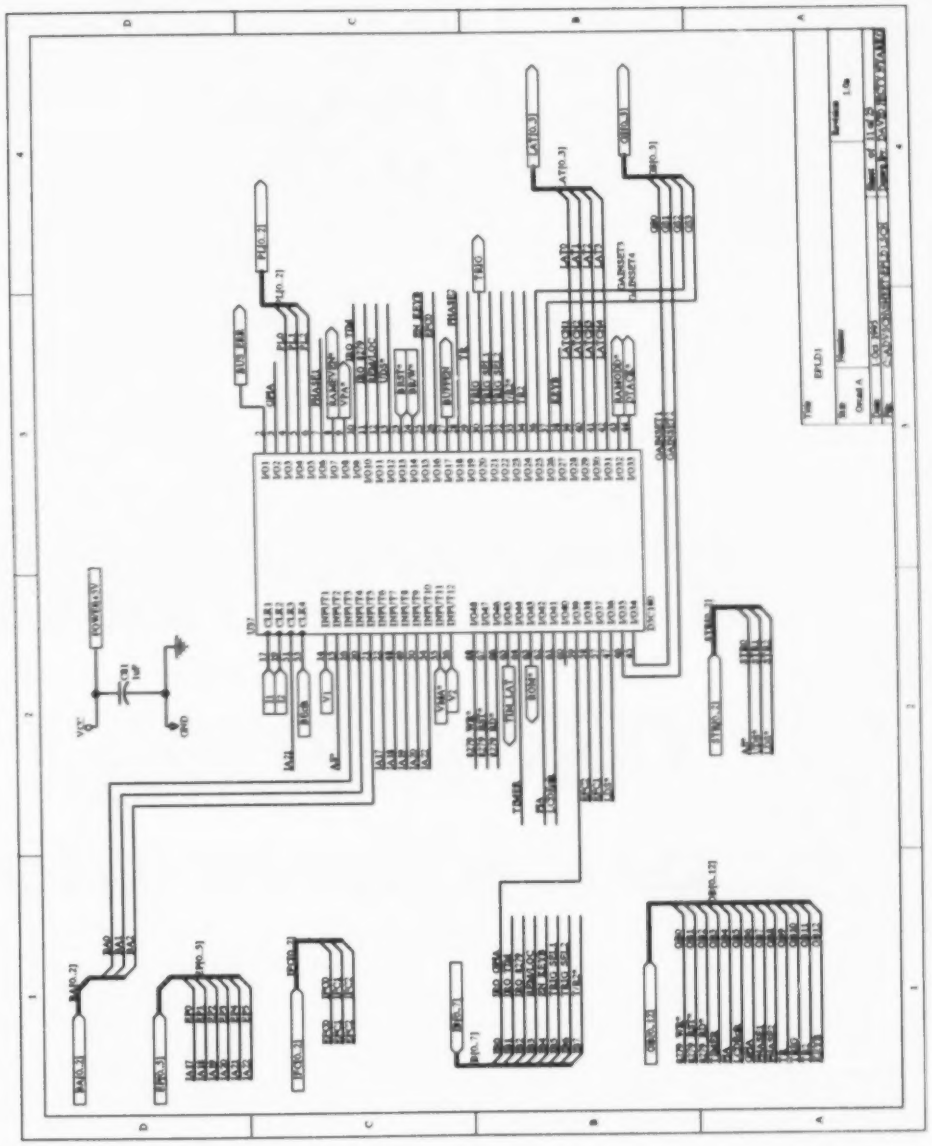

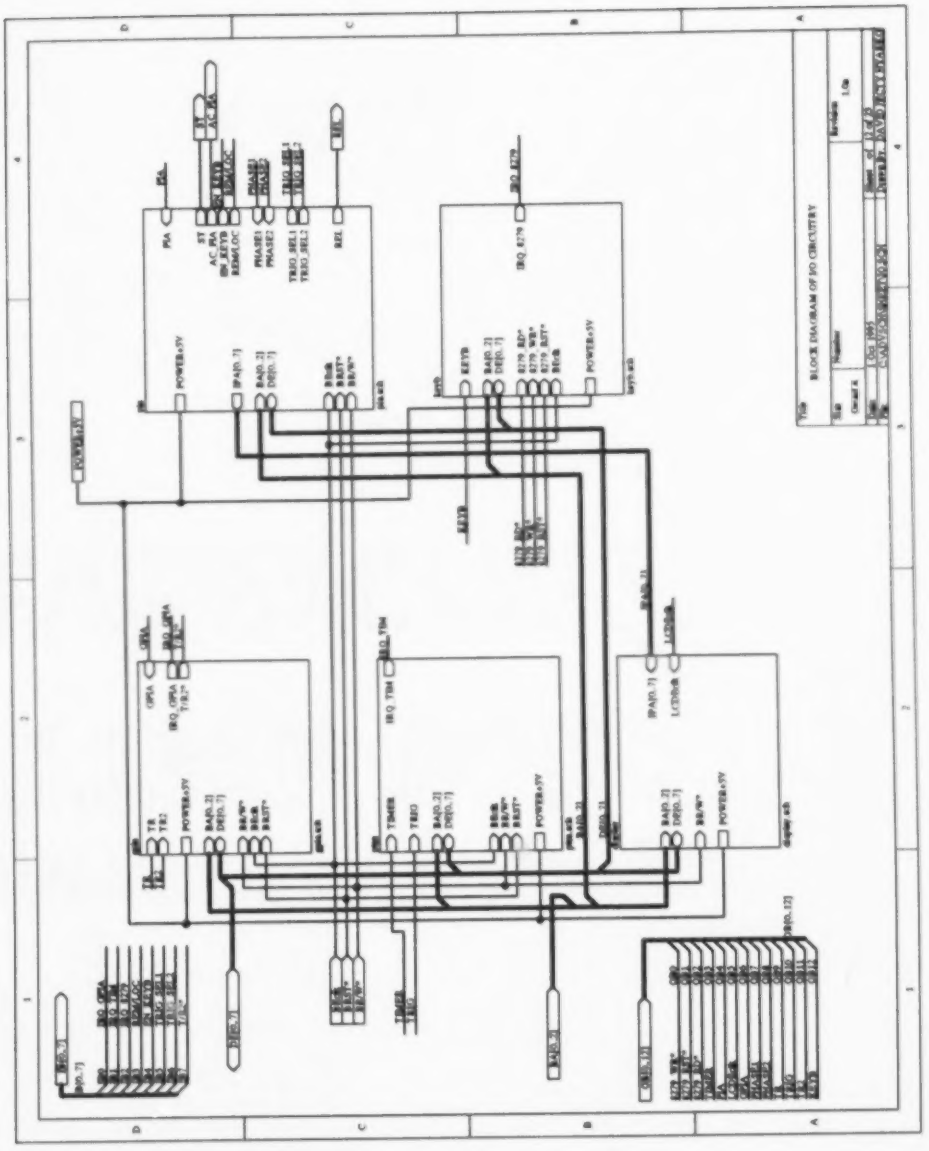

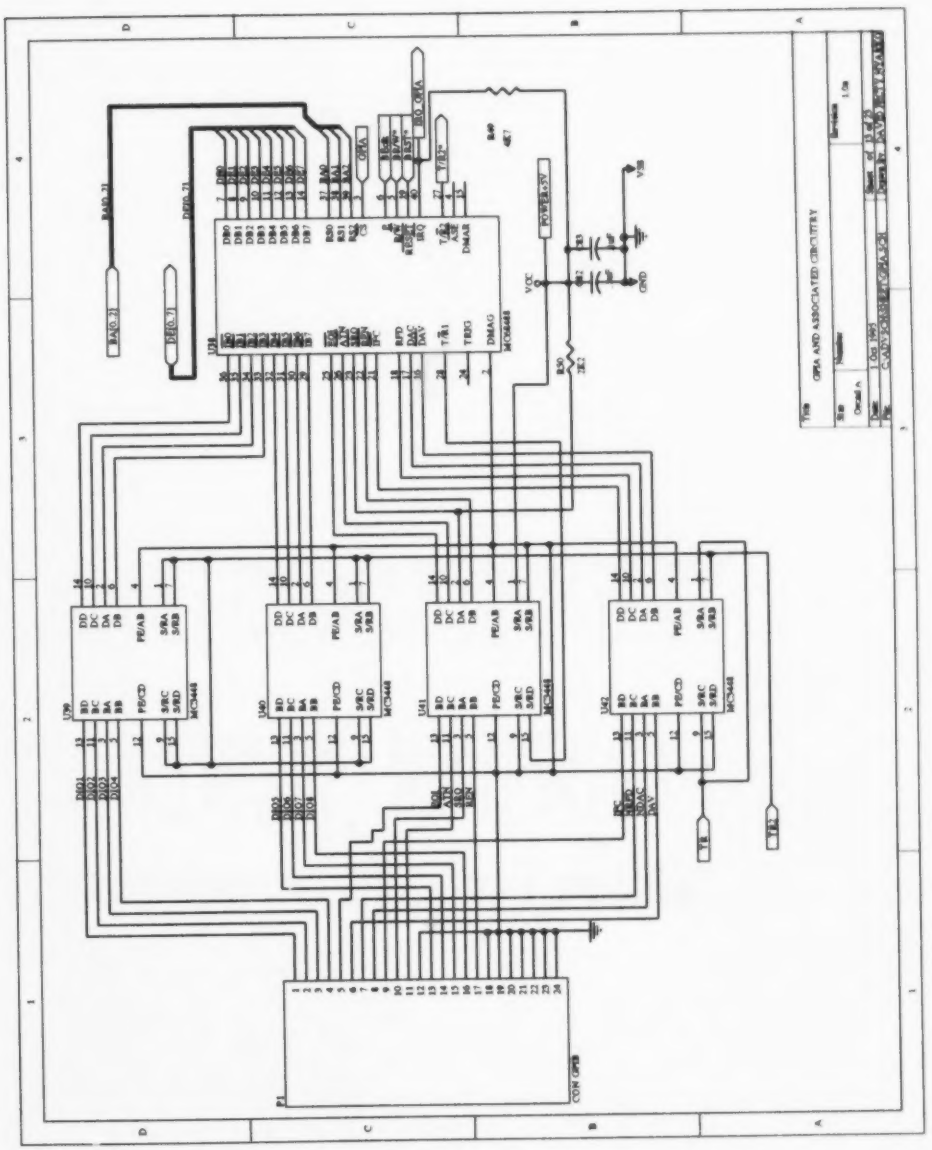

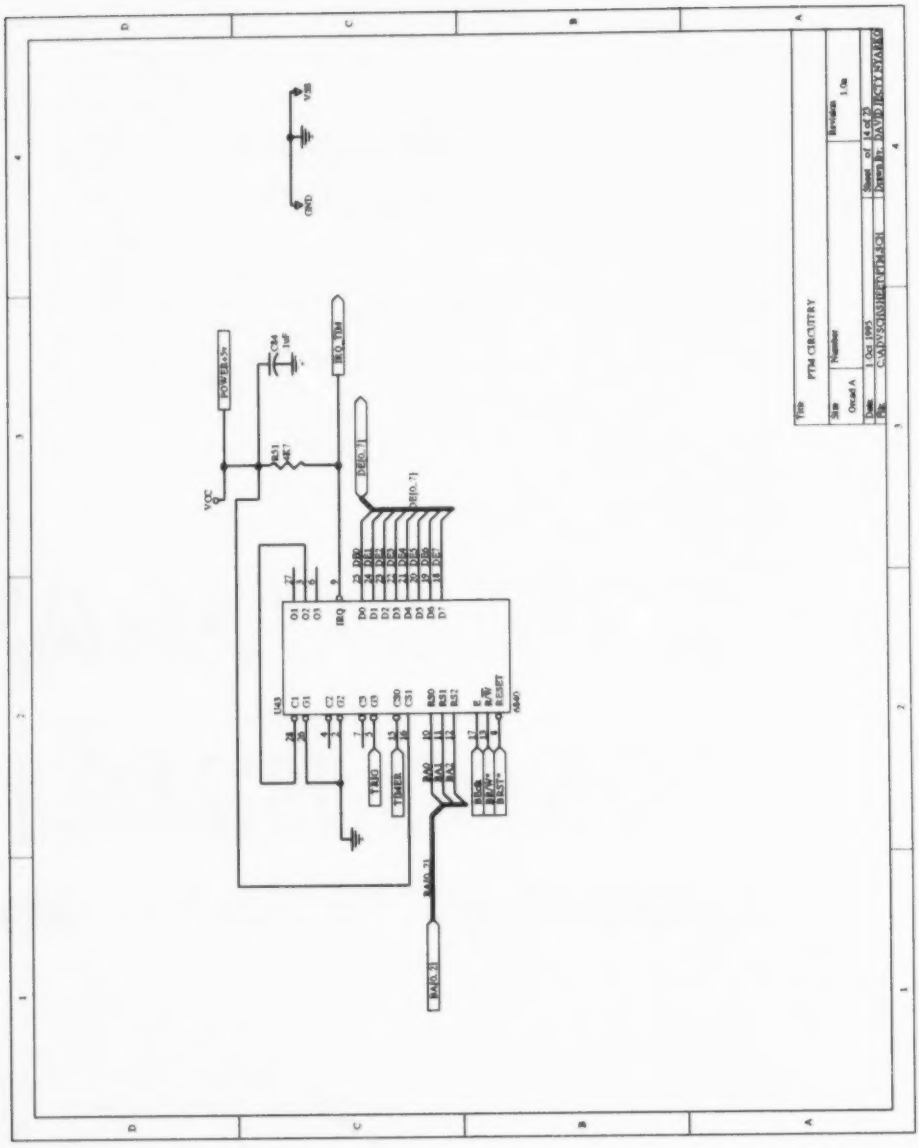
PTM CIRCUITRY
Size
Number
Revision
Date: 1 Oct 1995
Sheet of 14 of 23
File: C:\ADVSYS\STRATEGY\PTM.SCH
Drawn By: DAVID HOLLAND
VSS
GND
POWER+5v
VCC
R31
10KT
C34
1nF
IRQ_TIM
DB[0..7]
U43
TIMER
RESET
A[0..2]

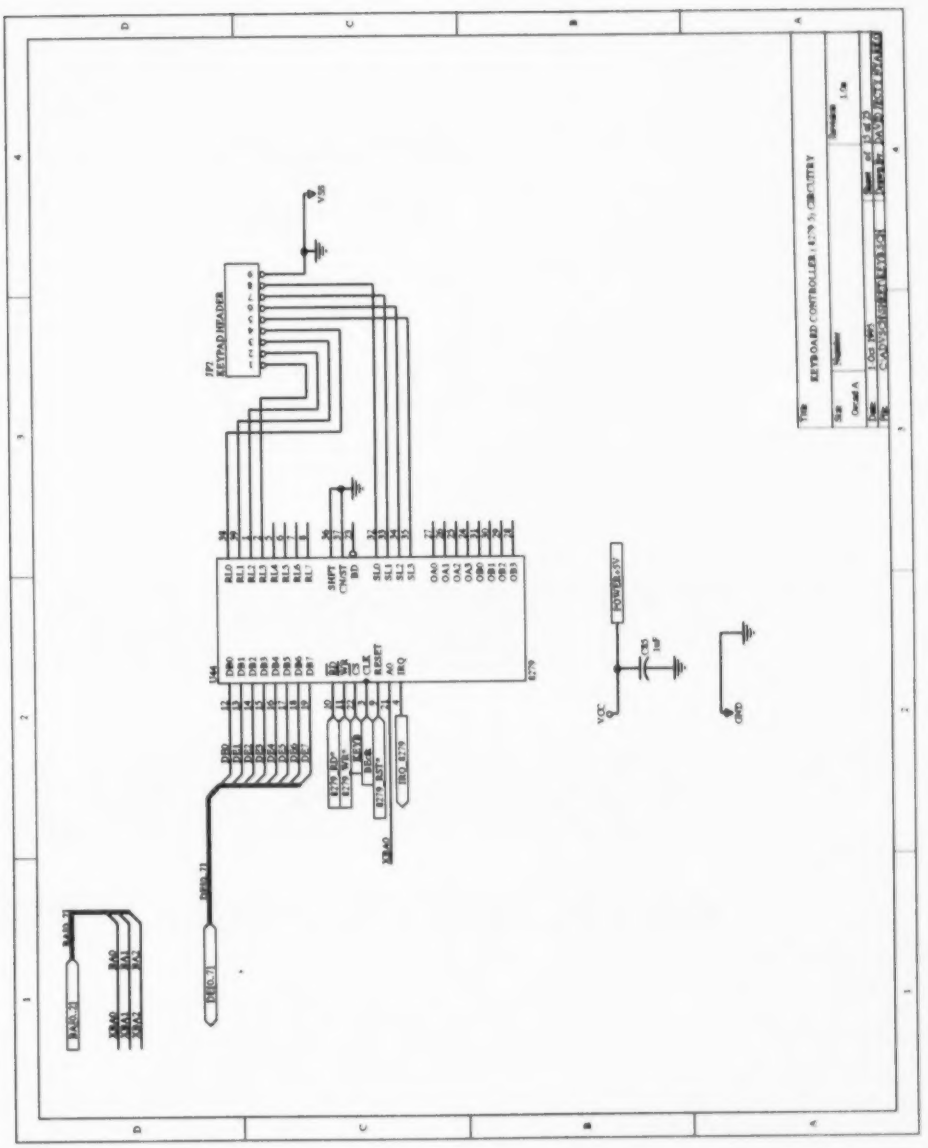
KEYBOARD CONTROLLER (8279) CIRCUITRY
KEYPAD HEADER
8279
SHIFT
CNTRST
IRQ
CLK
RESET
POWER 5.0V
GND
VCC

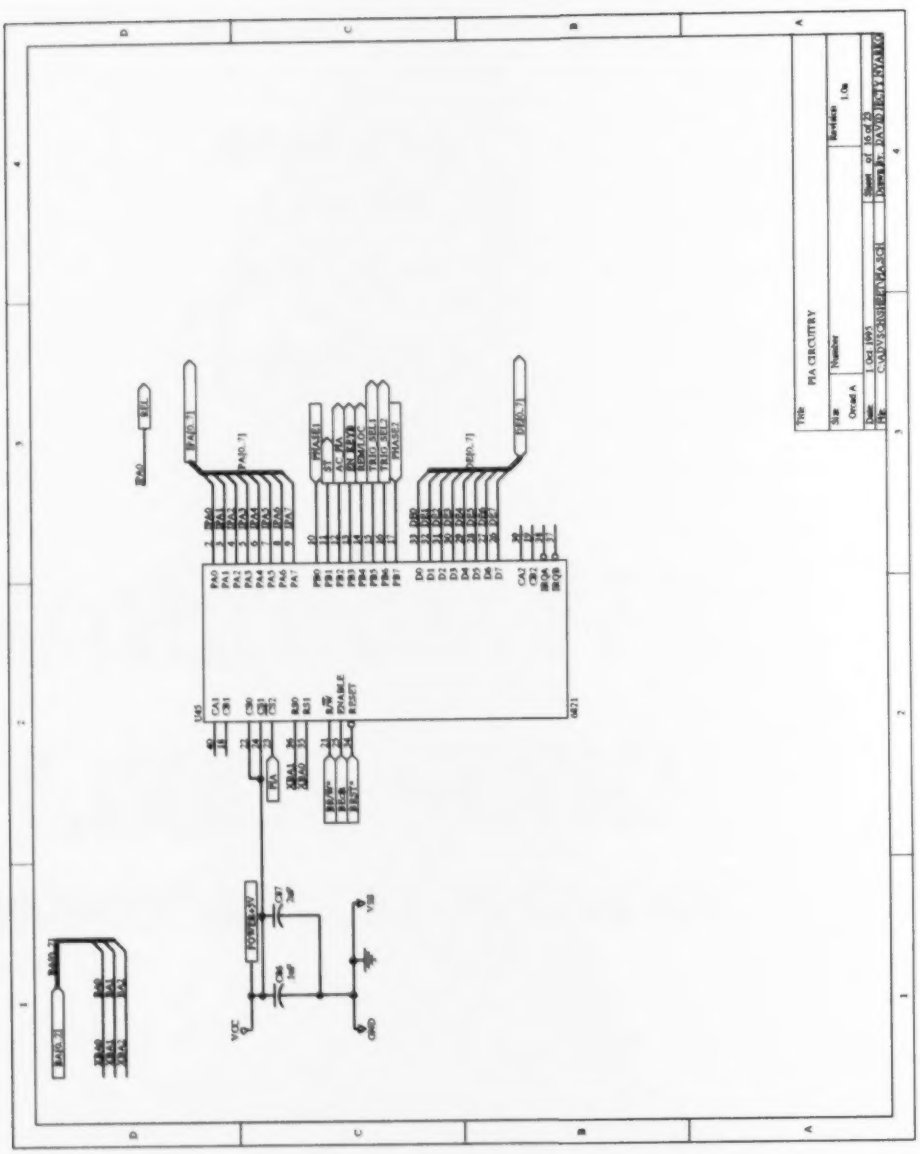
PIA CIRCUITRY
Number
Revision
1.0a
Oct 1993
Sheet of
File:
Title
Size
Drawn By:
Date:
PA[0..7]
PB[0..7]
PHASE1
PHASE2
PHASE3
PHASE4
PHASE1_SEL1
PHASE2_SEL2
PHASE3_SEL3
PHASE4_SEL4
PHASE_SEL
PHASE
RESET
ENABLE
VCC
GND
VSS
U21
6821

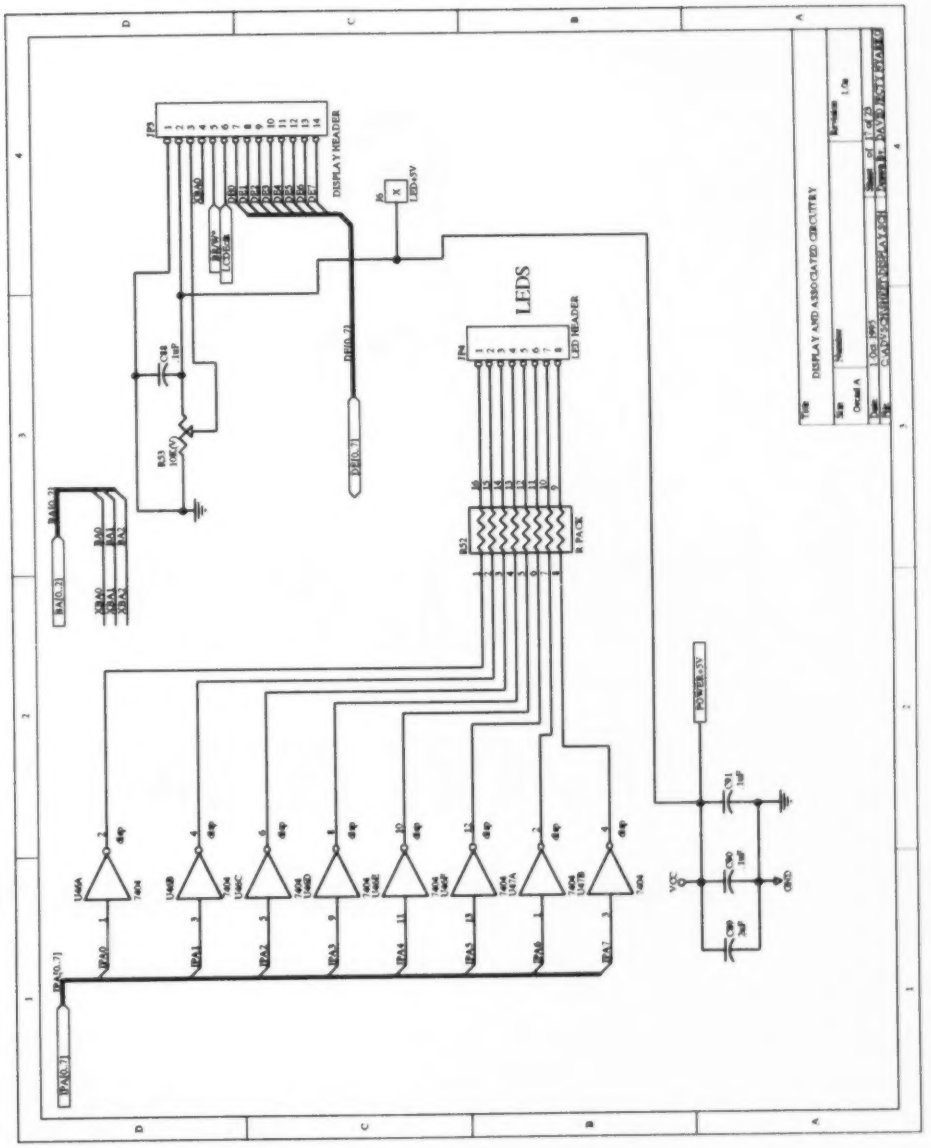
DISPLAY HEADER
LEDS
LED HEADER
R PACK
DISPLAY AND ASSOCIATED CIRCUITRY
POWER+5V
LED+5V
VCC
GND

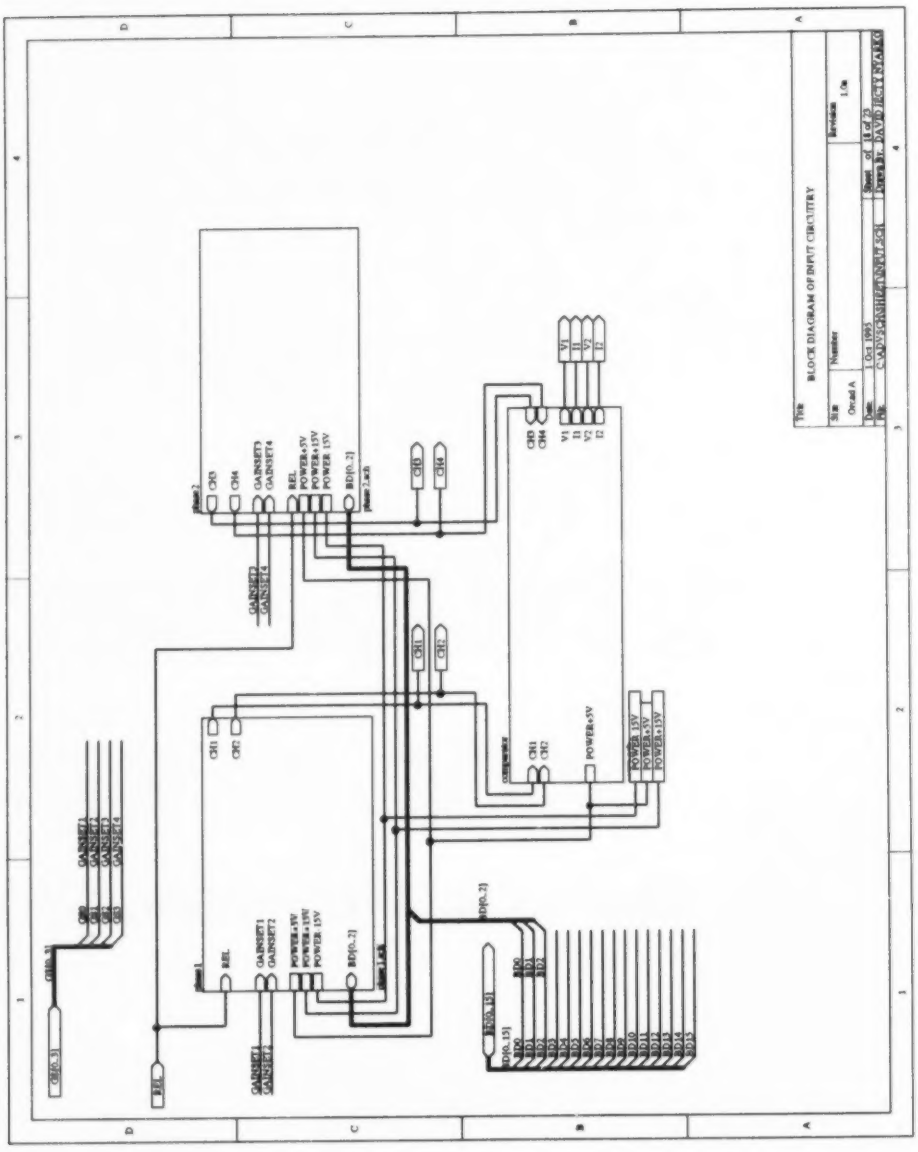
BLOCK DIAGRAM OF INPUT CIRCUITRY
Number
Revision
1.0a
Size
Date
1 Oct 1995
Sheet of
DAVID BECKWITH
CHAN3
CHAN4
GAINSET3
GAINSET4
REL
POWER+5V
POWER+15V
POWER-15V
BD[0..2]
CHAN1
CHAN2
GAINSET1
GAINSET2
V1
I1
V2
I2
POWER-5V
CHAN[0..3]
BD[0..15]

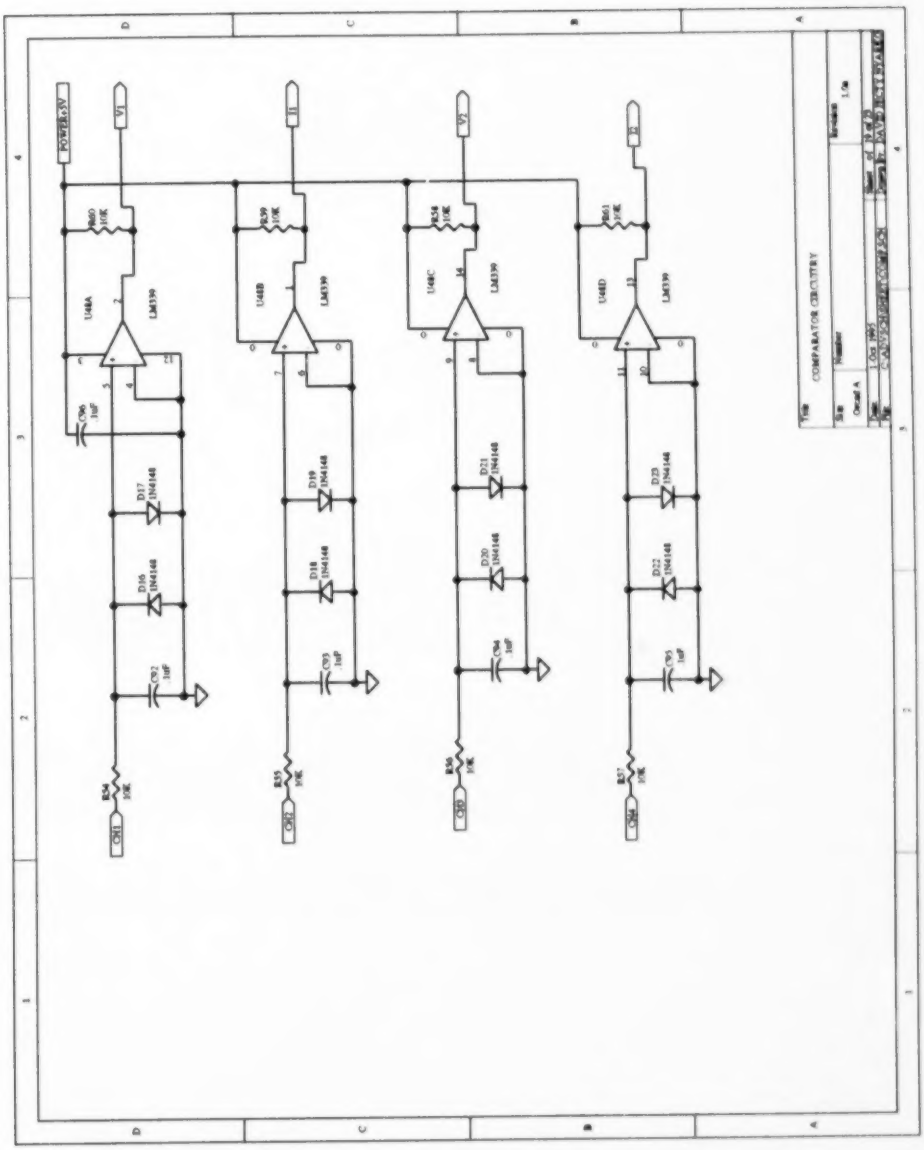
POWER+5V
V1
I1
V2
I2
R60 10K
R59 10K
R58 10K
R61 10K
U4A LM339
U4B LM339
U4C LM339
U4D LM339
C96 1nF
C92 1nF
C93 1nF
C94 1nF
C91 1nF
D17 1N4148
D16 1N4148
D19 1N4148
D18 1N4148
D21 1N4148
D20 1N4148
D23 1N4148
D22 1N4148
R54 10K
R55 10K
R56 10K
R57 10K
GND
COMPARATOR CIRCUITRY
Number
Size
Date: 1 Oct 1997

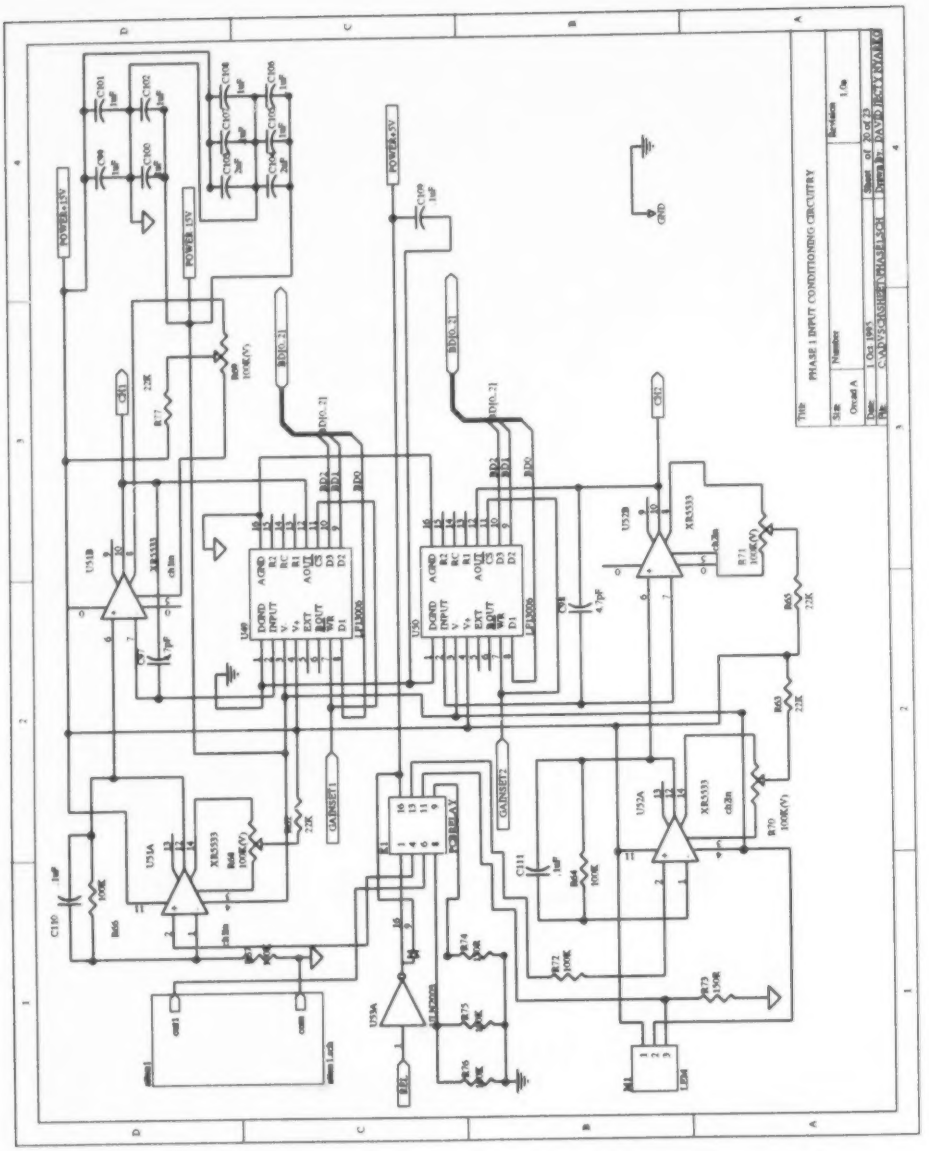
PHASE 1 INPUT CONDITIONING CIRCUITRY
Title
Size
A
Number
Revision
1.0a
Date:
1 Oct 1995
Sheet of
File:
C:\MY93-95\THESIS\PHASE1.SCH
Drawn By:
POWER+15V
POWER-15V
GND
BD[0..3]
GAINSEL1
GAINSEL2
XR5533
LF13508
LF13006
PCB/BAY
LED1
LED2
C100
C101
C102
C103
C104
C105
C106
C107
C108
C109
C110
C111
R64
R65
R66
R67
R68
R69
R70
R71
R72
R73
R74
R75
R76
U50
U51A
U51B
U52A
U52B
U53A
U53B
K1
J8
M1

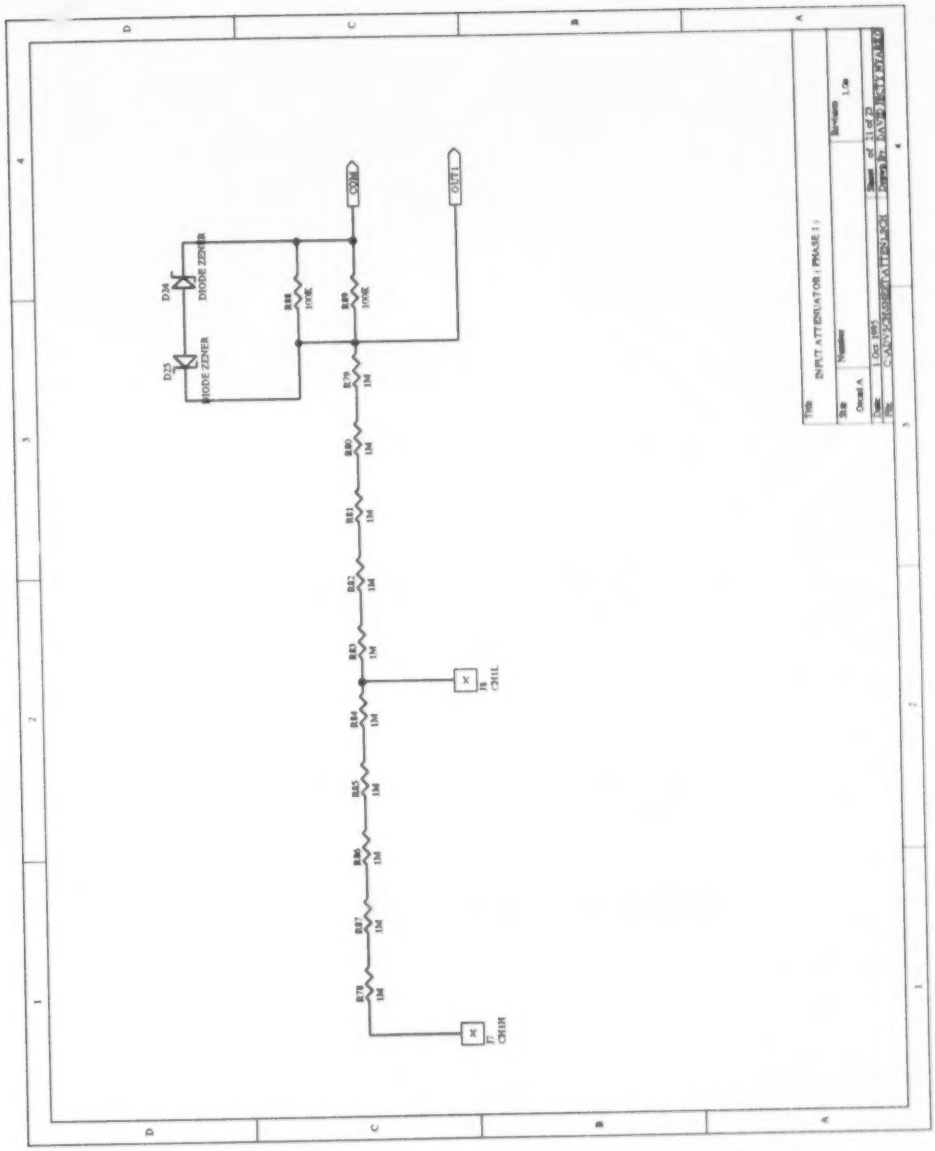
D
C
B
A
4
3
2
1
COM
OUT1
D24
DIODE ZENER
D25
DIODE ZENER
R88
100E
R89
100E
R79
1M
R80
1M
R81
1M
R82
1M
R83
1M
R84
1M
R85
1M
R86
1M
R87
1M
R78
1M
J8
CH1L
J7
CH1R
Title
INPUT ATTENUATOR (PHASE 1)
Size
Number
Revision
1.0a
Drawn By:
Sheet of 31 of 73

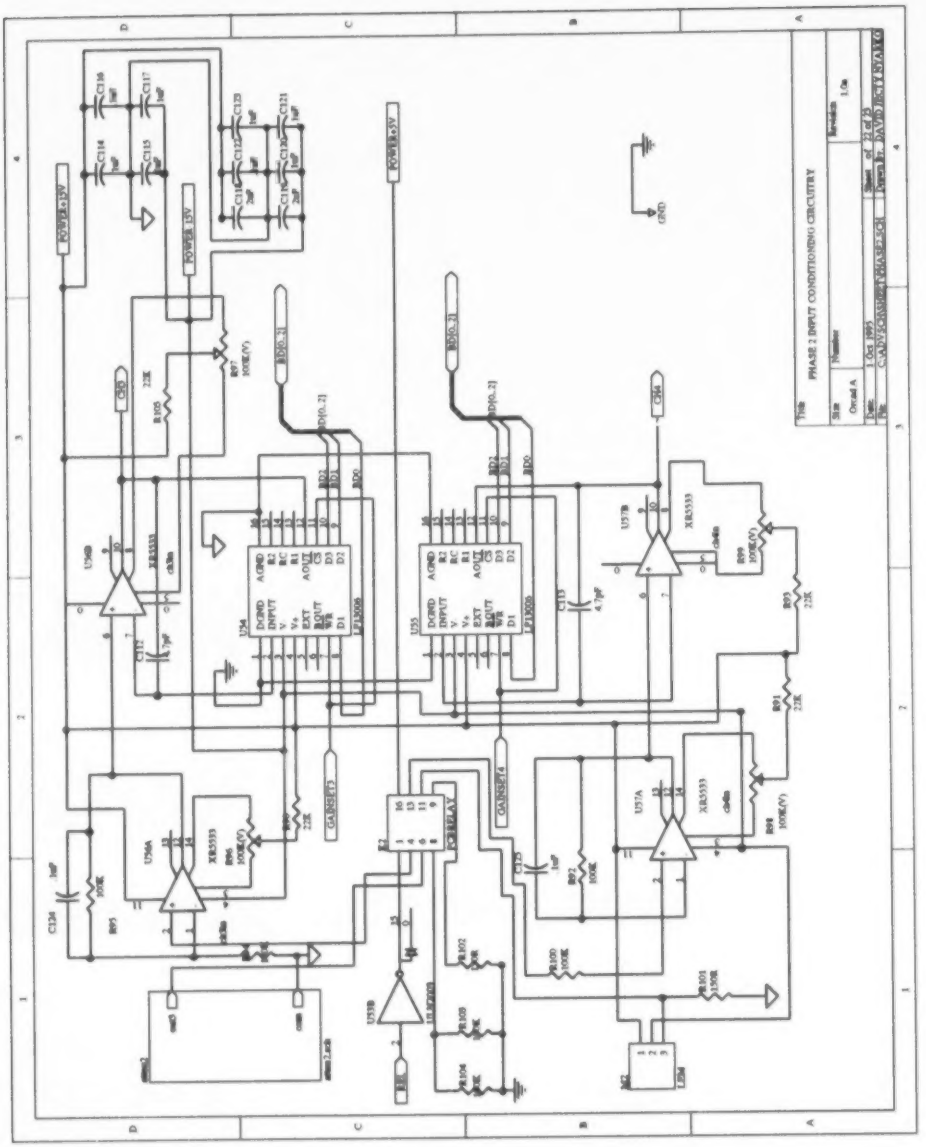

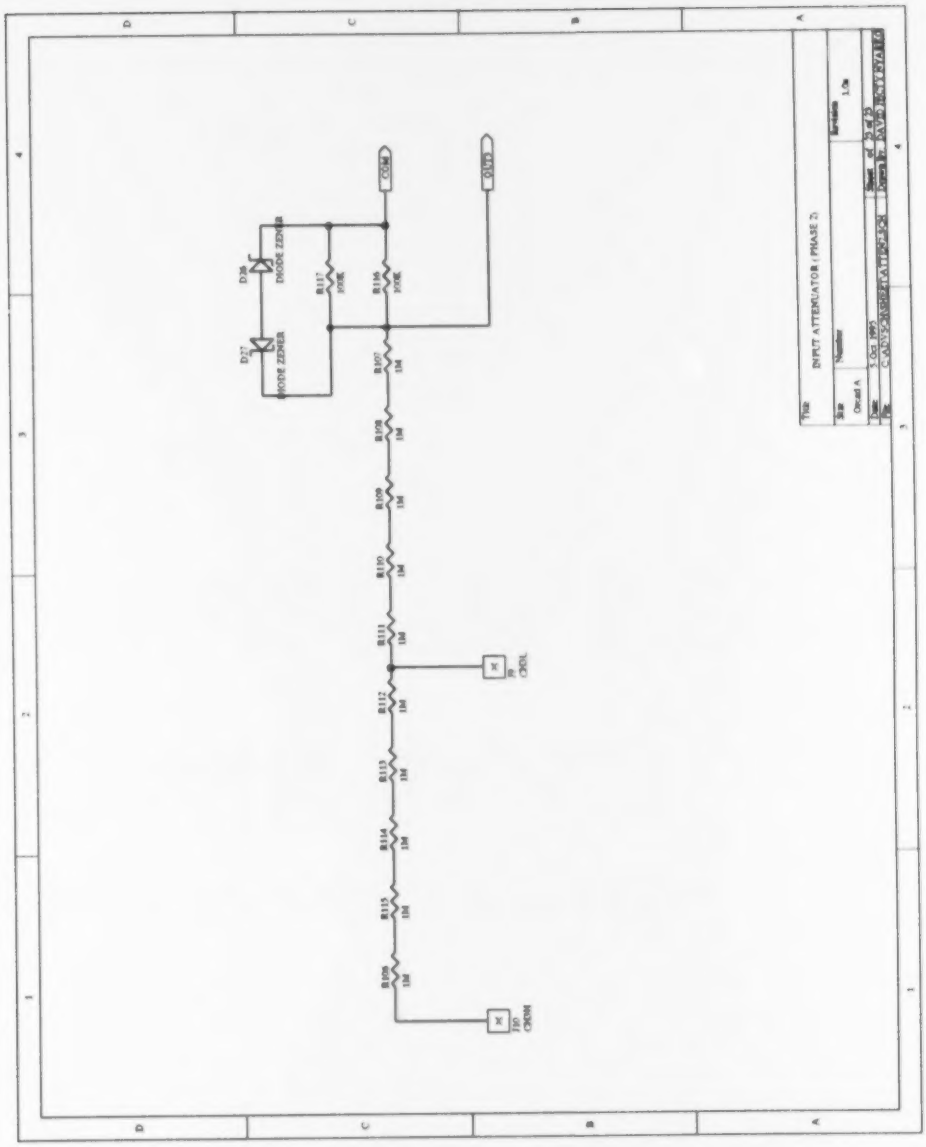
INPUT ATTENUATOR (PHASE 2)
COM
D36
DIODE ZENER
D37
DIODE ZENER
R107
1M
R108
1M
R109
1M
R110
1M
R111
1M
R112
1M
R113
1M
R114
1M
R115
1M
R116
1M
R117
1M
J1
J2